

EXPLORING THE MAGNETIC PHASES IN DYSPROSIUM
BY NEUTRON SCATTERING TECHNIQUES

by

JIAN YU

GARY J. MANKEY, COMMITTEE CHAIR

CONOR HENDERSON
PATRICK R. LECLAIR
CLAUDIA K.A. MEWES
TAKAO SUZUKI

A DISSERTATION

Submitted in partial fulfillment of the requirements
for the degree of Doctor of Philosophy
in the Department of Physics and Astronomy
in the Graduate School of
The University of Alabama

TUSCALOOSA, ALABAMA

2014

Copyright Jian Yu 2014
ALL RIGHTS RESERVED

ABSTRACT

With one of the highest intrinsic magnetic moments ($10.6 \mu_B$) among the heavy rare-earth elements, dysprosium (Dy) exhibits a rich magnetic phase diagram, including a few modulated magnetic phases. Aided by the Ruderman-Kittel-Kasuya-Yosida (RKKY) interaction, the magnetic modulations propagate coherently over a long range, even with intervening non-magnetic layers. Neutron diffraction experiments were performed to determine the microscopic magnetic origin of the field induced phases in bulk Dy as a function of temperature, covering regions of the well-known ferromagnetic, helical antiferromagnetic, fan phases and several possible new phases suggested by previous studies. A short range ordered (SRO) fan phase was identified as the intermediate state between ferromagnetism and long range ordered (LRO) fan. The temperature range of a coexisting helix/fan phase was also determined. The magnetic phase diagram of Dy was thus refined to include the newly determined magnetic structures and the associated phase boundaries. Based on the period of the magnetic modulation and the average magnetization, the evolution of the spin arrangement upon heating was derived quantitatively for the modulated magnetic phases. To gauge the effect of nanostructuring on the magnetic phases with nonmagnetic Y layers, epitaxial Dy/Y superlattices of various layer thicknesses and repeats were fabricated by magnetron sputtering under carefully controlled conditions. X-ray characterizations confirmed that the crystallographic and interfacial qualities of the superlattices are comparable to those grown by MBE in previous studies. The macroscopic magnetization was characterized by magnetometry, whereas the microscopic magnetic structures were extracted

from neutron diffraction and polarized neutron reflectometry (PNR) measurements. The ordering of helical modulation is sensitive to the interfacial roughness of the multilayer as well as the cooling histories. Off-specular PNR was applied the first time to characterize the helical domain structures in Dy/Y multilayers. The lateral correlation length in the helical magnetic structure was in the order of 100 nm.

DEDICATION

This thesis is dedicated to my dear family for their unconditional love and support throughout my Ph.D. years.

LIST OF ABBREVIATIONS

<i>AC</i>	Alternating current
<i>ADAM</i>	Alabama Deposition system for Advanced Materials
<i>bcc</i>	body centered cubic
<i>BNL</i>	Brookhaven National Laboratory
<i>CVD</i>	Chemical vapor deposition
<i>DC</i>	Direct current
<i>DMI</i>	Dzyaloshinsky-Moriya interaction
<i>FIE-TAX</i>	Fixed-incident-energy triple-axis spectrometer
<i>FM</i>	Ferromagnetic/ferromagnetism
<i>FWHM</i>	Full width at half maximum
<i>hcp</i>	hexagonal close-packed
<i>HFIR</i>	High flux isotope reactor
<i>HM</i>	Helical magnetic
<i>LRO</i>	Long-range ordering
<i>MBE</i>	Molecular beam epitaxy
<i>MPMS</i>	Magnetic property measurement system
<i>MR</i>	Magnetic reflectometer
<i>NIST</i>	National Institute of Standards and Technology
<i>ORNL</i>	Oak Ridge National Laboratory

<i>PG</i>	Pyrolytic graphite
<i>PNR</i>	Polarized neutron reflectivity/reflectometry
<i>PM</i>	Paramagnetic/paramagnetism
<i>PPMS</i>	Physical Property Measurement System
<i>PSD</i>	Position-sensitive detector
<i>PVD</i>	Physical vapor deposition
<i>RF</i>	Radio frequency
<i>RGA</i>	Residual gas analyzer
<i>RKKY</i>	Ruderman-Kittel-Kasuya-Yosida
<i>SANS</i>	Small angle neutron scattering
<i>SEMPA</i>	Scanning electron microscopy with polarization analysis
<i>SLD</i>	Scattering length density
<i>SNS</i>	Spallation neutron source
<i>SQUID</i>	Superconducting quantum interference device
<i>SRO</i>	Short-range ordering
<i>TOF</i>	Time-of-flight
<i>UHV</i>	Ultra high vacuum
<i>VSM</i>	Vibrating sample magnetometer
<i>XRD</i>	X-ray diffraction
<i>XRR</i>	X-ray reflectivity

ACKNOWLEDGMENTS

I would like to express my deepest gratitude to my research advisor, my mentor Dr. Gary Mankey, for guiding me through the adventurous trails into the physics and beyond. Thanks to his tremendous passion and inspiring ideas in scientific researches, along with his rich experience and brilliant solutions on experiments, I have spent five enjoyable years working under his supervision.

This research would have not been possible without the financial support and the outstanding work environment provided by the Department of Physics and Astronomy and the MINT center throughout the years.

I am grateful to all the professors and staff in the Department of Physics and Astronomy and the MINT center who have been helpful during my graduate study. Especially, I always benefit greatly from the constructive ideas and advice provided by my dissertation committee, comprised of Dr. Conor Henderson, Dr. Patrick LeClair, Dr. Claudia Mewes and Dr. Takao Suzuki, as well as my preliminary committee members, Dr. James Harrell, Dr. Rainer Schad and Dr. Richard Tipping.

I am indebted to Dr. Hideo Sato (Tohoku University), who worked as a post-doctoral fellow in our group, for his valuable instructions and help on thin film fabrication and characterizations at the beginning of this work.

I would like to acknowledge Dr. Lee Robertson, Dr. Lowell Crow and Dr. Wei Tian, for their generous help on the neutron diffraction experiments, along with Dr. Valeria Lauter, Dr.

Hailemariam Ambaye and Dr. Richard Goyette for their excellent assistance on the neutron reflectivity measurements performed in ORNL.

I wish to thank all the colleagues who helped directly or indirectly on my research. The instrumentation setup in this work could not be done without the teamwork with Dr. Hwachol Lee (NIMS, Japan). The magnetometer measurements were performed with the huge assistance from Sahar Keshavarz and Dr. Dipanjan Mazumdar. I am also thankful to Dr. Ru Zhu (Graceland University), Dr. Ning Li (Applied Materials), Dr. Xing Zhong (Intel), Dr. Neha Pachauri (Intel), Yinjun Zhang, Su-chi Chang, Ezhil Manoharan, and Narpinder Chahil for their helpful support and discussions on my research.

I must also thank the machine shop staff, David Key, Danny Whitcomb, Joe Howell and Jason Kuykendall, and the MINT facility manager John Hawkins, for their professional support on the hardware in our laboratory.

A special thank goes to Dr. Prakash Mani, Dr. Mrugesh Desai, Dr. Kumar Srinivasan and Dr. Cristian Papusoi for their influence to my understanding of magnetism during my internship with the Western Digital Inc.

This work is supported by the DOE award DE-FG02-08ER46499. The neutron scattering experiments performed at ORNL were sponsored by the Scientific User Facilities Division, Office of Basic Energy Science, U.S. Department of Energy.

CONTENTS

ABSTRACT.....	ii
DEDICATION	iv
LIST OF ABBREVIATIONS.....	v
ACKNOWLEDGMENTS	vii
LIST OF TABLES.....	xi
LIST OF FIGURES	xii
1. INTRODUCTION	1
2. SAMPLE FABRICATION AND PRELIMINARY CHARACTERIZATIONS	11
2.1 Magnetron sputtering	11
2.1.1 Vacuum system.....	11
2.1.2 Sputtering process.....	15
2.1.3 Epitaxial thin film growth.....	17
2.2 Structural characterizations.....	20
2.2.1 X-ray reflectivity.....	20
2.2.2 X-ray diffraction	23
2.2.3 Rocking curve	25
2.2.4 Pole figure.....	25
2.3 Magnetic characterizations.....	26
2.3.1 Low-temperature vibrating sample magnetometer (VSM).....	26
2.3.2 Superconducting quantum interference device (SQUID)	28

3.	NEUTRON SCATTERING	30
3.1	Introduction to neutron scattering techniques	30
3.2	Principles of polarized neutron reflectometry (PNR)	31
3.3	Polarized neutron reflectometer	38
3.4	Principles of neutron diffraction	42
3.5	Triple-axis neutron diffractometer	43
4.	MAGNETIC PHASE DIAGRAM OF BULK Dy	46
4.1	Overview of neutron diffraction results	46
4.2	Temperature dependence of the lattice parameters of ^{163}Dy in various applied fields ..	52
4.3	Magnetic phases and the phase transitions of ^{163}Dy in zero field	54
4.4	Magnetic phases and the phase transitions of ^{163}Dy in the field of 1 T	57
4.5	Magnetic phases and the phase transitions of ^{163}Dy in the field of 1.5 T	65
4.6	The refined magnetic phase diagram	71
5.	CRYSTALLOGRAPHIC, MORPHOLOGICAL AND MACROSCOPIC MAGNETIC PROPERTIES OF Dy/Y SUPERLATTICES	73
5.1	Epitaxial Dy/Y superlattices grown on a-sapphire.....	73
5.2	Crystallographic and morphological qualities characterized by X-ray	78
5.3	Magnetization of Dy/Y superlattice at low temperatures.....	85
6.	MICROSCOPIC MAGNETIC STRUCTURES IN Dy/Y SUPERLATTICES	90
6.1	Helical magnetic structures observed by neutron diffraction.....	90
6.2	Helical spin configuration measured by specular PNR.....	94
6.3	Evidence of helical antiferromagnetic domains shown in off-specular PNR	102
7.	CONCLUSIONS	105
	REFERENCES	107

LIST OF TABLES

1. Three pumping modes of the cryo pump in the ADAM system.....	14
2. The comparison of the typical background pressure and partial pressure of different gas molecules in ADAM system before and after overnight baking.....	15
3. The important properties of neutrons and the corresponding advantages when applied to condensed matter physics.....	31
4. The list of the measurement conditions of the neutron diffraction experiments performed on the ^{163}Dy crystal.....	47
5. The chemical profiles extracted by XRR for the seven superlattices selected for neutron scattering experiments.....	79
6. The comparison of the X-ray characterization results for sample c and d.....	85
7. The summary of the cooling fields, measurement temperatures and fields and the resultant magnetic states for sample a, b, c and d which went through the PNR measurements.....	96

LIST OF FIGURES

1. The simplified schematics of a helix (left) and a fan (right) modulation propagating along the c-axis of the hexagonal rare-earth lattice.....	4
2. The magnetic phase diagram of Dy constructed in reference [17] with the magnetic field applied along the a-axis.....	6
3. The visualization of the nuclear, magnetic and total potential sensed by the neutrons for a Dy/Y superlattice.....	9
4. The diagram of the helical magnetic domains of opposite chirality in a field applied along the basal plane of a Dy/Y superlattice. The propagation of the helical moment through the non-magnetic Y is also shown.....	10
5. The schematic of the vacuum system in the ADAM sputtering system.....	13
6. The magnetron sputtering process in the ADAM system.....	17
7. The design of the heater assembly and the rotational stage in the ADAM system.....	19
8. The schematic of the X-ray reflected by a thin film.....	21
9. The schematic of the Philips X'pert X-ray diffractometer.....	23
10. The illustration of the pole figure scan for the (111) planes of a simple cubic structure while the film surface is the (100) plane.....	26
11. The schematic of the VSM measurement in the Quantum Design DynaCool PPMS system.....	28
12. The schematic of the magnetization measurement in the Quantum Design MPMS SQUID system.....	29
13. The schematics of the specular reflection (left) and the off-specular (diffuse) scattering (right).	33
14. The flow chart for extracting the SLD profile from the neutron reflectivity data.....	37

15. The typical schematics of a monochromatic (top) and polychromatic (bottom) reflectometer	39
16. The 2-D raw data of the neutron reflectivity measured at the MR at a given incident angle. Left: neutron reflectivity versus the X and Y-pixel; Right: neutron reflectivity versus the X-pixel and the TOF	42
17. The schematic of a typical triple-axis spectrometer.	44
18. The raw data of the neutron diffraction scans along the c-axis of the ^{163}Dy crystal at various temperatures with the field of 1 T applied along the a-axis.....	47
19. The raw data of a single neutron diffraction scan along the c-axis of the ^{163}Dy crystal at a fixed temperature (170 K) with the field of 1 T applied along the a-axis.	49
20. The neutron diffraction pattern of pure nuclear origin measured at 275 K with no field applied.....	51
21. The neutron diffraction pattern of pure magnetic origin obtained by subtracting the nuclear contributions (Fig. 20) from the raw data (Fig. 19). The horizontal axis has been converted to the reduced wavevector [000L], in order to align the FM peaks.	52
22. The temperature dependence of the interplanar spacing along the c-axis of the Dy crystal in different fields (0, 1 T and 1.5 T) applied along the a-axis. The dash lines indicate the Curie temperature (89 K) and the Neel temperature (179 K).	53
23. The temperature dependence of the integrated intensity (top) of the magnetic diffraction peaks and the diffuse scattering, and the position (bottom) of the peaks with no field applied. The dash lines indicate the phase boundaries between the FM, helix, and PM phases.....	56
24. The temperature dependence of the propagation wavevector and the average turn angle of the helix modulation in zero field.....	57
25. The temperature dependence of the integrated intensity (top) of the magnetic diffraction peaks and the diffuse scattering, and the position (bottom) of the peaks with 1 T field applied along the a-axis of the Dy crystal. The dash lines indicate the phase boundaries between the FM, fan, coexisting helix and fan, helix, and PM phases.	59
26. The temperature dependence of the double peaks at the m2- magnetic satellite in a field of 1 T applied along the a-axis of the crystal. The peak at the lower L is due to the helix structure and the one at higher L stems from the fan modulation.	61
27. The temperature dependence of the propagation wavevector and the average period of the helix and fan modulations in 1 T field applied along the a-axis of the Dy crystal.	62

28. The evolution of the fan modulation (a-c) and the helix modulation (d-f) as temperature increases in the field of 1 T. Only one period of the magnetic modulation is shown. The average turn angle and opening angle are estimated based on the magnetization in reference [17]. The numbers at the end of the arrows indicate the indices of the Dy (0002) atomic layers.	65
29. The temperature dependence of the integrated intensity (top) of the magnetic diffraction peaks and the diffuse scattering, and the position (bottom) of the peaks with 1.5 T field applied along the a-axis of the Dy crystal. The dash lines indicate the phase boundaries between the FM, fan, and PM phases.	67
30. The magnetic diffraction patterns measured at (a) 114 K, (b) 136 K, (c) 155 K, and (d) 185 K when 1.5 T field is applied along the a-axis of the Dy crystal.....	68
31. The temperature dependence of the propagation wavevector and the average period of the fan modulations in 1.5 T field applied along the a-axis of the Dy crystal.	69
32. The evolution of the fan modulation as temperature increases in the field of 1.5 T. Only one period of the magnetic modulation is shown. The average turn angle and opening angle are estimated based on the magnetization in reference [17]. The numbers at the end of the arrows indicate the indices of the Dy (0002) atomic layers.	71
33. The refined magnetic phase diagram of Dy based on the neutron diffraction results, with the magnetic field applied along the a-axis.....	72
34. A comparison of the atomic spacing between the sapphire (11-20) plane, the Nb (110) plane and the Y (0002) plane.	74
35. The layout of the Dy/Y superlattice designed in this work.	75
36. The deposition rate for Nb, Dy and Y as a function of the Ar pressure. The circles indicate the pressure selected for depositing the superlattices.....	76
37. The optimization of the deposition temperature based on the XRD intensity of the Nb (110), Dy/Y (0002) and the Dy/Y (0002) satellite peaks. The circles indicate the temperature selected for depositing the superlattices.	77
38. The XRD pattern (top) for sample a and the zoomed in region (bottom) around the Dy/Y (0002) diffraction peak.	80
39. The measured and fitted XRR intensities for sample a. The inset shows the X-ray SLD depth profile for the superlattice extracted from fitting.....	81
40. The uniformity of the bi-layer thicknesses over the 2-inch-diameter sample c.....	82
41. The rocking curve measured on sample a around the Dy/Y (0002) peak.....	83

42. The pole figure measured for the Dy/Y (10-11) peak on sample a shows 6-fold symmetry.....	84
43. The temperature dependence of the magnetization for sample a, c and d during cooling in different magnetic fields applied in the sample plane.	87
44. The in-plane hysteresis loops measured at 5 K for sample a (bottom) and 10 K, 100 K for sample c (top).	89
45. The neutron diffraction patterns measured along the c-axis of the $[Dy_{16}/Y_{10}] \times 214$ superlattice as a function of temperature with no field applied. The intensities are shown in both the linear (top) and the logarithm (bottom) scales.....	91
46. The temperature dependence of the average turn angle of the magnetic moment in the Dy layers, calculated by the positions of the magnetic satellite peaks in Fig. 45.....	93
47. The thermal hysteresis of the intensities of the m- magnetic satellite.	94
48. The schematic of the PNR experiment. The applied field and neutron polarization are both parallel with the film plane.	95
49. The measured PNR intensities and simulations for sample a ($[Dy_{24}/Y_7] \times 8$) under different cooling histories, measurement temperatures and fields, covering a) PM state, b) FM state, c) remanent FM state, and d) helix state. The total neutron SLD profiles are shown in the insets.....	98
50. At 5 K and 10 mT applied field, the PNR measurements show the helical magnetic peaks and ferromagnetic components for sample c (top) and the helix modulation with no net magnetization for sample d (bottom).....	100
51. For sample d, the PNR measurements show the helical magnetic peaks and ferromagnetic components at the remanent state at 5 K (top) and the helix modulation with negligible net magnetization after warming up to 150 K (bottom).	101
52. The 3-D reflectivity contour (top) measured by PNR for sample c and d at the helical magnetic state and the off-specular rocking curves (bottom) when Q_z is fixed at the nuclear peak and two magnetic peaks respectively.	103

1. INTRODUCTION

The magnetic rare earth materials present unique opportunities for studying fundamental magnetism and have been intensively investigated for decades. They undergo complex phase transitions between a range of diverse magnetic phases through various temperatures and magnetic fields. For heavy rare-earth elements with a more than half-filled 4f shell, they exhibit several intermediate phases during the transitions from the high-temperature paramagnetic phases to the low-temperature ferromagnetic phases, excluding Gd, which orders ferromagnetically near room temperature [1]. The most interesting but unique feature for the intermediate magnetic phases is the oscillatory arrangement of spins, which gives rise to the modulated magnetic structures [1]. The modulated magnetic structure can have an oscillatory moment either in amplitude or orientation or both. The helical configuration in Dy is an example of the oscillatory orientation [2], while the conical configuration in Er is the case of both oscillatory orientation and amplitude [3]. It is well-known that the interaction between the localized 4f electrons through conduction electrons contributed by the 5d and 6s shells, known as the indirect Ruderman-Kittel-Kasuya-Yosida (RKKY) interaction, was primarily responsible for such oscillatory arrangements [4-6]. However, the actual magnetic structure in rare-earth materials can be the effect of the RKKY interaction perturbed by the anisotropic crystal-field and magnetoelastic interactions [7, 8]. Moreover, the competition between the interactions is temperature dependent, resulting in the complex magnetic phase diagram.

The investigation on these modulated magnetic structures was pioneered by Koehler et al. in the 1960s via neutron diffraction, and delivered a general understanding on the basic physics [2, 9-11]. However, the complete magnetic phase diagram as well as the rigorous mechanism of the phase transitions has not been fully understood for all heavy rare-earth elements. More detailed studies become feasible in recent years with the great advance in neutron scattering techniques in terms of the increased neutron flux and the flexibility of the instruments [12]. Here we explore the detailed magnetic phases in both bulk Dy and the Dy thin films using neutron diffraction and the polarized neutron reflectivity (PNR).

A Dy atom has 10 electrons from the 4f shell that account for its magnetic moment. According to Hund's rule, the total orbital angular momentum quantum number (L) and the total spin angular momentum quantum number (S) need to be maximized, i.e.

$$L = 2 \times (3 + 2 + 1) + 0 - 1 - 2 - 3 = 6, \quad (1)$$

$$S = 7 \times \frac{1}{2} - 3 \times \frac{1}{2} = 2. \quad (2)$$

Since the 4f shell is more than half filled, the total angular momentum quantum number (J) is given by

$$J = L + S = 8. \quad (3)$$

For L-S coupling, the total magnetic moment in a Dy atom is then:

$$\mu_J = g_J \sqrt{J(J+1)} \mu_B = 10.6 \mu_B, \quad (4)$$

where $\mu_B = 9.274 \times 10^{-24} \text{ A}\cdot\text{m}^2$ is the Bohr magneton, and the Lande g-factor is given by

$$g_J = 1 + \frac{J(J+1) + S(S+1) - L(L+1)}{2J(J+1)} = 1.25. \quad (5)$$

The intrinsic moment of $10.6 \mu_B$ per Dy atom is one of the largest in nature, in contrast to $2.2 \mu_B$ per Fe atom. The large Dy moment gives rise to strong magnetic scattering amplitude when interacting with neutrons. The magnetization for the perfectly saturated Dy can be calculated by

$$M_{Dy} = \frac{10.6\mu_B \cdot N_A}{V_{mol}} \approx 3100 \text{ emu/cc}, \quad (6)$$

where $N_A = 6.02 \times 10^{23}$ is the Avogadro's number, and $V_{mol} = 19 \text{ cm}^3/\text{mole}$ is the molar volume of Dy. The magnetic anisotropy energy of the order of 10^8 erg/cc at low temperatures is also enormous for Dy [13].

In zero magnetic field, bulk Dy is paramagnetic at room temperature, and the atomic spins order in an incommensurate helix below the Neel temperature of 179 K. At the Curie temperature of around 86 K, the helical magnetic state goes through a first-order phase transition and collapses to the ferromagnetic state [2]. The Dy crystal lattice is the hexagonal close-packed (hcp) structure and its basal plane is the magnetic easy plane. In the helical magnetic phase, the Dy moment is ferromagnetically aligned in each easy plane, but rotates about the c-axis by a certain turn angle (ϕ) in successive (0002) atomic planes. The schematic of a helix is shown in Fig. 1. The magnetic moment vector in the nth (0002) atomic plane can be written as

$$\mathbf{m}_n = m_0 [\cos(\varphi_0 + n\phi) \mathbf{i} + \sin(\varphi_0 + n\phi) \mathbf{j}], \quad (7)$$

where m_0 is the total magnetic moment in each (0002) plane, φ_0 represents the orientation of the moment in the first (0002) plane and ϕ is the turn angle of the moment between the adjacent (0002) planes. Note that the simple antiferromagnetic state is a special case of the helical phase, in which the turn angle is 180° . On the other hand, the helical ordering is antiferromagnetic, i.e. the total magnetization is zero over a magnetic unit cell, which consists of $N = 360^\circ/\phi$ atomic planes. The period of the magnetic modulation in bulk Dy is temperature dependent within the

helical magnetic region (89 K - 179 K). In terms of the turn angle, it decreases monotonically from 44° to 27° before it collapses into the ferromagnetic state where the turn angle is essentially 0° [2].

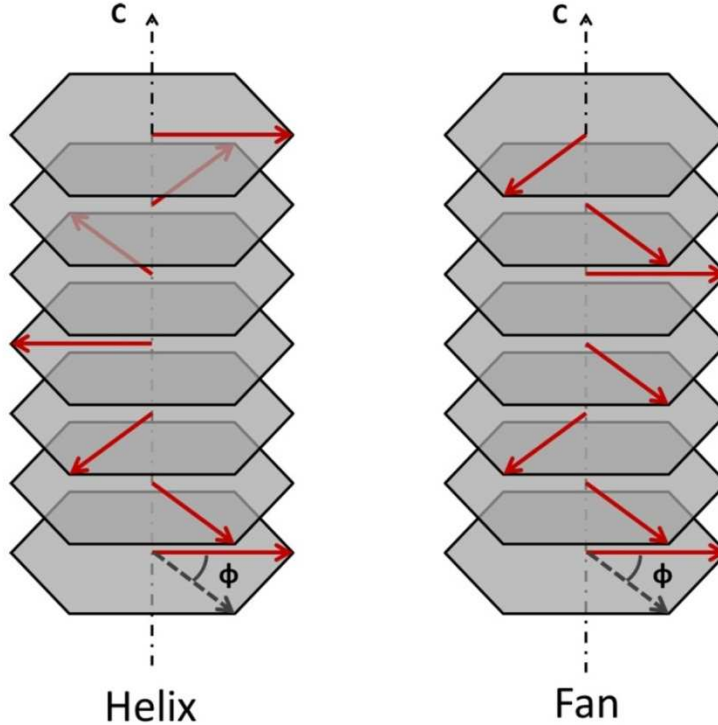


Figure 1. The simplified schematics of a helix (left) and a fan (right) modulation propagating along the c-axis of the hexagonal rare-earth lattice.

In a non-zero magnetic field, however, a couple of candidates of the intermediate phases have been reported between the paramagnetic, helical magnetic and ferromagnetic states of the bulk Dy. With a field applied along the a-axis, the appearance of a fan phase was confirmed by isothermal magnetization curves [14] and neutron diffraction [15]. The schematic of the fan phase is shown in Fig. 1. An extra phase boundary was detected within the region of the fan phase via the resistivity measurements but the nature of the related phases was unclear [16]. Chernyshov et al. observed many anomalies during a careful investigation on the magnetocaloric

effect, magnetization, AC susceptibility and heat capacity of the single-crystal Dy, and mapped out the most detailed version of the magnetic phase diagram for Dy (Fig. 2), which included a spin-flop phase, a vortex phase, and a few possible new phases [17]. However, further experiments are necessary in order to confirm the existence of the new phases and provide clear pictures of the new phases. In comparison, the magnetic structures in bulk Ho, the neighbor of Dy in the periodic table, have been largely revealed. A stable helifan phase was predicted by the self-consistent mean-field calculations [18] and verified by the neutron diffraction experiments [19] to intermediate the helix and fan phases in Ho when a certain range of magnetic field is applied in the basal plane. A spin-slip model was developed and successfully explained the harmonics around the magnetic satellites observed in both X-ray magnetic scattering [20] and neutron diffraction [21], and also agreed well with the theoretical calculations [22]. The neutron diffraction measurements on Dy in the past have covered a few discrete regions in the phase diagram only to identify the presence of the helix, fan and ferromagnetic phases [2, 15].

The magnetic phase transitions in bulk Dy are accompanied by a series of structural transitions. The structural transition and the magnetic transition can be coupled or decoupled at different temperatures. The lattice parameter of Dy along the c-axis is at minimum at the Neel temperature (179 K), above which it increases with temperature, but decreases between the Curie temperature (86 K) and the Neel temperature. Upon heating in zero field, an orthorhombic-hcp transition occurs at the Curie temperature, along with a discontinuity in the lattice parameter of the c-axis [23]. When a moderate magnetic field is applied in the basal plane of Dy crystal, the c-axis discontinuity shifts to a higher temperature, together with the ferromagnetism-helix transition, suggested by the magnetization measurements [14]. However, the orthorhombic-hcp transition appears independent of the field and always occurs at the Curie point [17].

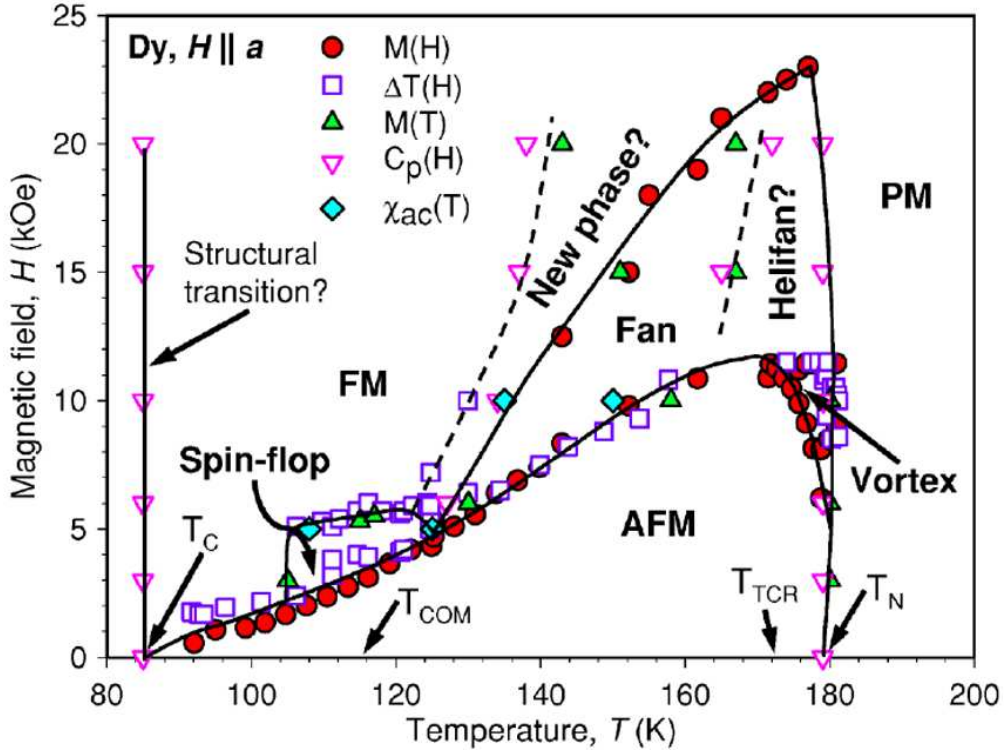


Figure 2. The magnetic phase diagram of Dy constructed in reference [17] with the magnetic field applied along the a-axis.

Aiming to examine the detailed magnetic phase diagram of bulk Dy as well as the mechanisms of the phase transition, neutron diffraction experiments were performed on a single-crystal ^{163}Dy at the Fixed-Incident-Energy Triple-Axis Spectrometer (FIE-TAX) located at the beam line HB-1A of the High Flux Isotope Reactor (HFIR), Oak Ridge National Laboratory (ORNL), by scanning throughout the temperatures covering the paramagnetic phase to the ferromagnetic phase at different applied fields. The results are discussed in Chapter 4.

Research on rare-earth multilayers have been another area of interest, in that the magnetic properties of rare-earth materials can be tuned on an atomic scale by inserting materials with varying interlayer coupling, giving rise to novel magnetic structures [24]. By inserting nonmagnetic but chemically and electronically similar layers, such as Y, into magnetic Dy thin

films, the RKKY interaction can be still effective, and the spin coherence in the superlattice propagates through many bilayers [25-28]. Dy and Y are both hcp structure and their lattice mismatch is relatively small at 1.6 %, so single-crystal Dy/Y superlattices are an ideal system for studying short-range magnetic interactions. Both structural and magnetic properties of Dy/Y superlattices differ distinctly from the bulk counterpart. The structural transition of Dy in the superlattice is much less abrupt than in the bulk, because of the clamping effect from the Y lattice. Therefore, the low-temperature ferromagnetic phase is suppressed in the Dy/Y superlattice system by the helical magnetic phase due to the modified lattice parameters through the magnetoelastic energy [25]. The turn angle of the helical structure in Dy/Y superlattice is also different from bulk values, ranging from 46° to 30° and locks at a constant value at low temperatures [26]. While Y is paramagnetic throughout all temperatures, the effective turn angle of the Dy moment through the intervening Y layer is 51° per Y atomic layer [25]. Recently, non-zero average spin chirality was observed in Dy/Y superlattices after field cooling, and this effect was attributed to the Dzyaloshinsky-Moriya interaction (DMI) induced by the broken of the inversion symmetry at the Dy/Y interfaces [29-31]. However, a detailed picture of the morphology of the helical magnetic structure is still absent, which is essential to understand the microscopic magnetic behavior in this system and gain better control of it.

Single-crystal Dy/Y superlattices of very high quality are required for the above research. While Molecular Beam Epitaxy (MBE) was used exclusively for the deposition of the superlattices in previous experiments [25-30], here we attempted magnetron sputtering for sample growth. The crystallographic and interfacial qualities of the superlattices were characterized by the X-ray techniques, while the macroscopic magnetic properties were characterized by low-temperature magnetometers. The methodologies regarding the magnetron

sputtering and the preliminary characterizations are discussed in Chapter 2 and the results are presented in Chapter 5. Based on the results of the preliminary characterizations, the superlattices were selected for further study by neutron scattering techniques.

The helical magnetic state in Dy is essentially a type of antiferromagnetic configuration with very small net magnetization. The magnetometers are not sensitive to the microscopic configuration of the helix. One of the most powerful tools to probe such microscopic magnetic heterostructures is the neutron scattering. Since neutrons interact with both the nucleus and the magnetic moment in the material in terms of different scattering potentials, the chemical and magnetic structures can be detected simultaneously by neutron scattering in the atomic scale [12]. Fig. 3 provides a visualization of what neutrons see for a Dy/Y superlattice in the helical magnetic state. The color scale represents the scattering length density (SLD) which is proportional to the interacting potential sensed by the neutrons. Neutron diffraction has been applied to both bulk Dy and Dy/Y superlattices routinely to characterize the period of the helical spins [2, 9, 25, 32], which is associated to the magnetic diffraction peaks. Polarized neutron reflectivity (PNR) is capable of probing the microscopic magnetic depth profile of the multilayers, and has been proved to be a powerful tool to detect the configuration of non-collinearly aligned moments in the antiferromagnetic coupled Fe/Cr superlattices [33, 34]. The non-zero average chirality of the helical structure in Dy/Y superlattices was also detected by PNR [29, 30]. Additionally, the off-specular scattering measured along with PNR provides information about the lateral magnetic domains in the structure [33, 35]. A detailed introduction of the neutron diffraction and PNR techniques is given in Chapter 3.

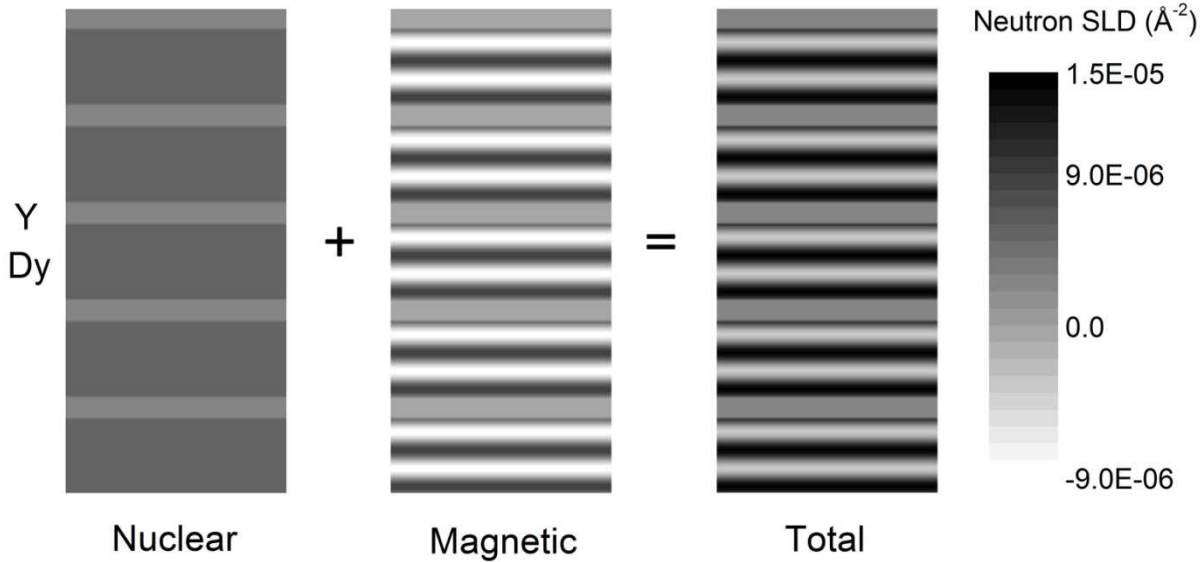


Figure 3. The visualization of the nuclear, magnetic and total potential sensed by the neutrons for a Dy/Y superlattice.

In Chapter 6, we present the magnetic structure, including but not limited to the helical magnetic state, of Dy/Y superlattices characterized by PNR under different temperatures, fields, and cooling conditions at the Magnetism Reflectometer (MR) of the Spallation Neutron Source (SNS) in ORNL. In the measurement of PNR, a small field has to be applied at the sample to maintain the polarization of the neutrons. In our case, the magnetic field was applied in the Dy/Y (0002) plane. For the incommensurate helical magnetic structure, the Dy layer between two nonmagnetic Y layers would exhibit an uncompensated magnetic moment. If the uncompensated Dy moment is not aligned with the external magnetic field, we expect the helical magnetic structures decompose into domains, in order to be stable. One possible domain configuration is the helix of opposite chirality, since such chirality domains have been observed in bulk Tb [36] and Ho [37]. The schematic of the chirality domains is shown in Fig. 4, as the magnetic moments of the two domains are symmetrical about the applied field such that no net magnetization is

perpendicular to the applied field. Other types of domain configuration are possible, such as the spin slip domains. The possibility of non-zero net chirality does not play any role here because the polarized neutrons could not distinguish between the left-handed and the right-handed domains in our PNR geometry. Direct evidence of the domain structures and the magnetic lateral correlation length in the helical state will be presented in Chapter 6, as seen in the off-specular scattering of the Dy/Y superlattices.

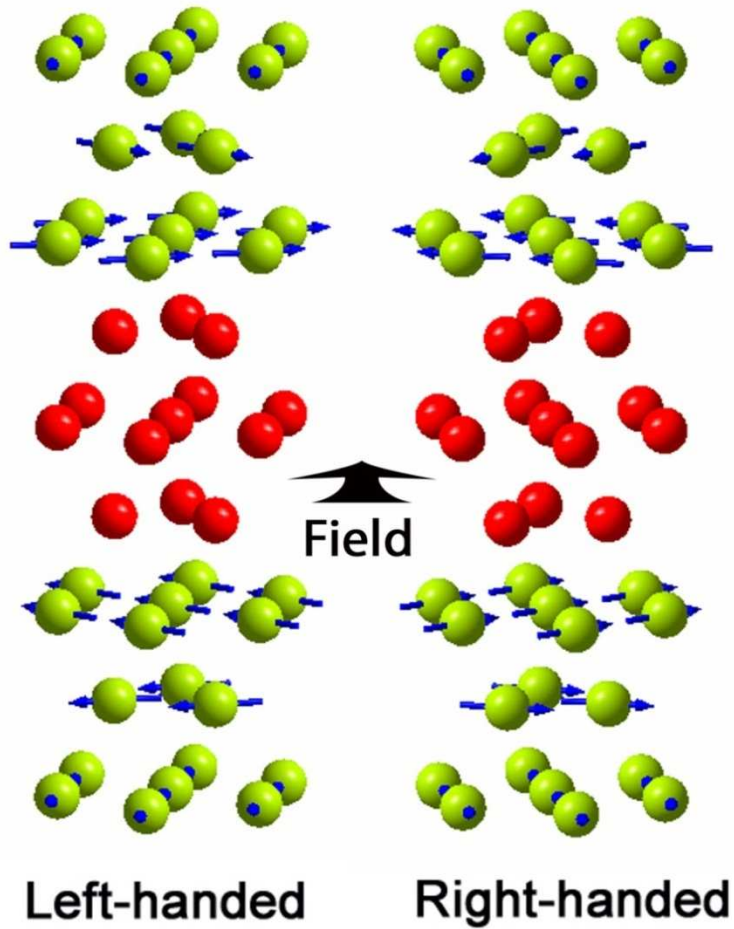


Figure 4. The diagram of the helical magnetic domains of opposite chirality in a field applied along the basal plane of a Dy/Y superlattice. The propagation of the helical moment through the non-magnetic Y is also shown.

2. SAMPLE FABRICATION AND PRELIMINARY CHARACTERIZATIONS

2.1 Magnetron sputtering

Sputter deposition is one of the most common physical vapor deposition (PVD) methods for thin film growth. By bombarding the target with energetic particles, the target materials escape from target surface and condense on the substrate. Sputter deposition has been widely used in the magnetic storage, semiconductor, and optical industries due to its ability to sputter a wide variety of materials including metals, alloys, and compounds. A basic sputtering system includes two components, a vacuum system and a diode discharge system.

In this dissertation, all Dy/Y multilayers were fabricated by a homemade magnetron sputtering system --- Alabama Deposition system for Advanced Materials (ADAM). Compared to Molecular Beam Epitaxy (MBE), which was used in all previous studies on Dy/Y multilayers [25-30], magnetron sputtering is a faster, more reliable and cost effective approach. In Chapter 5, it is shown that the Dy/Y multilayers deposited by magnetron sputtering are of the similar quality of the multilayers grown in MBE.

2.1.1 Vacuum system

The vacuum system provides a clean environment for the sputtering process. A clean vacuum is crucial for the quality of the deposited film, because it maintains the plasma discharge, keeps the atomically clean surfaces contamination-free, and increases the mean free path for the electrons and atoms. For example, it takes about 1 s for a surface to be coated by a

monolayer of contaminants in 10^{-6} Torr while the time is extended by a factor of 1000 for a 10^{-9} Torr vacuum [38]. The mean free path for the ideal gas molecules is 1000 m in a 10^{-9} Torr environment [39].

A basic vacuum system consists of vacuum chambers, vacuum pumps, and vacuum gauges. As an example, the schematic for the vacuum system of ADAM is shown in Fig. 5. There are two chambers connected by a gate valve. The load lock chamber operates in medium vacuum ($\sim 10^{-7}$ Torr) and can be vented and pumped down within a short time for loading and unloading samples without interrupting the ultra-high vacuum (UHV) in the main chamber (10^{-9} - 10^{-10} Torr), where the sputtering takes place. Three sample holders can be loaded at one time. The load lock chamber is connected to a Pfeiffer Balzers turbo pump (260 L/s) and a rotary vane pump in series. The vacuum pressures in the load lock chamber and the rough pumping line are given by a thermocouple gauge respectively. When medium vacuum is achieved, one can open the gate valve between the load lock and the main chamber to transfer samples using a mechanical manipulator. The main chamber is attached to a CTI cryo pump through a pneumatic gate valve. There is another bypass bellows with a hand operated valve connected between the main chamber and the cryo pump. This two-lane pumping configuration allows three pumping modes for different needs: a) high-speed pumping, b) low-speed pumping, and c) not pumping. See Table 1 for details of the three pumping modes. A Bayert-Alpert ionization gauge is used to measure the vacuum above the cryo pump. A residue gas analyzer (RGA) is installed in the main chamber to monitor the partial pressures of various gas molecules of different masses in the vacuum. High purity (99.99%) Ar is used as the sputtering gas in ADAM system and is connected to the main chamber through a flow controller. By sending a constant Ar flow and setting the cryo pump at low-speed pumping mode, the Ar pressure in the main chamber can be

maintained at a constant value (a few mTorr in practice). A MKS capacitance manometer gauge located in the main chamber reads the Ar pressure during sputtering because the gauge is most sensitive when the pressure is in the order or a few mTorr.

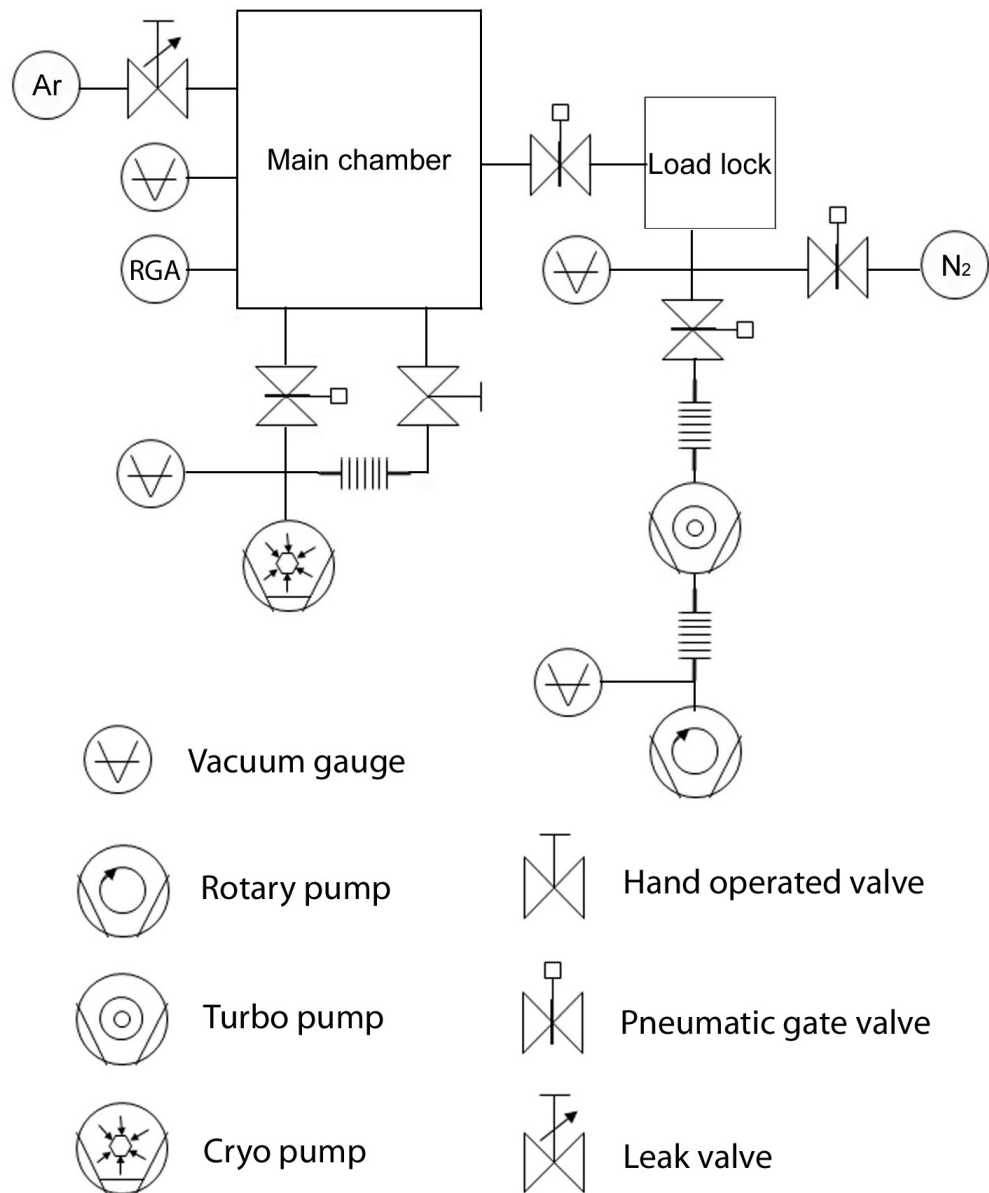


Figure 5. The schematic of the vacuum system in the ADAM sputtering system.

Table 1. Three pumping modes of the cryo pump in the ADAM system.

Pumping mode	HV gate valve	Bypass valve	Usage
High-speed	open	open	When UHV is needed
Low-speed	closed	open	maintain a constant Ar pressure during sputtering
Not pumping	closed	closed	When main chamber is vented but cryo pump regeneration is not necessary

At a given pumping speed for the vacuum pumps, there are several sources that may limit the pressure in a vacuum system, such as leaks, the material outgassing, and the trapped gasses [38]. The chambers in ADAM system are made of stainless steel with standard sized conflat flanges and sealed by knife edges penetrating copper gaskets. The leaks can be kept at minimum when all vacuum components are assembled properly. The outgassing of materials has two contributions, a) evaporation of the materials and b) release of absorbed gasses [40]. The former is an intrinsic property of the material, so materials with high vapor pressure should be avoided in vacuum systems, such as Zn, Pb and organic materials. The latter increases the pumping time needed for achieving a good vacuum. The solution is to bake the chamber for a period of time (hours to days). The baking speeds up the outgassing process by degassing the system at an elevated temperature (150 °C - 250 °C). Table 2 shows a comparison of the typical background pressure and partial pressure of different gas molecules in ADAM system before and after overnight baking. The most noticeable pressure drop occurs for water vapor, which is the most significant gas absorbed in the chamber before baking. On the other hand, all vacuum components should be kept dry and clean before using in vacuum. The trapped gas molecules

can be most commonly found around the thread of a bolt and the pit behind the bolt. Therefore, only the bolts designed for vacuum are used in the ADAM system.

Table 2. The comparison of the typical background pressure and partial pressure of different gas molecules in ADAM system before and after overnight baking.

Background pressure (Torr)	Partial pressure (Torr)				
	H ₂	H ₂ O	N ₂ /CO	O ₂	CO ₂
Before baking	4×10^{-7}	1×10^{-7}	1×10^{-6}	6×10^{-8}	1×10^{-8}
After baking	5×10^{-9}	1×10^{-8}	3×10^{-9}	3×10^{-9}	$< 10^{-10}$

2.1.2 Sputtering process

Sputtering is a process where the target is bombarded with energetic particles in order to eject target materials. For non-reactive sputtering, the energetic particles are usually heavy inert gas such as Ar and Kr. The simplest sputtering system is a diode discharge system. The target material is mounted on the cathode with a negative voltage applied. The substrate and sample holder are grounded and act as the anode. In a vacuum system filled with rarefied Ar gas (a few mTorr), a small number of electrons, accelerated by the cathode, ionize the Ar atoms and producing more secondary electrons. The secondary electrons then go through a cascade process which ionizes all Ar atoms. The Ar ions carrying positive charges are also accelerated toward the target. The ejected target materials carry no charge, so they travel to the substrate freely with the momentum transferred from the Ar ions, excluding some of the materials scattered by Ar ions before they arrive at the substrate.

A more commonly used sputtering system is magnetron sputtering. It differs from the diode sputtering with the addition of a few magnets in the cathodes. The schematic of the magnetron sputtering system is given in Fig. 6. The configuration of the magnetic field confines the electrons around the cathode. Due to the electric and magnetic field, the electrons travel in a

spiral pattern giving them a greater chance of colliding with Ar atoms. Thus, compared to the diode sputtering, the magnetron sputtering allows much higher deposition rate and more efficient use of the target.

In the ADAM system, there are four magnetron guns compatible with 1.5-inch-diameter targets. The magnets in the cathode are permanent magnets which provide magnetic fields up to 0.2 T at the surface of the target. The cathode is circulated by cooling water in order to prevent the magnets from overheating and demagnetizing. For DC sputtering, the magnetron guns are powered by Advanced Energy MDX 500 power supplies. The power supply is set at a fixed power for each target. Depending on the target material and thickness, the current and voltage of the target differs greatly. The cathode voltage determines the energy the Ar ions carrying when bombarding the target, while the cathode current indicates the number of Ar ions hitting the target per unit time. Therefore a constant deposition rate is expected at a given sputtering power, since the power is simply the product of voltage and current. On the other hand, the cathode current and voltage are very important for monitoring the plasma status and estimating the lifetime of the targets. Usually, when the targets get thinner, the magnetic field at its surface becomes larger. As a result, more electrons are confined around the target and eventually more current goes through the target. In our case, at the sputtering power of 60 W, the cathode current changes from around 120 mA for a new Dy target to 145 mA before it burns through, and from 210 mA for a new Y target to 260 mA before it burns out. In the ADAM system, a homemade Labview program is used to regulate the sputtering process, including controlling the deposition time and power, and recording the sputtering current and voltage.

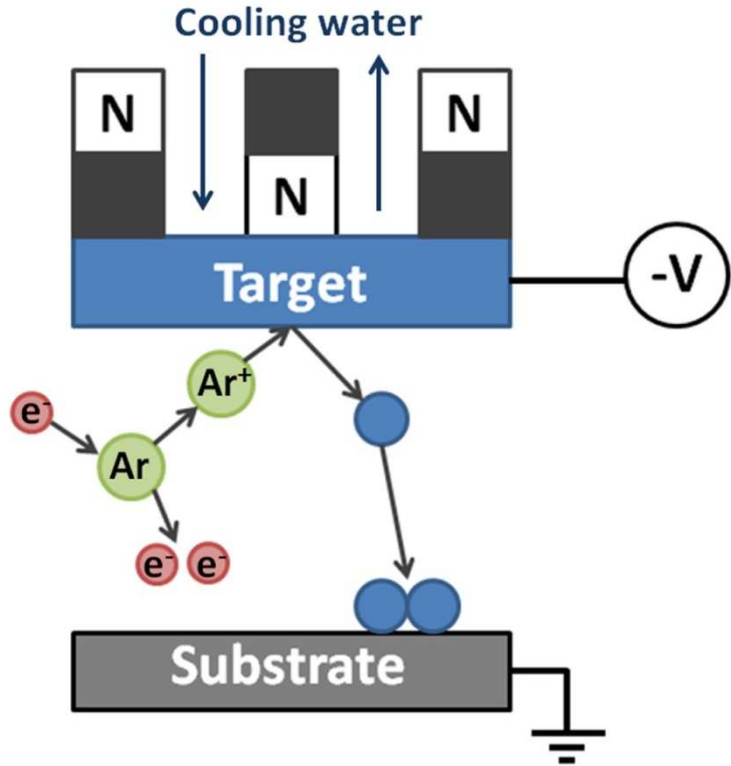


Figure 6. The magnetron sputtering process in the ADAM system.

2.1.3 Epitaxial thin film growth

The fabrication of single-crystal thin films is of great interest to the semiconductor device industry as well as fundamental scientific researches. In this dissertation, single-crystal Dy thin film is required since the magnetic moments of Dy atoms, which lie in the Dy (0002) plane, need to be ordered. The straightforward approach to obtain single crystalline films is to start with crystalline substrates. In appropriate conditions, the deposited layer may inherit the lattice structure of the substrate and form a crystalline thin film, i.e. the epitaxial thin film. Similarly, more single-crystal layers can be stacked on each other to form an epitaxial multilayer. For epitaxial growth, there are always certain translational relationships between the crystal lattices

of the adjacent layers of materials. For example, Cu (100) is known to grow epitaxially on Si (100) while Cu (111) can be grown on Si (110) or Si (111) [41, 42].

Epitaxial growth could be realized by many deposition methods including but not limited to MBE, sputtering and CVD. Here we focus on discussing the factors affecting the epitaxial growth in sputter deposition. Depending on the substrate temperature, surface energy, interfacial energy, lattice mismatch, deposition flux and deposition gas pressure, there can be several growth modes in epitaxy. When the substrate temperature is sufficiently high to achieve thermodynamic equilibrium, the growth modes are determined by the surface energy of the substrate ($\gamma_{substrate}$) relative to the surface energy of the film (γ_{film}) plus the interfacial energy ($\gamma_{interface}$) [43]. When the condition of wetting is satisfied, where

$$\gamma_{substrate} < \gamma_{film} + \gamma_{interface}, \quad (8)$$

small lattice mismatch leads to layer-by-layer growth while large lattice mismatch results in a mixed layer-island growth. If equation (8) is not satisfied, the film has a tendency to nucleate hence the island growth. The island growth may also be seen in the metastable growth, which typically occurs at low substrate temperature or high deposition flux where the surface atoms do not have enough energy or time to reach the thermodynamic equilibrium. Although the island growth and columnar growth are useful in quantum dots [44] and perpendicular magnetic recording media [45] respectively, the layer-by-layer mode is desired for the Dy/Y multilayers since the magnetic moments of Dy need to be resolved in each atomic layer. In addition, the vacuum condition and surface cleanliness are critical for the purpose of maintaining a contamination free interface.

In the ADAM system, the substrates are heated by a homemade heater assembly shown in Fig. 7. The heater core is a halogen lamp with the maximum power of 1000 W. The input

voltage of the lamp is controlled by a variable transformer. The cylindrical heater box is folded by tantalum sheets of three layers for the purpose of shielding. The top of the heater box is open and allows the sample holder to be heated through thermal radiation. The titanium sample holder sits on a rotational stage which rotates when sputtering in order to improve the uniformity of the film. The rotational stage is hollow at the center where the wiring for the heater lamp and the thermocouple go through, as well as a supporting pole for the stationary heater box. Calibrated by thermocouples with respect to the applied voltage, this heater assembly is capable of heating the substrate up to 1000 °C when 50 % power is applied*. This heater setup can be not only used for heating the substrate during sputtering, but also for degassing the chamber and in-situ annealing.

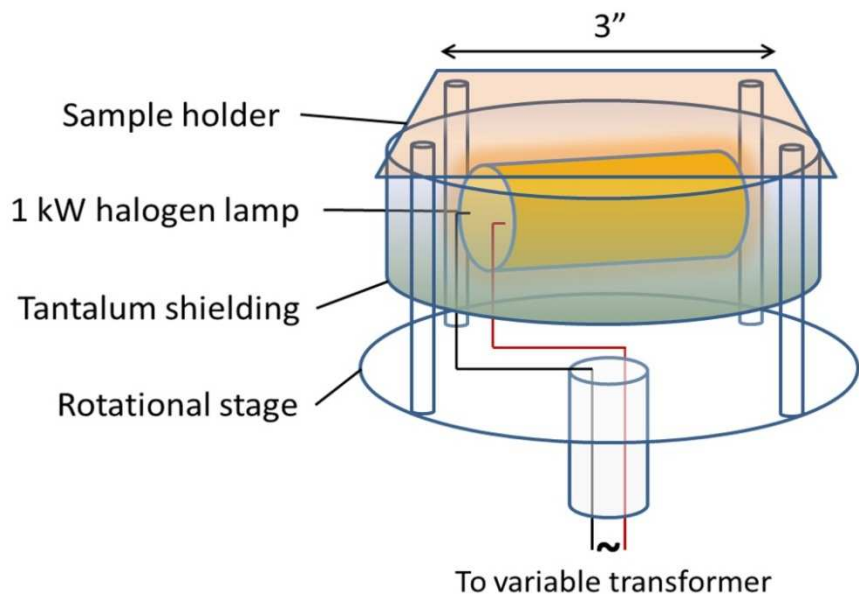


Figure 7. The design of the heater assembly and the rotational stage in the ADAM system.

* The halogen lamp can be damaged if the temperature goes above 1000 °C.

2.2 Structural characterizations

2.2.1 X-ray reflectivity

When an X-ray is incident onto the thin film surface at a grazing angle ($0^\circ - 15^\circ$), the optical path difference between the X-ray reflected by the interfaces is of the same order of magnitude of the X-ray wavelength, thus the reflected X-ray can constructively or destructively interfere at slightly different incident angles. The oscillations of the X-ray reflectivity (XRR) is called Kiessig fringes, which can be used to evaluated the thickness of the film as well as the interfacial morphology. The schematic of XRR for thin film is shown in Fig. 8. Note that the incident angles here are defined as the angles between the X-ray beam and the interface plane, instead of interface normal which is the case in conventional optics. The condition for constructive interference is given by

$$2nD\sin\theta_t = m\lambda, (m = 1,2,3 \dots), \quad (9)$$

where n and D are the refractive index and the thickness of the film respectively, while m is the order of Kiessig fringes. Applying Snell's law,

$$\cos\theta_i = n\cos\theta_t, \quad (10)$$

equation (9) becomes:

$$2D\sqrt{\sin^2\theta_i - 1 + n^2} = m\lambda, (m = 1,2,3 \dots). \quad (11)$$

Note that the critical angle for total reflection is given by $n = \cos\theta_c$. Therefore,

$$2D\sqrt{\sin^2\theta_i - \sin^2\theta_c} = m\lambda, (m = 1,2,3 \dots). \quad (12)$$

In terms of the scattering vector ($Q = 4\pi\sin\theta/\lambda$), we have

$$Q_i^2 - Q_c^2 = \left(\frac{2\pi m}{D}\right)^2, (m = 1, 2, 3 \dots). \quad (13)$$

Here Q_i is the incident scattering vector corresponding to the m th Kiessig fringe. The critical angle Q_c and the film thickness D can both be determined by extrapolating the Q_i^2 versus m^2 curve. For the superlattice sample of N repeats, $D = N\Lambda$, where Λ is the superlattice period.

$$Q_i^2 - Q_c^2 = \left(\frac{2\pi m}{N\Lambda}\right)^2 = \left(\frac{2\pi M}{\Lambda}\right)^2, (M = 1, 2, 3 \dots). \quad (14)$$

where $M = m/N$ is the order of the Bragg peak, which is due to the constructive reflection from the top and bottom interface of a bi-layer.

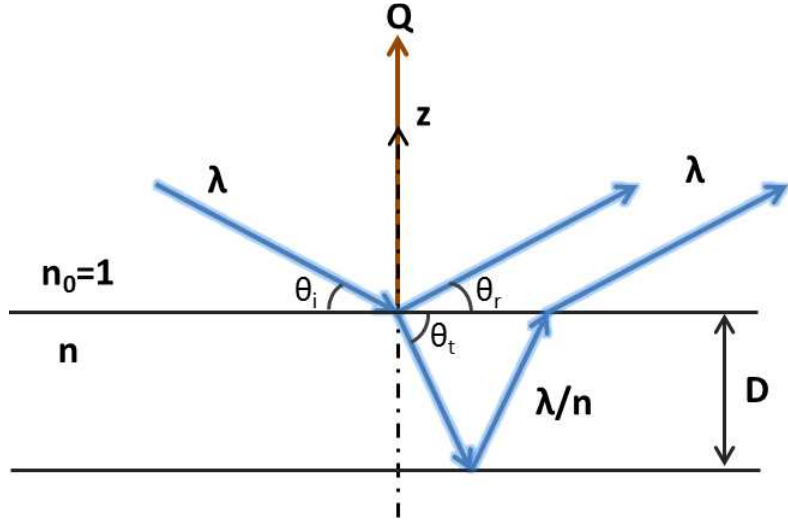


Figure 8. The schematic of the X-ray reflected by a thin film.

The accurate determination of the XRR intensity is discussed in the following. For a single boundary case, the wave functions of X-ray during reflection can be written as

$$\Psi_1 = A e^{ik_i z} + B e^{ik_r z}, \quad (15)$$

$$\Psi_2 = C e^{ik_t z}, \quad (16)$$

in media 1 and 2 respectively. Applying the boundary conditions that the wave function and its first derivative are both continuous at the interface ($z = 0$), the Fresnel reflectivity coefficient can be derived,

$$r = \frac{B}{A} = \frac{k_i - k_t}{k_i + k_t}. \quad (17)$$

For a double boundary case, i.e. semi-infinite top and bottom layers and a middle layer of thickness t , the reflectivity coefficient oscillates due to the interference effect, and is given by

$$r = \frac{r_{01} + r_{12}e^{i2k_1 t}}{1 + r_{01}r_{12}e^{i2k_1 t}}. \quad (18)$$

Equation (17) and (18) can be extended into the n-boundary (multilayer) case, which is given by the Parratt recursion relation* [46],

$$R_{n-1,n} = \frac{r_{n-1,n} + R_{n,n+1}e^{i2k_n t_n}}{1 + r_{n-1,n}R_{n,n+1}e^{i2k_n t_n}}, \quad (19)$$

where

$$r_{n-1,n} = \frac{k_{n-1} - k_n}{k_{n-1} + k_n}, \quad (20)$$

$$k_n = \sqrt{k_0^2 - 4\pi\rho_n}. \quad (21)$$

Here ρ_n is the X-ray scattering length density (SLD) for the nth layer, and R is the reflectivity. The X-ray SLD is material dependent. For a multilayer thin film, the SLD profile is a function of the surface normal, i.e. $\rho(z)$. For a certain incident angle,

$$R = |r|^2 = \frac{\text{reflected intensity}}{\text{incident intensity}}. \quad (22)$$

On one hand, the reflectivity R is directly measured by the detector. On the other hand, R can be calculated from the trial SLD profile $\rho(z)$ using the Parratt recursion relation. By fitting the

* The subscript n denotes the layer number.

calculated reflectivity to the measured one, the SLD profile can be accurately determined.

In this work, all X-ray characterizations were performed on a Philips X'pert X-ray diffractometer (see Fig. 9) with Cu target ($\lambda \approx 1.541 \text{ \AA}$). The chemical depth profiles, including thickness and roughness information, were extracted for all Dy/Y superlattices with the help of the model fitting software Wingixa, which is based on the Parratt formalism modified to include roughness.

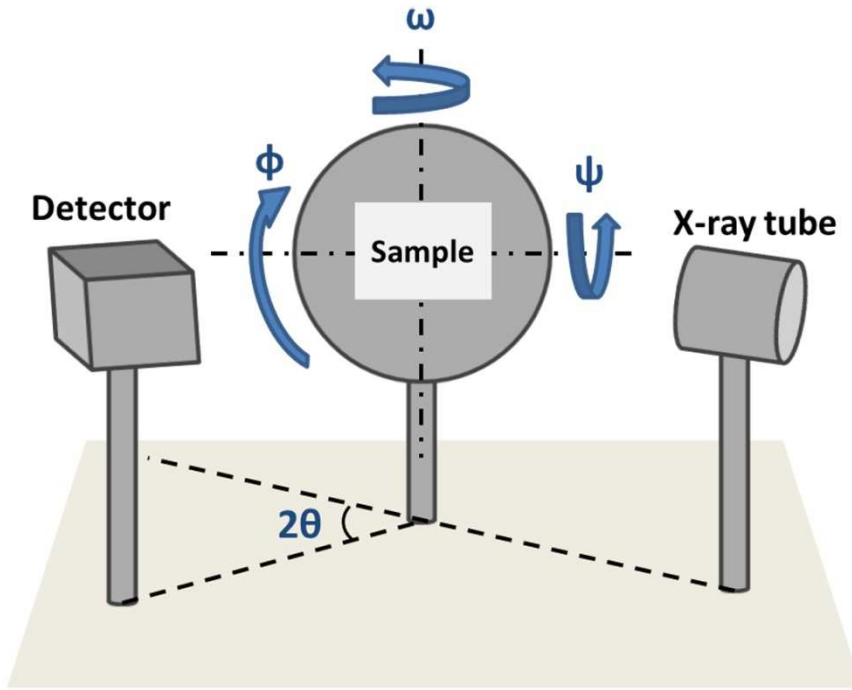


Figure 9. The schematic of the Philips X'pert X-ray diffractometer.

2.2.2 X-ray diffraction

In contrast to XRR, X-ray diffraction (XRD) measures the constructive diffraction from the atomic planes in the crystal lattice. The XRD usually occurs at higher angles ($> 15^\circ$) compared to XRR. The condition of XRD peak of nth order is given by the Bragg law [47],

$$2dsin\theta_i = n\lambda \text{ or } \mathbf{Q} = \mathbf{G}, \quad (23)$$

where d is the spacing between the atomic planes along the direction of the scattering vector, and \mathbf{G} is the corresponding reciprocal lattice vector. The XRD intensity per unit cell is determined by the structure factor [48],

$$S_{\mathbf{G}} = \sum_j f_j(\mathbf{G}) e^{-i\mathbf{G}\cdot\mathbf{r}_j}, \quad (24)$$

where \mathbf{r}_j is the scattering center and f_j is the atomic form factor, which is a function of the electron density $n_j(\mathbf{r} - \mathbf{r}_j)$:

$$f_j(\mathbf{G}) = \iiint n_j(\mathbf{r} - \mathbf{r}_j) e^{-i\mathbf{G}\cdot(\mathbf{r}-\mathbf{r}_j)} dV. \quad (25)$$

For superlattice thin films, the bi-layer modulation gives rise to a set of satellite peaks around the main XRD peak. The positions of the satellite peaks are given by [49],

$$\frac{2sin\theta_n}{\lambda} = \frac{1}{d} \pm \frac{n}{\Lambda} \text{ or } Q_n = \frac{2\pi}{d} \pm \frac{2\pi n}{\Lambda}, \quad (26)$$

where n is the order of the satellite. The main diffraction peak is given by n = 0. The average lattice constant is $\bar{d} = \Lambda/(N_A + N_B)$, where N_A and N_B are the number of atomic planes of material A and B in one bi-layer. Therefore, the separation between the main peak and the nth-order satellite peaks is given by:

$$\Delta Q = \frac{2\pi n}{\Lambda}. \quad (27)$$

In this dissertation, XRD was used as the tool to confirm the orientation of the epitaxial growth and evaluate the quality of the single-crystal thin film. The deposition conditions for Dy/Y superlattice were optimized based on the XRD results.

Fig. 9 shows the schematic of the Philips X'pert X-ray diffractometer. The sample stage has six degrees of freedom, i.e. moving along x, y, z-direction, and rotating about ω , ϕ , and ψ -axes. In XRD, the intensity is scanned with respect to 2θ , or $|\mathbf{Q}|$, while the direction of the scattering vector is fixed along the normal of a specific set of crystal planes, i.e. $\mathbf{Q} \parallel \mathbf{G}$. The diffraction peaks appear at the angles at which $|\mathbf{Q}| = |\mathbf{G}|$ is satisfied.

2.2.3 Rocking curve

The rocking curve measures the distribution of a specific crystal axis. In the deposited single-crystal thin films, a certain variation of the crystal orientation always exists. The rocking curve is scanned by setting the scattering vector equal to the reciprocal lattice vector in magnitude, i.e. $|\mathbf{Q}| = |\mathbf{G}|$, and rocking the angle of the \mathbf{G} vector. In practice, while the detector and the X-ray tube are fixed at the angles given by the Bragg condition, the scan is performed by rocking the sample about the ω -axis (see Fig. 9). The width of the rocking curve peak indicates the distribution of the crystal orientations.

2.2.4 Pole figure

Normal XRD probes the crystal planes parallel with the sample surface. In contrast, the pole-figure scans the crystal planes non-parallel to the sample surface. Consider a simple cubic crystal for example (Fig. 10). Suppose the (100) plane is parallel with the sample surface but the (111) plane is not. In order to scan the (111) plane, the scattering vector needs to be set at $|\mathbf{Q}| = |\mathbf{G}_{111}|$ and tilted from the surface normal by an angle ψ :

$$\psi = \cos^{-1}\left(\frac{\mathbf{G}_{100} \cdot \mathbf{G}_{111}}{|\mathbf{G}_{100}| |\mathbf{G}_{111}|}\right) \approx 54.7^\circ. \quad (28)$$

In this case, when the crystal rotates about the surface normal for one cycle, there are four positions where $\mathbf{Q} = \mathbf{G}_{111}$, hence four pole-figure diffraction peaks. In practice, the pole-figure is scanned with the sample tilted by angle ψ and rotating the azimuthal angle ϕ . By measuring the pole-figure, the crystallinity of the sample can be evaluated in three dimensions.

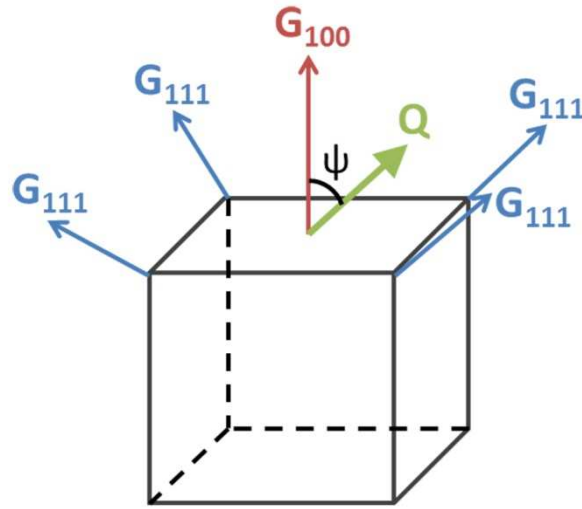


Figure 10. The illustration of the pole figure scan for the (111) planes of a simple cubic structure while the film surface is the (100) plane.

2.3 Magnetic characterizations

The macroscopic magnetic properties of the Dy/Y superlattices were characterized by low-temperature magnetometers. The in-plane net magnetization was measured as a function of temperature for both heating and cooling process with various fields applied in the film plane.

2.3.1 Low-temperature vibrating sample magnetometer (VSM)

One of the low-temperature magnetometers used in this work is the Quantum Design DynaCool physical property measurement system (PPMS) with the VSM option. It follows the same basic principle as a conventional VSM, i.e. Faraday's law:

$$V = -\frac{d\Phi}{dt}, \quad (29)$$

where V is the voltage induced in the pickup coil, and Φ is the magnetic flux enclosed in the pickup coil. By sinusoidally vibrating the position of the magnetic sample, the induced voltage in a suitably placed pickup coil is measured as a function of time, from which the magnetization of the sample can be derived. However, the configuration of the pickup coils and the vibrator in the DynaCool differs from the conventional VSM. Unlike the resonant voice-coil vibrator used in the regular VSM, the vibration in the DynaCool VSM is operated by a linear motor at 40 Hz. In the conventional VSM, the four pickup coils are oriented with the coil axis perpendicular to the vibration axis. In contrast, the pickup coils in the DynaCool system are the first-order gradiometer type with the coil axis parallel to the vibration axis. The pickup coils are counter-wound in order to minimize the background signal, such as voltages induced by the external magnetic field. The schematic of the DynaCool system is shown in Fig. 11. With the above setup, the DynaCool VSM is able to resolve the magnetization change as small as 10^{-7} emu at a data rate of 1 Hz [50]. The superconducting magnet in the system provides a magnetic field up to 9 T.

The refrigeration system in the DynaCool VSM is a closed-loop cryogenic system, which allows very efficient consumption of the helium. The system consists of two main components, the compressor and the cold head. The cryogen used in the system is the helium with 99.999 % purity. The helium gas is compressed in the compressor and then sent to the cold head through the helium flex line, which is made of stainless steel. In the cold head, the high-pressure helium gas goes through an adiabatic expansion which removes heat from the cold head. The low-pressure helium returns to the compressor through the helium flex line and starts another compression-expansion cycle.

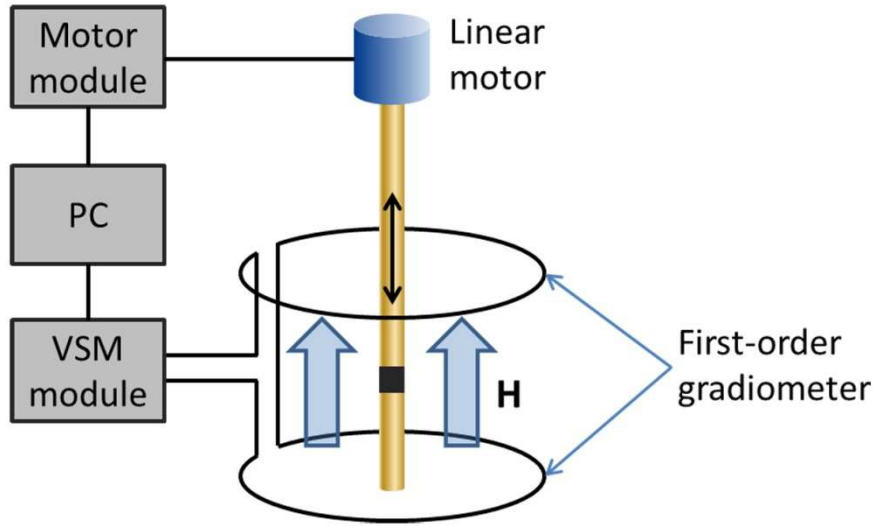


Figure 11. The schematic of the VSM measurement in the Quantum Design DynaCool PPMS system.

2.3.2 Superconducting quantum interference device (SQUID)

Another low-temperature magnetometer used to characterize the Dy/Y superlattices is the Quantum Design magnetic property measurement system (MPMS). It is a radio frequency (RF) superconducting quantum interference device (SQUID), equipped with a cryogenic system and a superconducting magnet. The model is capable of measuring magnetic moment as low as 10^{-7} emu from 4.2 K to 350 K with an applied field up to 5 T [51]. Fig. 12 shows the schematic of the MPMS. A second-order gradiometer is used as the pickup coil, which is less sensitive to the background signal, compared to the first-order gradiometer. During measurements, the sample is moving through the coil along the z-direction. The induced current in the gradiometer is measured as a function of z-position and transformed into voltage signal by the RF SQUID, which operates on a single Josephsen junction based on the AC Josephsen effect [52]. The amplified voltage signal is calculated based on the model of a magnetic dipole passing through a

second-order gradiometer, from which the magnetic moment of the sample is accurately determined.

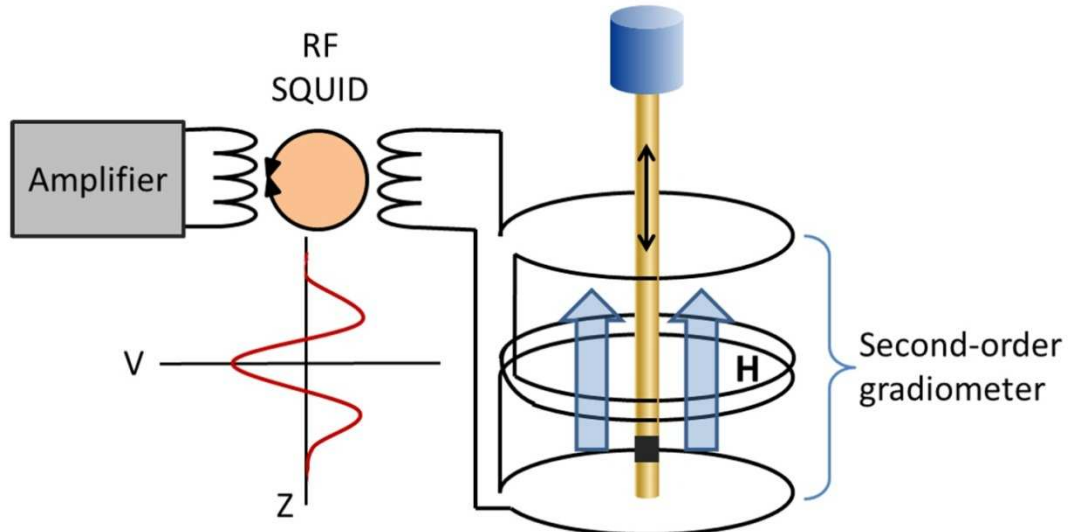


Figure 12. The schematic of the magnetization measurement in the Quantum Design MPMS SQUID system.

3. NEUTRON SCATTERING

3.1 Introduction to neutron scattering techniques

Similar to X-ray diffraction, neutron scattering is another powerful tool to investigate the microscopic structure of materials. While X-ray senses the distributions of electrons in materials, neutrons see the nuclei and magnetic moments. Thanks to the properties of neutrons, neutron scattering techniques lead to a unique path to explore the complex magnetic structures in the atomic scale and the dynamic properties of solids, which are very difficult to access via other experimental techniques. The important properties of neutrons and the corresponding advantages are summarized in Table 3. Since the 1950s when neutron scattering was first applied to materials research, many branches of neutron scattering techniques have been developed, accompanied by the advance in the neutrons facilities which produce sufficient neutron flux for the applications [12]. For instance, the elastic neutron diffraction measures the crystallography, texture and strain in materials. Inelastic neutron scattering is used for studying the motion of atoms. Neutron reflectivity is specialized on the surface and interface properties of multilayer systems. Small angle neutron scattering (SANS) is aimed at structures of larger length scale (10 nm – 1 μm). On the other hand, the magnetic neutron scattering is incorporated in the nuclear neutron scattering, due to the interaction between the neutron moment and the magnetic moment in the materials. Thus the magnetic signals can be detected by neutron at the same time, such as magnetic structures or magnetic excitations. In our study, elastic neutron diffraction was measured to characterize the crystallography and magnetic structures in both bulk Dy single

crystal and Dy/Y superlattices. Polarized neutron reflectometry (PNR) was applied to extract the magnetization depth profile of the Dy/Y superlattices.

Table 3. The important properties of neutrons and the corresponding advantages when applied to condensed matter physics.

Properties of neutrons	Advantages of neutrons
Neutrons interact with atomic nuclei through short range forces.	Neutrons can distinguish isotopes.
Neutrons are charge neutral.	Neutrons are highly penetrative, non-destructive, and can be used at the presence of electric fields.
Neutrons have magnetic moment, and interact with the B field caused by unpaired electrons via a magnetic dipole interaction.	Neutron senses the distribution of magnetization in materials.
Neutrons have spin.	Neutrons can be polarized and used for coherent scattering.
The wavelength of neutrons can be tuned comparable to the atomic spacing of materials.	Neutrons can probe crystal structures.
The energies of thermal neutrons are similar to the energies of excitations in solids.	Neutrons can probe lattice vibrations.

3.2 Principles of polarized neutron reflectometry (PNR)

PNR is developed by G. P. Felcher to analyze the chemical and magnetic structure of the multilayers in the atomic scale [53]. PNR is a relatively new technique but has seen great improvement in the recent years [54, 55]. Analogous to the chemical depth profile extracted from

XRR, specular reflectivity of neutrons is in essence a surface depth profiling technique. PNR was proved to be a powerful tool to detect the configuration of non-uniformly aligned moments in the antiferromagnetically coupled Fe/Cr superlattices [33]. On the other hand, the imperfections in the surface and lateral inhomogeneities result in scattering off the specular direction. The correlated lateral inhomogeneities show up in the reflectivity in terms of off-specular patterns. The off-specular scattering measured along with PNR provides the information about the lateral magnetic domains in the structure [33, 35]. PNR is also capable of measuring the chirality of the helical structure in Dy/Y superlattices in a non-conventional geometry [29, 30].

Consider the simplest case when a neutron beam of wavevector \mathbf{k} is reflected by the interface between two media, with the refractive index of n_1 and n_2 respectively, as shown in Fig. 13. Notice that the incident angles here are defined as the angles between the beam and the interface plane, instead of interface normal which is the case in conventional optics. For smooth surface, specular reflection occurs, where the angle of reflection is equal to the angle of incidence (Fig. 13 left). The scattering vector is perpendicular to the surface plane, and the magnitude is given by

$$Q = Q_z = 2k_z = 2ksin\theta_i = \frac{4\pi}{\lambda} sin\theta_i. \quad (30)$$

If the surface is rough, part of the beam is reflected at different angles from the incident angle. This is the off-specular scattering or diffuse scattering (Fig. 13 right). In this case, \mathbf{Q} is tilted from the surface normal, and the in-plane and out-of-plane components can be written as:

$$Q_x = k(cos\theta_r - cos\theta_i), \quad (31)$$

$$Q_z = k(sin\theta_r + sin\theta_i). \quad (32)$$

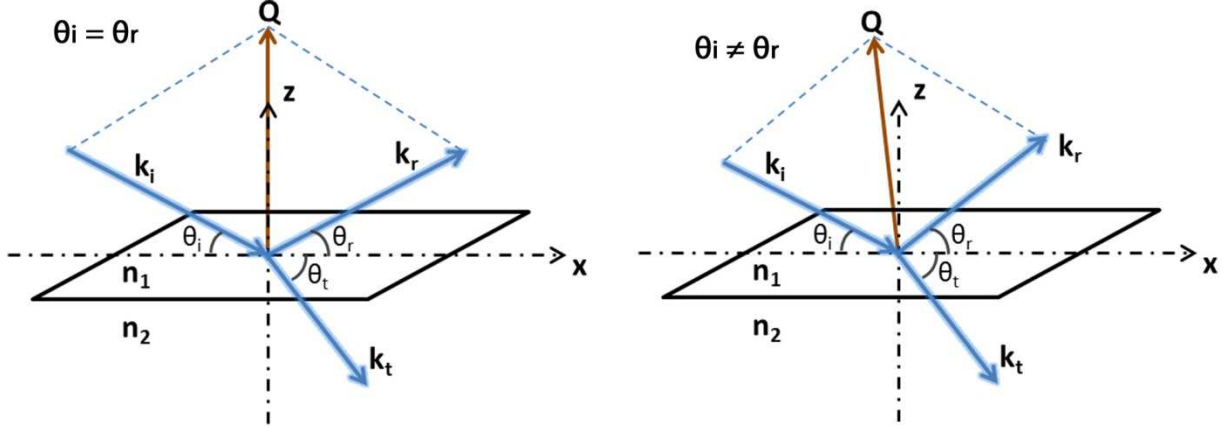


Figure 13. The schematics of the specular refection (left) and the off-specular (diffuse) scattering (right).

When a neutron is incident from vacuum and interacts with the nuclei in the layered material, it sees the Fermi pseudo-potential [56], which is proportional to the nuclear scattering length density (SLD) of the material [57],

$$V(z) = \frac{2\pi\hbar^2}{m} Nb = \frac{2\pi\hbar^2}{m} \rho(z). \quad (33)$$

Here N is the number of atoms per unit volume in the material and b is the neutron coherent scattering length. m is the mass of a neutron. Assuming the layered material is homogenous in the film plane, the SLD and the Fermi pseudo-potential are only functions of the depth (z) into the film. The z component of the neutron kinetic energy in free space is given by

$$E_z = \frac{\hbar^2 k_0^2}{2m}, \quad (34)$$

where k_0 stands for the z component of the neutron wavevector in free space. The wavevectors discussed in the following all represent their z components. Plug equation (33) and (34) into the time-independent Schrodinger equation in z direction,

$$-\frac{\hbar^2}{2m} \nabla^2 \Psi(z) + V(z)\Psi(z) = E\Psi(z), \quad (35)$$

we have

$$\frac{\partial^2}{\partial z^2} \Psi(z) + [k_0^2 - 4\pi\rho(z)]\Psi(z) = 0. \quad (36)$$

Define k_n as the wavevector of neutron in the medium of refractive index n , where

$$k_n^2 = k_0^2 - 4\pi\rho. \quad (37)$$

The Schrodinger equation is then reduced to a Helmholtz equation,

$$\frac{\partial^2}{\partial z^2} \Psi + k_n^2 \Psi = 0. \quad (38)$$

The solution is a free travelling wave function with wavevector k_n . If the neutron is incident from vacuum, the refractive index (n) of the medium for neutron and the critical angle (θ_c) for total reflection can be expressed in terms of the SLD of the medium and the neutron wavevector, i.e.

$$n = \frac{k_n}{k_0} = \sqrt{1 - \frac{4\pi\rho}{k_0^2}}, \quad (39)$$

$$\cos\theta_c = n, \text{ or } \sin\theta_c = \sqrt{\frac{4\pi\rho}{k_0^2}}. \quad (40)$$

The discussion above only involves the neutron-nucleus interaction. Associated with an intrinsic spin angular momentum, neutron can only occupy one of two discrete energy states within a given magnetic field [12]. Taking into account of the magnetic interaction, the Fermi pseudo-potential needs to be modified by adding a magnetic term*,

$$V_m = \mp \mu_N \cdot \mathbf{B} = \mp \mu_0 \mu_N M \cos\theta, \quad (41)$$

where M is the magnetization of the sample and θ is the angle between magnetization and the

* The subscripts N, n, m denote neutron, nuclear and magnetic respectively.

neutron moment. By introducing the magnetic scattering length density,

$$\rho_m = \mp \frac{m}{2\pi\hbar^2} \mu_0 \mu_N M \cos\theta, \quad (42)$$

the total potential energy can be written in the same form of the nuclear Fermi pseudo-potential, i.e.

$$V_{tot} = V_n + V_m = \frac{2\pi\hbar^2}{m} \rho_n \mp \mu_0 \mu_N M \cos\theta = \frac{2\pi\hbar^2}{m} (\rho_n + \rho_m). \quad (43)$$

Thus, the principle above still holds true at the presence of magnetic scattering, except that the SLD includes two terms, nuclear SLD and magnetic SLD. The latter has the similar order of magnitude as the former, and proportional to the magnetization of the sample, as shown in equation (42). The \pm sign in equation (41) through (43) indicate that the neutrons of opposite spin states see reversed magnetic potentials, hence giving different reflectivity spectrum. The difference in the reflectivity reflects the magnetization of the sample. For this application, the PNR is designed to measure the magnetization depth profile of the sample. Thanks to the magnetic depth profiling capability, PNR is especially useful in resolving the complex magnetization distribution over the film thickness, such as the helical magnetic moment in the epitaxial MnSi thin film [58] and the exchange bias in spin-valves [59-61].

The Parratt recursion relation in equation (19), (20) and (21) is also true for neutron reflectivity, with the reflectivity defined as:

$$R = |r|^2 = \frac{\text{number of reflected neutrons}}{\text{number of incident neutrons}}. \quad (44)$$

In neutron reflectivity experiment, R is directly measured in terms of the intensity by the detector at different incident angles. However, R carries no phase information about r, making the SLD-solving task very challenging.

The neutron reflectivity coefficient can also be written in the integral expression [12]. In one dimensional case,

$$r(Q) = \frac{4\pi}{iQ} \int_{-\infty}^{\infty} \Psi(Q, z) \rho(z) e^{-ik_0 z} dz. \quad (45)$$

In the Born approximation limit, where Q is large enough that the incident neutron wave function in medium is not significantly distorted from its free-space form, the wave function in medium can be substituted by the wave function in vacuum [12], i.e.

$$\Psi(Q, z) \approx e^{-ik_0 z}. \quad (46)$$

Notice that $Q = 2k_0$ along z direction. Therefore,

$$r(Q) = \frac{4\pi}{iQ} \int_{-\infty}^{\infty} \rho(z) e^{-iQz} dz. \quad (47)$$

The SLD profile $\rho(z)$ can be retrieved from $r(Q)$ by Fourier transform. Again, the phase information of $r(Q)$ is lost during the measurement of $|r(Q)|^2$. In the case of three dimensional scattering, equation (47) remains the same form, except that $\rho(z)$ is the average in-plane SLD, i.e.

$$\overline{\rho(z)} = \frac{1}{S} \iint_{-\infty}^{\infty} \rho(x, y, z) dx dy, \quad (48)$$

where S is the surface area in the plane of material slab.

The data analysis for neutron reflectivity is the so-called inverse problem. The aim is to reconstruct $\rho(z)$ from the measured reflectivity $R(Q)$. The conventional approach involves modeling and nonlinear least-square fitting [12]. Fig. 14 shows the flow chart of the approach. Starting from the designed sample model, the corresponding SLD profile is determined. The reflectivity is calculated using the Parratt recursion relation. The calculated reflectivity is compared to the measured and then the sample model is refined. Due to the loss of the phase

information in measured $R(Q)$, there is a set of $r(Q)$ that gives identical $R(Q)$. Thus the solution for $\rho(z)$ is not unique. To overcome this problem, the number of independent parameters in the sample model needs to be minimized and their ranges should be well-defined. In practice, the parameters are set based on the knowledge of the sample, which is gathered by other characterization techniques, such as XRR for structural information and magnetometer for magnetic information.

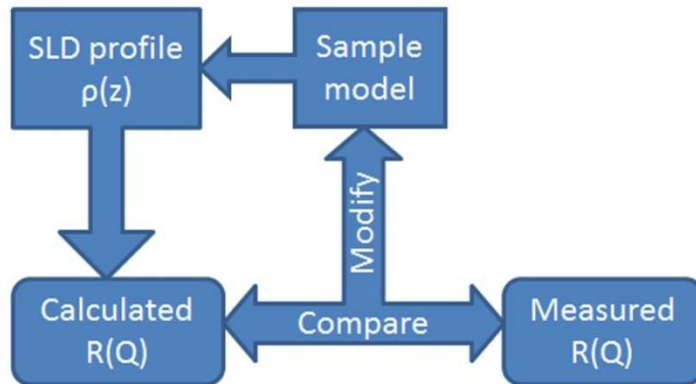
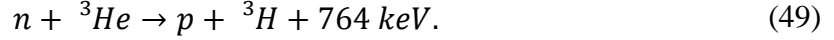


Figure 14. The flow chart for extracting the SLD profile from the neutron reflectivity data.

The off-specular scattering, on the other hand, is a measurement of the lateral inhomogeneity which can generally be described by a correlation function that characterizes the correlation of properties between two points [34, 35]. The correlation function of roughness can be obtained from a measured reciprocal-space distribution of diffuse scattering. Similarly, the magnetic off-specular scattering provides information about the magnetic inhomogeneity in the film plane, i.e. the in-plane magnetic domain structures [62-64]. For the Dy/Y superlattice, the magnetic off-specular scattering in terms of Bragg sheets around the magnetic peaks would prove the presence of the lateral helical domains with the shape and intensity determined by the magnetic lateral coherence length.

3.3 Polarized neutron reflectometer

The polarized neutron reflectometer is the instrument for measuring neutron reflectivity as a function of the momentum transfer during scattering. The neutrons are polarized in order to distinguish the magnetic reflection from the nuclear reflection. Depending on the approaches for varying the scattering vector \mathbf{Q} , there are two types of polarized neutron reflectometers, the monochromatic reflectometer and the polychromatic reflectometer. For monochromatic reflectometer, the neutron wavelength is fixed while the angle of incidence is changed. In contrast, the incident angle is fixed but the neutron wavelength is varying for the polychromatic reflectometers. The typical schematics of both types are shown in Fig. 15. For both reflectometers, the incident neutron beam is polarized by a polarizer and a spin flipper and collimated by multiple slits. The reflected neutron goes through a spin flipper and an analyzer before collected by the detector. The neutron detectors are usually operated with ${}^3\text{He}$ gas, based on the reaction:



The polarizer is typically a Fe/Si supermirror which selectively transmits neutrons of one spin channel. The spin flipper, if turned on, flips the neutron spin polarized by the polarizer. The analyzer chooses the neutron spins aligned with the polarizer from the reflected neutrons. With this setup, the neutron reflectivity can be measured in four channels, two non-spin-flip channels, R^{++} (R^{--}), corresponding to the number of spin up (down) incident neutrons reflected with spin up (down) polarization, and two spin-flip channels, R^{+-} (R^{-+}), associated with the number of neutrons experiencing a spin-flip during the reflection due to the magnetization in the sample [55]. In general, the reflectivity of the non-spin-flip channels reflects the average magnetization

parallel to the spin polarization. The reflectivity of the spin-flip channels reveals the magnetization perpendicular to the spin polarization [54].

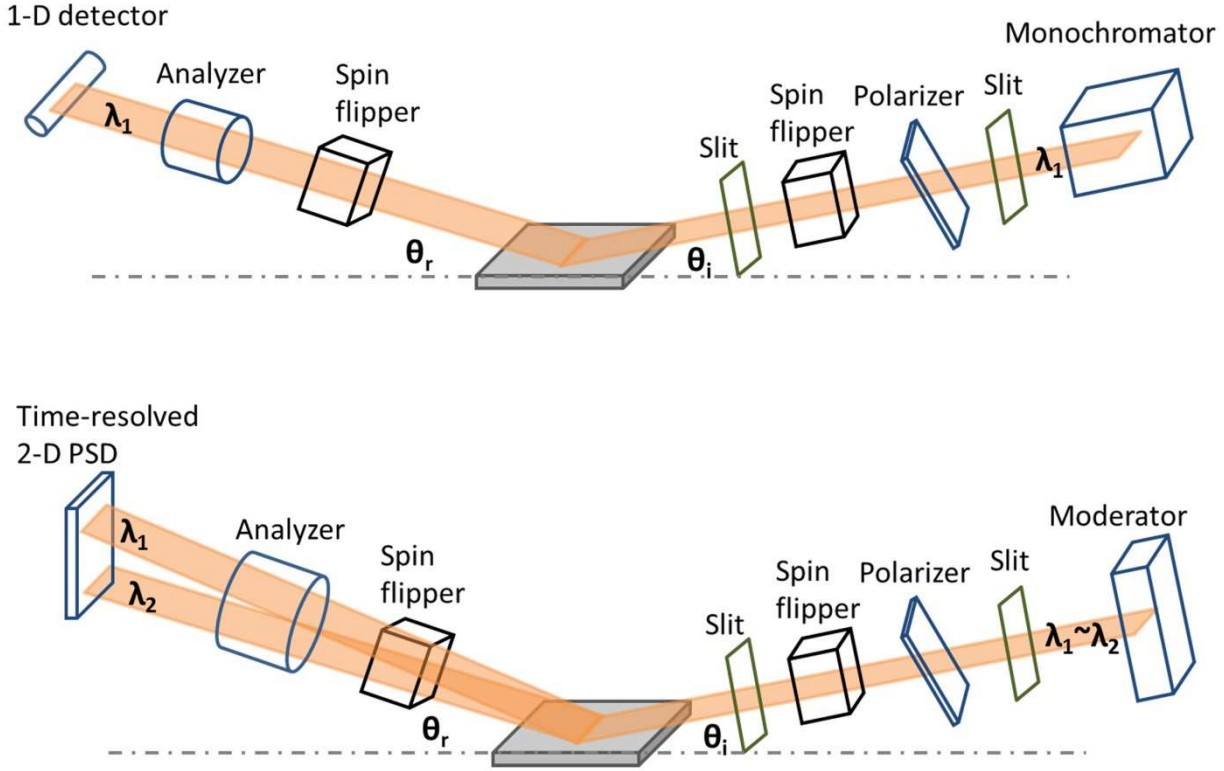


Figure 15. The typical schematics of a monochromatic (top) and polychromatic (bottom) reflectometer.

The monochromatic reflectometer is commonly seen at the reactor based neutron source which provides high-quality monochromatic neutrons, such as the Polarized Beam Reflectometer (PBR) in the National Institute of Standards and Technology (NIST). The scan mode of monochromatic reflectometer is the same as the XRR scan. In contrast, the polychromatic reflectometer is usually associated with the accelerator based spallation neutron source, such as the Magnetism Reflectometer (MR) at the Spallation Neutron Source (SNS) in ORNL. The accelerator based neutron source produces high intensity neutron pulses of continuously

distributed wavelengths. The moderators are used to cool down the hot neutrons. The neutron wavelength is identified by the time-of-flight (TOF) method in the polychromatic reflectometers. The relationship between TOF and the neutron wavelength is given by

$$TOF = \frac{s}{v} = \frac{sm}{p} = \frac{sm\lambda}{h}, \quad (50)$$

where s, v, p, m and h represent the distance between the moderator and the detector (21.265 m for MR), the neutron speed, the neutron momentum, the neutron mass, and the Planck constant, respectively. Coupled with the time-resolved two dimensional position-sensitive detector (PSD), the TOF method is capable of measuring both specular reflectivity and off-specular reflectivity over a wide range of Q at a given incident angle.

The PNR experiments in this dissertation were performed on the MR (beam line 4A) at the SNS. The neutron wavelength ranges from 1.8 Å to 14.0 Å in MR while the polarization is 98.5% [65]. The 2-D PSD is developed by the Brookhaven National Laboratory (BNL) and is 21 cm by 18 cm in dimension with 304×256 pixels [66]. A temperature controller ranging from 5 K to 750 k is used for the temperature dependent measurement. A magnetic field up to 1.15 T can be applied to the sample plane which is parallel or antiparallel to the polarization of the neutron. Note that in this experiment geometry, the neutron is not sensitive to the chirality of the helical spin in Dy/Y superlattice, which have to be measured with neutron polarized perpendicular to the helical magnetization [29, 30]. In our experiment, no analyzer was used to distinguish the spin state of the reflected neutrons, so the reflectivity is only in two independent channels: $R^+ = R^{++} + R^{+-}$ and $R^- = R^{--} + R^{-+}$. For the measurement on Dy/Y superlattices, based on the assumption of the domain configuration of different chiralities, there is no net magnetization perpendicular to the applied field. So the contribution of the spin-flip cross-sections (R^{+-} and R^{-+}) is negligible.

Although the TOF polychromatic reflectometer is more efficient than the monochromatic type in measuring the off-specular reflectivity, the data representation for the polychromatic reflectometer is not as straightforward as in the monochromatic type. For monochromatic instruments, the scan is performed along different incident angles and reflected angles, so the measured reflectivity is a function of the incident and reflected angles, i.e. $R(\theta_i, \theta_r)$. The condition for specular reflection is $\theta_i = \theta_r$, and the Bragg sheets of diffuse scattering is at $\theta_i + \theta_r = \text{constant}$. Using equation (51) and (52),

$$Q_x = \frac{2\pi}{\lambda} (\cos\theta_r - \cos\theta_i), \quad (51)$$

$$Q_z = \frac{2\pi}{\lambda} (\sin\theta_r + \sin\theta_i), \quad (52)$$

the reflectivity data can be transformed to the Q space, i.e. $R(Q_x, Q_z)$, with the specular condition being $Q_x = 0$ and the Bragg sheets at $Q_z = \text{constant}$. Here λ is the specific neutron wavelength used in the instrument.

For the polychromatic MR at SNS, the reflectivity is measured as a function of the detector pixel (X and Y) and TOF, i.e. $R(X, Y, \text{TOF})$. Fig. 16 (left) shows the reflectivity (color) data versus X and Y-pixel (TOF is not shown) taken at the MR at a given incident angle θ_i . The variation along X direction is essentially the change of the angle of reflection. The specular reflection is marked at $X = X_0$, which corresponds to $\theta_i = \theta_r$. Considering the geometry of the reflection, the relationship between X and the angle of reflection can be written as

$$\theta_r = \theta_i + \Delta\theta, \quad (53)$$

$$\Delta\theta = \tan^{-1} \left[\frac{(X_0 - X) \cdot w}{d} \right] \approx 2.7 \times 10^{-4} \cdot (X_0 - X). \quad (54)$$

Here $d = 2.562$ m is the distance between the sample and the detector, and $w = 0.21$ m/304 pix is the width of a single X-pixel. The variation along Y direction is simply due to the intensity

distribution along the height of the neutron beam. After integrating the intensity along Y direction, one can plot the reflectivity as a function of X and TOF, i.e. $R(X, \text{TOF})$, as shown in Fig. 16 (right). The specular line is again at $X = X_0$. Using equation (50), (53) and (54), the reflectivity $R(X, \text{TOF})$ can be transformed into $R(\theta_r, \lambda)$. Then, $R(\theta_r, \lambda)$ can be transformed into $R(Q_x, Q_z)$ by equation (51) and (52).

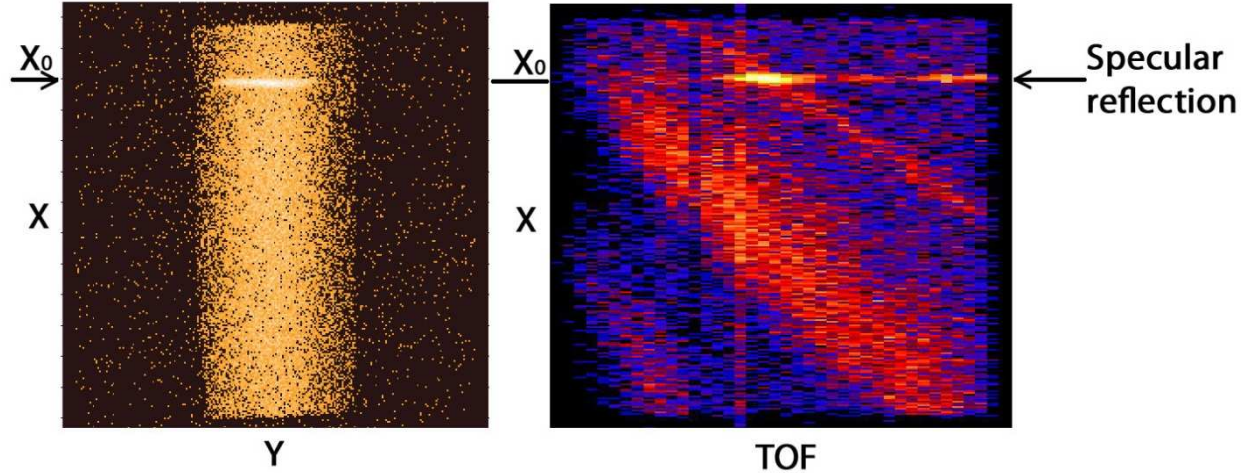


Figure 16. The 2-D raw data of the neutron reflectivity measured at the MR at a given incident angle. Left: neutron reflectivity versus the X and Y-pixel; Right: neutron reflectivity versus the X-pixel and the TOF.

3.4 Principles of neutron diffraction

Neutron diffraction is a powerful tool to study the modulated magnetic structures. In neutron diffraction, the neutrons can be scattered elastically or inelastically. A neutron can be inelastically scattered by the magnetic structures, with the creation of a magnon (spin wave) [48]. Only with the recent advance in the neutron sources, the spin wave dispersion relations of the magnetic superlattices could be measured by the inelastic neutron scattering [67, 68]. Large sample size is required in order to reduce the measurement time and the cost of the neutron beam. When a neutron is elastically scattered, it resembles the X-ray diffraction discussed in

Chapter 2. The elastic diffraction can be described by two distinct structure factors, the nuclear structure factor (F_n) and the magnetic structure factor (F_m) as the following [12]:

$$F_n(\mathbf{Q}) = \sum_j b_j e^{i\mathbf{Q} \cdot \mathbf{r}_j} e^{-W_j(\mathbf{Q}, T)}, \quad (55)$$

$$F_m(\mathbf{Q}) = \gamma r_0 \sum_j \mu_j f_j(\mathbf{Q}) e^{i\mathbf{Q} \cdot \mathbf{r}_j} e^{-W_j(\mathbf{Q}, T)} = \int \mathbf{M}(\mathbf{r}) e^{i\mathbf{Q} \cdot \mathbf{r}} d\mathbf{r}. \quad (56)$$

Here \mathbf{r}_j is the position of the atom j , μ_j is the magnetic moment of the j th atom, $\gamma = 1.9132$ is the gyromagnetic ratio, $r_0 = 2.8 \times 10^{-15}$ m is the classical radius of the electron, and $e^{-W_j(\mathbf{Q}, T)}$ is the Debye-Waller factor which arises from the thermal fluctuation of the position of an atom.

Neutrons do not have a form factor for the nuclear scattering but a nuclear scattering length (b_j) for the j th atom. On the other hand, the magnetic form factor is given by $f_j(\mathbf{Q})$. The magnetic structure factor can also be written as the Fourier transform of the magnetization density $\mathbf{M}(\mathbf{r})$ in a unit cell. Note that only the magnetization perpendicular to the scattering vector contributes to the magnetic scattering. In the case of neutron diffraction from a periodic magnetic modulation of either spin magnitude or spin orientation, the magnetic scattering appears in terms of the magnetic satellites around the nuclear scattering peaks.

3.5 Triple-axis neutron diffractometer

Triple-axis spectrometers have been widely used for both elastic and inelastic neutron scattering measurements to study the structures and dynamics in condensed matter. The schematic of a typical triple-axis spectrometer is shown in Fig. 17. The three rotational axes are the monochromator, the sample and the analyzer axes. Compared to the common double-axis spectrometer, e.g. the Philips X'pert X-ray diffractometer, the triple-axis spectrometer has an additional axis for the analyzer. Both the monochromator and the analyzer are typically single

crystals. By adjusting the angle of the monochromator, one can select the wavevector (\mathbf{k}_i) of the incident neutrons by Bragg diffraction. Similarly, a specific wavevector (\mathbf{k}_f) of the outgoing neutrons to be measured by the detector can be selected by adjusting the angle of the analyzer. The energy transfer ($\hbar\omega$) and the momentum transfer (\mathbf{Q}) can be written in terms of \mathbf{k}_i and \mathbf{k}_f , i.e.

$$\hbar\omega = E_i - E_f = \frac{\hbar^2}{2m_n} (k_i^2 - k_f^2), \quad (57)$$

$$\mathbf{Q} = \mathbf{k}_i - \mathbf{k}_f. \quad (58)$$

Therefore, the triple-axis spectrometer allows measurement of $S(\omega, \mathbf{Q})$ at any point in energy and momentum space physically accessible by the instrument. A triple-axis spectrometer can operate at the constant energy mode or the constant momentum transfer mode depending on type of excitation being examined.

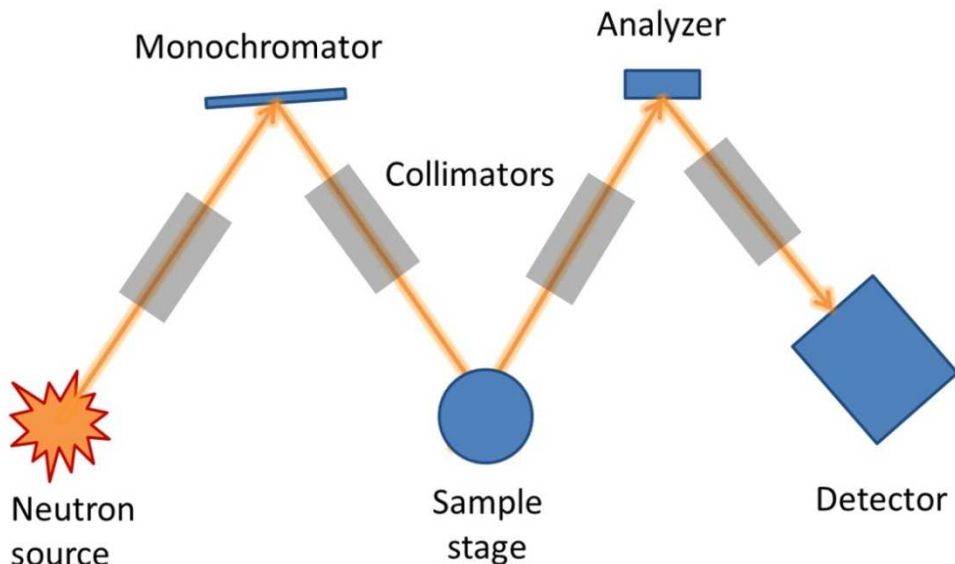


Figure 17. The schematic of a typical triple-axis spectrometer.

A detailed measurement of the dispersion relations by the inelastic neutron scattering requires single-crystal samples of very large size and high quality. Here we focus on the elastic

neutron diffraction ($\Delta E = 0$). At the Fixed-Incident-Energy Triple-Axis Spectrometer (FIE-TAX) located at the beam line HB-1A of the High Flux Isotope Reactor (HFIR), ORNL, the elastic neutron diffraction experiments were performed on a bulk Dy crystal and a Dy/Y superlattice, in order to explore the nature of the low-temperature magnetic phases and the evolution of the microscopic magnetic modulations in Dy. The bulk crystal weighs around 30 g and is enriched in the ^{163}Dy isotope. The Dy/Y superlattice been measured has over 200 total repeats. It is a stack of three superlattices of less repeats but high quality. This approach was used in order to avoid the poor epitaxial quality caused by the crystal defects accumulation during film deposition.

The FIE-TAX is a triple-axis spectrometer operating at a fixed incident energy of 14.6 meV by a double pyrolytic graphite (PG) monochromator system [69]. Two HOPG filters, one after each monochromator, are used to reduce $\lambda/2$ contamination. The high incident neutron flux is approximately $2 \times 10^7 \text{ cm}^{-2} \cdot \text{s}^{-1}$. The typical energy resolution at FIE-TAX is 0.5 meV to 1 meV depending on the analyzer being used. The FIE-TAX is capable of both elastic and inelastic neutron scattering measurement. For elastic study on the crystallographic and magnetic structures, the accessible scattering vector ranges from 0.2 \AA^{-1} to 4.9 \AA^{-1} .

4. MAGNETIC PHASE DIAGRAM OF BULK Dy

4.1 Overview of neutron diffraction results

A single-crystal ^{163}Dy with a mass of about 30 g was used for the neutron diffraction experiment. This isotope was selected because it has the lowest neutron absorption among the most abundant isotopes of Dy [70]. The measurements were performed at the Fixed-Incident-Energy (14.6 meV) Triple-Axis Spectrometer (FIE-TAX) located at the beam line HB-1A of the High Flux Isotope Reactor (HFIR), Oak Ridge National Laboratory (ORNL). The PG (002) analyzer used gives a typical energy resolution of 1 meV. Since the magnetic easy plane is the basal plane for the hexagonal Dy lattice, the complex magnetic structures tend to oscillate along the c-axis due to the competition of the interactions between the neighboring basal planes. Therefore, the scans were oriented such that the scattering vectors were parallel to the c-axis of the Dy crystal in order to probe the magnetic modulations propagating along the c-axis. The scans were performed as a function of temperature with three different fields (0 T, 1 T and 1.5 T) applied along the a-axis of the crystal, covering the paramagnetic, ferromagnetic, helical, fan phases and the possible intermediate phases in between (refer to Fig. 2). Table 4 lists the measurement conditions of the neutron diffraction experiment.

The raw data of the neutron diffraction scans at a fixed field can be plotted on a single three dimensional intensity map. Fig. 18 shows the results of the scans at the field of 1 T. The horizontal axis is the scattering vector Q around the Dy (0002) nuclear diffraction peak. The vertical axis is the temperature during the scan. In the measurement, the neutrons can be

Table 4. The list of the measurement conditions of the neutron diffraction experiments performed on the ^{163}Dy crystal.

Applied field	Temperature ranges	Heating/cooling	Covered phases
0	5 K - 260 K	heating and cooling	FM, HM, PM
1.0 T	119 K - 177 K	heating	FM, HM, Fan, PM
1.5 T	115 K - 190 K	heating	FM, Fan, PM

PM: paramagnetic state

HM: helical antiferromagnetic state

FM: ferromagnetic state

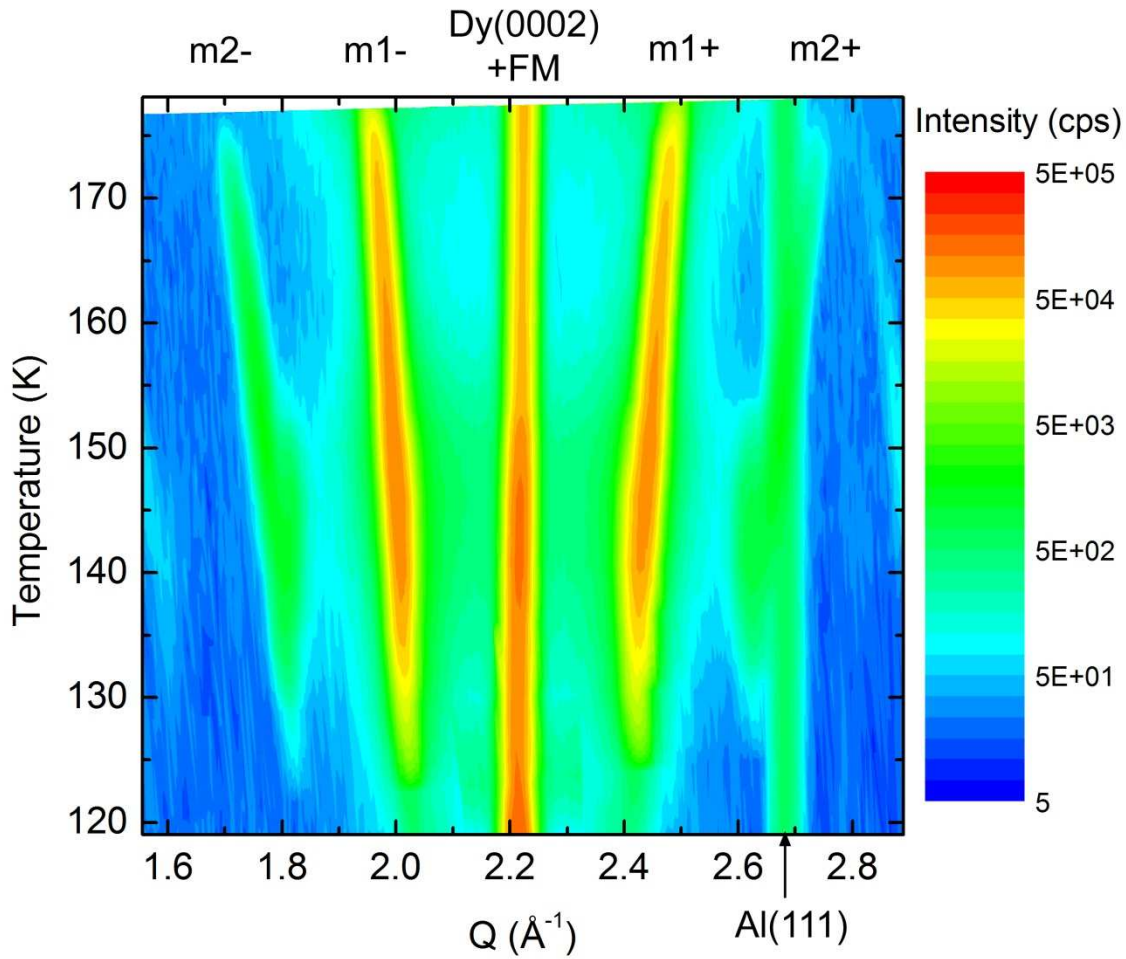


Figure 18. The raw data of the neutron diffraction scans along the c-axis of the ^{163}Dy crystal at various temperatures with the field of 1 T applied along the a-axis.

diffracted by both the nucleus and the magnetic moment of Dy, and also by the sample holder. Therefore, the intensities in Fig. 18 include the contributions from the nuclear, magnetic and background signals. One has to distinguish the signals of one origin from another before analyzing the data.

Each of the intensity sheets in Fig. 18 represents the evolution of the diffraction peak as a function of the temperature. Fig. 19 shows the diffraction pattern of a single Q-scan at a given temperature (170 K) and field (1 T). The Q-position of peak equals the magnitude of the reciprocal vector of the modulation giving rise to the peak. The temperature independent peak at around $Q = 2.7 \text{ \AA}^{-1}$ (Fig. 18) is from the Al sample holder used in the neutron diffractometer, since it matches the lattice spacing of the Al (111) planes. The central diffraction peak at around $Q = 2.2 \text{ \AA}^{-1}$ is associated with the modulation whose period equals the lattice spacing along the c-axis of the Dy crystal. This periodicity could stem from two possible scattering planes: a) the Dy nuclei in the (0002) atomic planes, and b) the magnetic moments of Dy in the (0002) atomic planes when they are all ferromagnetically (FM) aligned. The diffraction peak due to the former is temperature independent while the intensity from the latter is proportional to the square of the net magnetization of the sample. The position of the central diffraction peak varies slightly with temperature, reflecting the temperature dependence of the lattice parameter along the c-axis of the Dy crystal. The central peak in Fig. 18 can be seen shifting to a higher Q as temperature increases. The other peaks, spreading evenly and symmetrically about the central peak, are the satellites of pure magnetic origin. A pair of first-order magnetic satellites (marked as m1+ and m1-) and two second-order satellites (m2+ and m2-) can be seen in Fig. 19. The positions of the magnetic satellite peaks are temperature dependent for the case of Dy, and can be related to the average period (Λ_m) of the magnetic modulation in the crystal by equation (27),

$$\Delta Q = \frac{2\pi n}{A_m}, \quad (27)$$

where n is the order of the magnetic satellite and ΔQ is the separation between the nuclear diffraction peak and the n th-order magnetic satellite.

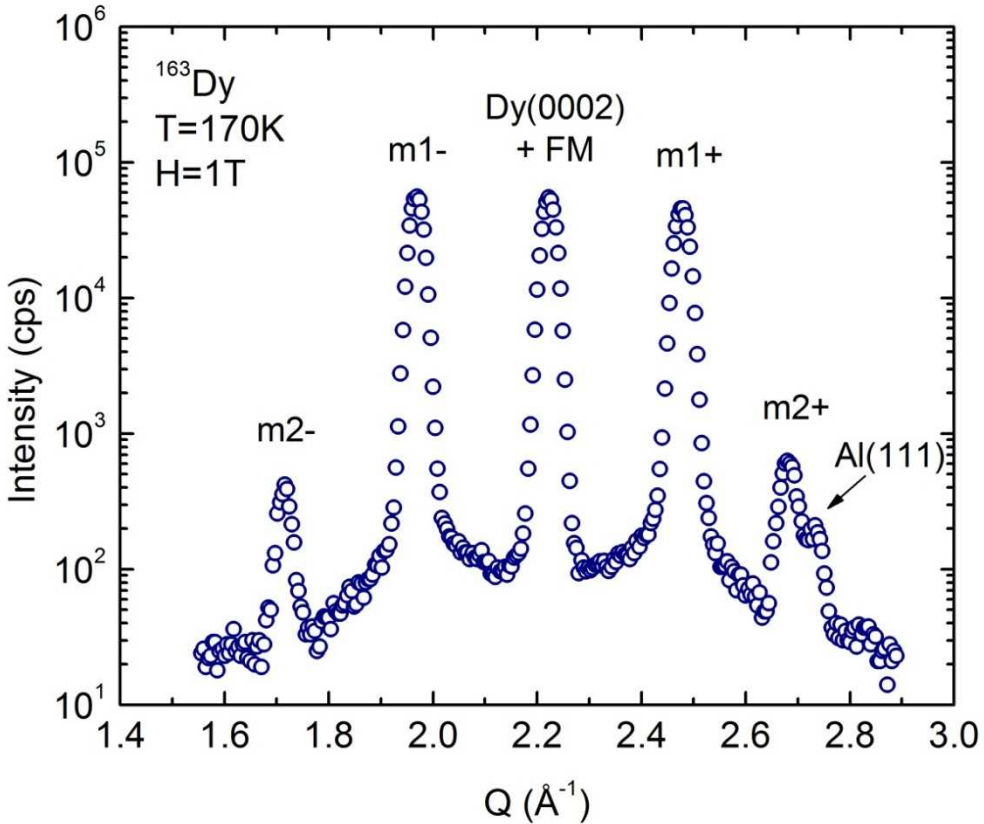


Figure 19. The raw data of a single neutron diffraction scan along the c-axis of the ^{163}Dy crystal at a fixed temperature (170 K) with the field of 1 T applied along the a-axis.

The diffraction peaks observed at the paramagnetic state of Dy are of pure nuclear origin. In Fig. 20, at the temperature of 275 K, well above the Neel temperature (179 K) of Dy, only the Dy (0002) and Al (111) nuclear peaks show up. The nuclear diffraction peaks are nearly perfect Gaussians with insignificant diffuse scattering. The most important information delivered by the nuclear diffraction peaks is the modulation of the chemical periodicity, i.e. the interplanar

spacing, along the c-axis of the hexagonal crystal, corresponding to the position of the Dy (0002) peak. The temperature dependence of the interplanar spacing is discussed in section 4.2.

Since the integrated intensity of the nuclear diffraction peak is temperature independent, it is reasonable to subtract the diffraction pattern in Fig. 20 from any diffraction patterns of lower temperatures to obtain the pure magnetic signal. However, the subtraction cannot be done directly because the central diffraction peaks are not aligned at the same Q position, owing to the temperature dependence of the lattice spacing of the Dy (0002) planes. The position of the central diffraction peak $Q_0(T)$ can be written as a function of the temperature:

$$Q_0(T) = \frac{2\pi}{c(T)/2}, \quad (59)$$

where $c(T)$ is the lattice parameter along the c-axis of the Dy crystal. This issue can be solved by converting the horizontal axis to the reduced wavevector [000L], where L is the ratio between the scattering vector and the reciprocal vector of the c-axis:

$$L = \frac{Q \cdot c}{2\pi}. \quad (60)$$

Therefore, the position of the central diffraction peak in terms of the reduced wavevector becomes temperature independent, i.e.

$$L_0 = \frac{Q_0 \cdot c}{2\pi} = 2. \quad (61)$$

A constant background intensity was also subtracted from the raw signal in order to retrieve the clean magnetic signal.

It is worth mentioning that during the heating and cooling process, the expansion or contraction of the sample holder may misalign the c-axis of the crystal from the scattering vector, giving lower intensities of the diffraction peaks. Therefore, the crystal was realigned at each temperature before the scan. However, for some of the temperature points, the crystal showed

further movement after the realignment. The intensity of the diffraction peaks for these temperature points were corrected manually.

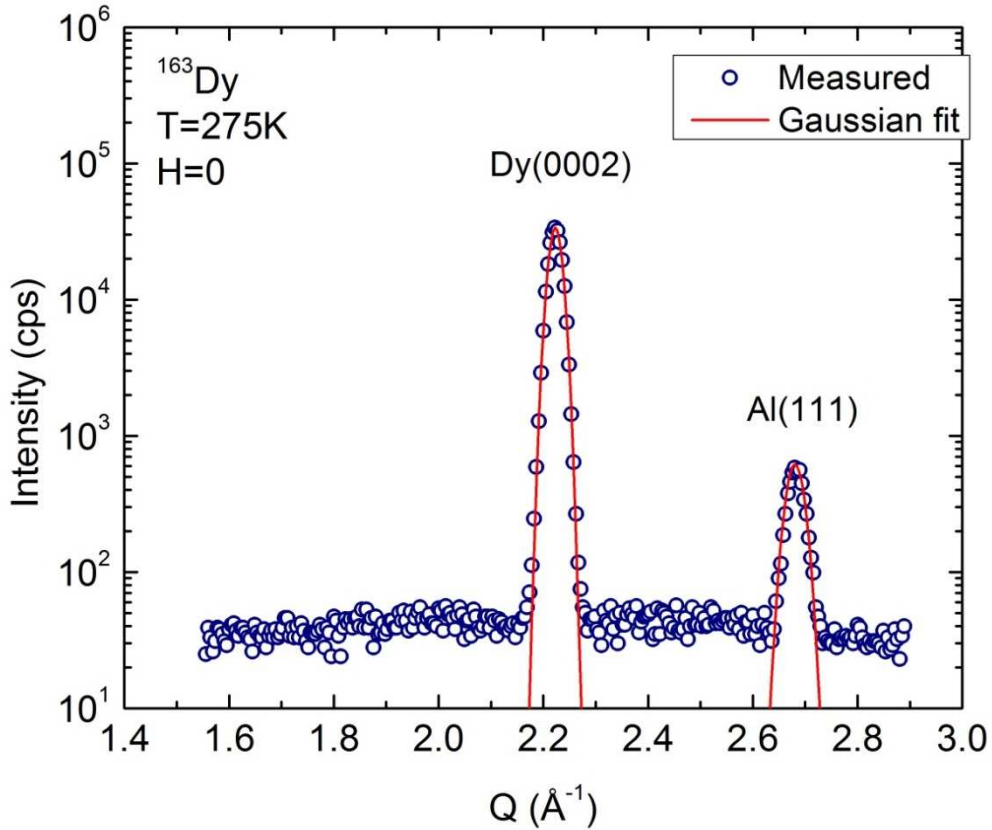


Figure 20. The neutron diffraction pattern of pure nuclear origin measured at 275 K with no field applied.

After the subtraction of the nuclear signal, the pattern of the pure magnetic diffraction is plotted in Fig. 21. The central diffraction peak at $L = 2.0$ stems from the ferromagnetic (FM) component in the crystal, whereas the magnetic satellites are the result of the magnetic modulation along the c-axis. The magnetic peaks could be nicely fitted by a Gaussian function. The width of the Gaussian function is approximately the same for all diffraction peaks, as it is defined by the instrument resolution ($\Delta L \approx 0.02 - 0.03$). In addition, noticeable diffuse scattering

was observed around the FM diffraction peak and the first-order satellite peaks, indicating the magnetic inhomogeneity in the crystal. The detailed discussions of magnetic diffraction patterns at various temperatures and fields are given in section 4.3 through 4.5.

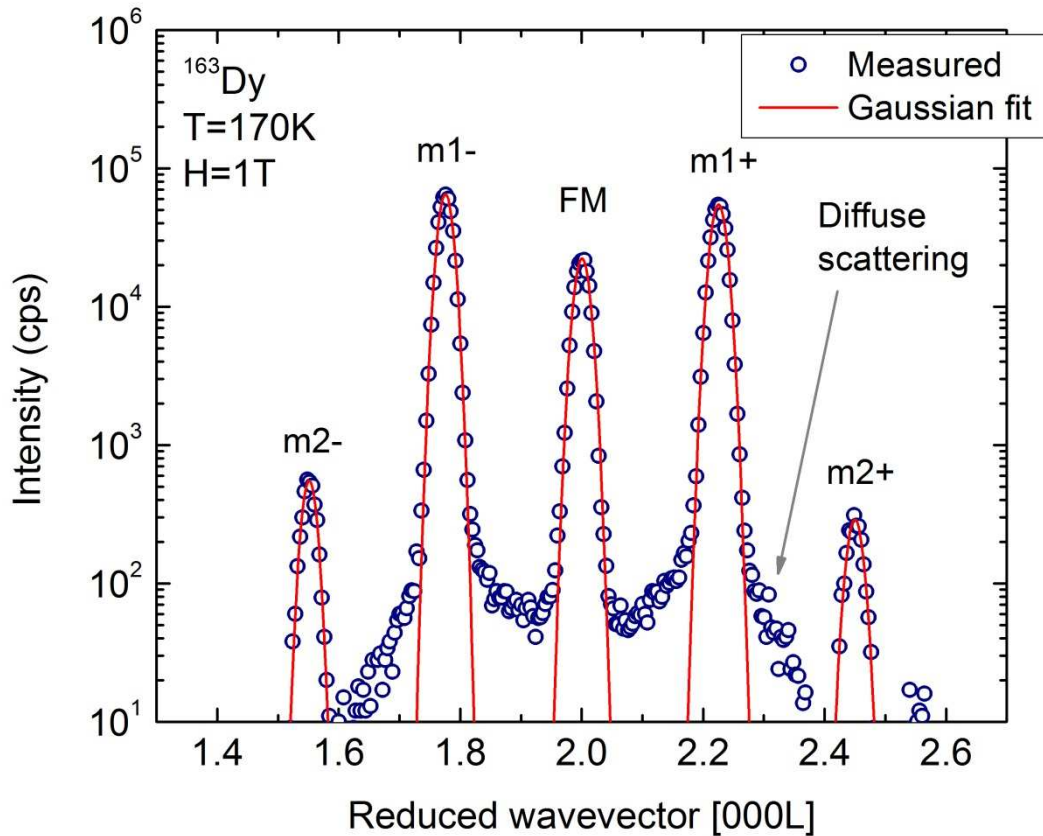


Figure 21. The neutron diffraction pattern of pure magnetic origin obtained by subtracting the nuclear contributions (Fig. 20) from the raw data (Fig. 19). The horizontal axis has been converted to the reduced wavevector [000L], in order to align the FM peaks.

4.2 Temperature dependence of the lattice parameters of ^{163}Dy in various applied fields

The interplanar spacing along the c-axis of the Dy crystal is plotted as a function of temperature in Fig. 22 for different applied fields (0, 1 T and 1.5 T). When no field applied, the lattice spacing was measured for both heating and cooling, and no significant thermal hysteresis

was observed. The curve is evidently separated into three stages by two temperature points, the Curie temperature (89 K) and the Neel temperature (179 K). Above 179 K, the c-axis of the Dy crystal expands as the temperature increases. In contrast, the c-axis contracts as the temperature increases from 89 K to 179 K. At 89 K, where the first-order helix-ferromagnetism transition occurs, there is an abrupt expansion of the c-axis. The same behavior has been measured by Darnell [23] and suggested by Evenson et al. [8] as the primary contribution, in terms of the magnetostrictive interactions, for the helix-ferromagnetism phase transition and the temperature dependence of the pitch of the helix.

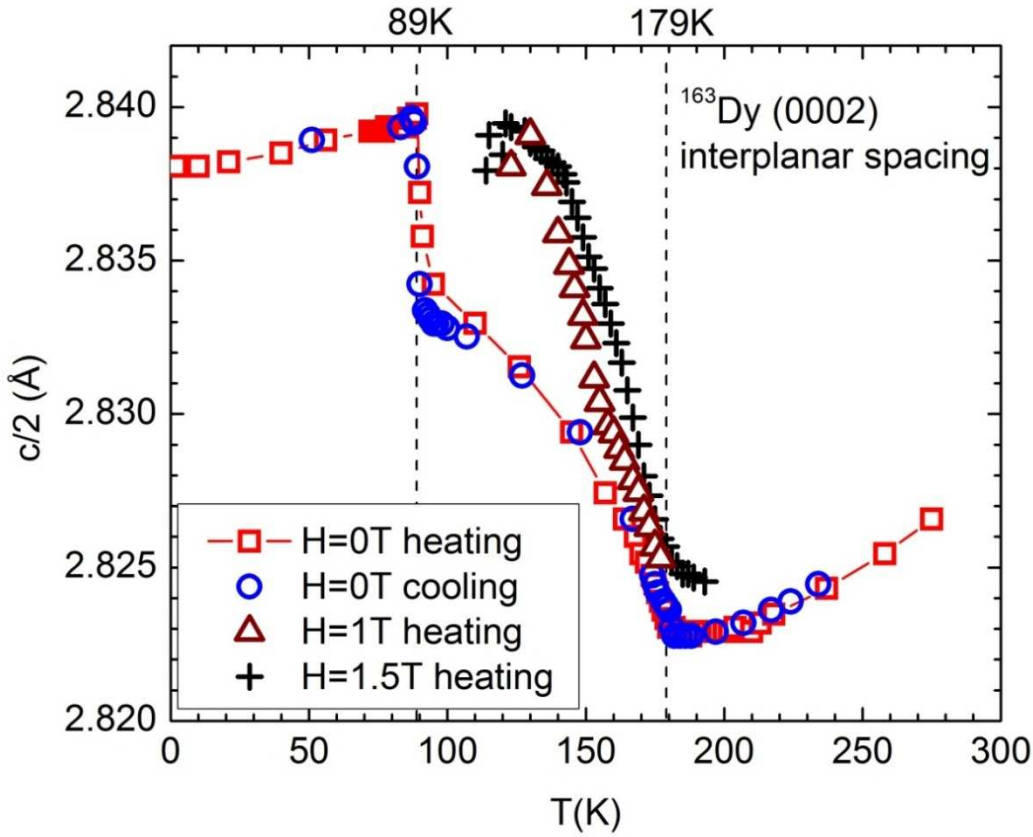


Figure 22. The temperature dependence of the interplanar spacing along the c-axis of the Dy crystal in different fields (0, 1 T and 1.5 T) applied along the a-axis. The dash lines indicate the Curie temperature (89 K) and the Neel temperature (179 K).

The lattice parameters in a non-zero field (1 T and 1.5 T) were only measured between 110 K and 190 K. The field applied along the a-axis induces a further expansion of the c-axis from the zero field values, as shown in Fig. 22. At around 130 K, the c-axis spacing has reached 2.838 Å, the value associated with ferromagnetism in zero field. Given that a higher helix-ferromagnetism transition temperature has been reported with non-zero field applied [2, 17], it is evident that the c-axis (structural) transition is coupled with the helix-ferromagnetism (magnetic) transition.

4.3 Magnetic phases and the phase transitions of ^{163}Dy in zero field

The magnetic scattering patterns in zero field covered the ferromagnetic diffraction peak (FM) and a pair of first-order magnetic satellites (m_1^- and m_1^+). The results were analyzed in terms of the temperature dependence of the integrated intensity (Fig. 23 top) and the position of the diffraction peaks (Fig. 23 bottom). There was no significant thermal hysteresis loop for the heating and cooling processes, so the data is shown for the heating only. The integrated intensity of the FM peak indicates the amount of the ferromagnetic alignment in the sample, while the intensity of the magnetic satellite peak reflects the degree of ordering of the magnetic modulation. The high intensity of the FM peak with the absence of the magnetic satellites confirms the ferromagnetic phase for temperatures below 89 K. Above 89 K, the FM peak immediately drops to a very low value, while large magnetic satellites appear, suggesting a dominating magnetic modulation with net magnetization close to zero. This magnetic modulation is known as the helical antiferromagnetic structure, which is the ground state of the magnetic hcp lattice if only the RKKY interaction is considered [71]. Above 179 K, all the intensities drop to zero quickly as

it enters the paramagnetic region. The first-order ferromagnetism-helix transition at 89 K and the second-order helix-paramagnetism transition at 179 K are also evident from Fig. 23. Moreover, the integrated intensity of the diffuse scattering shows a peak at 89 K and 179 K respectively, further confirming the two phase boundaries. The peak positions shown in Fig. 23 (bottom) provide information about the period of the magnetic modulation in the crystal. The FM peak is coincident with the (0002) nuclear peak since it has the same modulation as the Dy (0002) atomic planes. The period of the helical modulation can be calculated by equation (27). The propagation vector \mathbf{k} and the average turn angle of the helix φ are then given by:

$$\mathbf{k} = \frac{2\pi}{\Lambda_m} \hat{\mathbf{c}}, \quad (62)$$

$$\varphi = \frac{c \cdot 180^\circ}{\Lambda_m}. \quad (63)$$

Fig. 24 shows the temperature dependence of the propagation wavevector and the average turn angle of the helix for both heating and cooling. The turn angle decreases nearly linearly as the decrease of the temperature. At a given temperature between 110 K and 170 K, the turn angles during heating are around 1° larger than those in cooling. As other measurements [2, 14, 17] on the magnetic phases of the bulk Dy under zero magnetic field suggested, no intermediate phase was detected here.

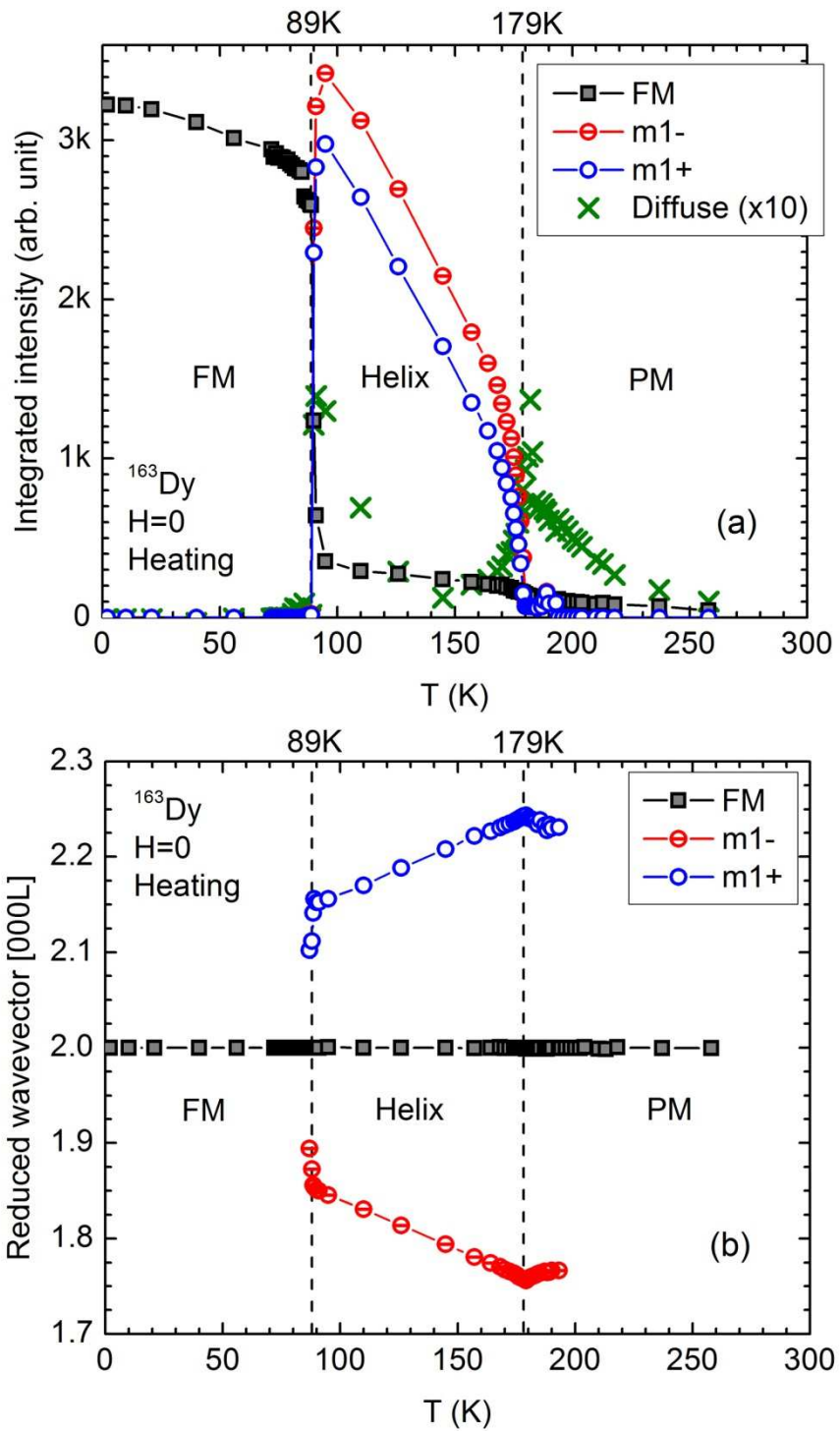


Figure 23. The temperature dependence of the integrated intensity (top) of the magnetic diffraction peaks and the diffuse scattering, and the position (bottom) of the peaks with no field applied. The dash lines indicate the phase boundaries between the FM, helix, and PM phases.

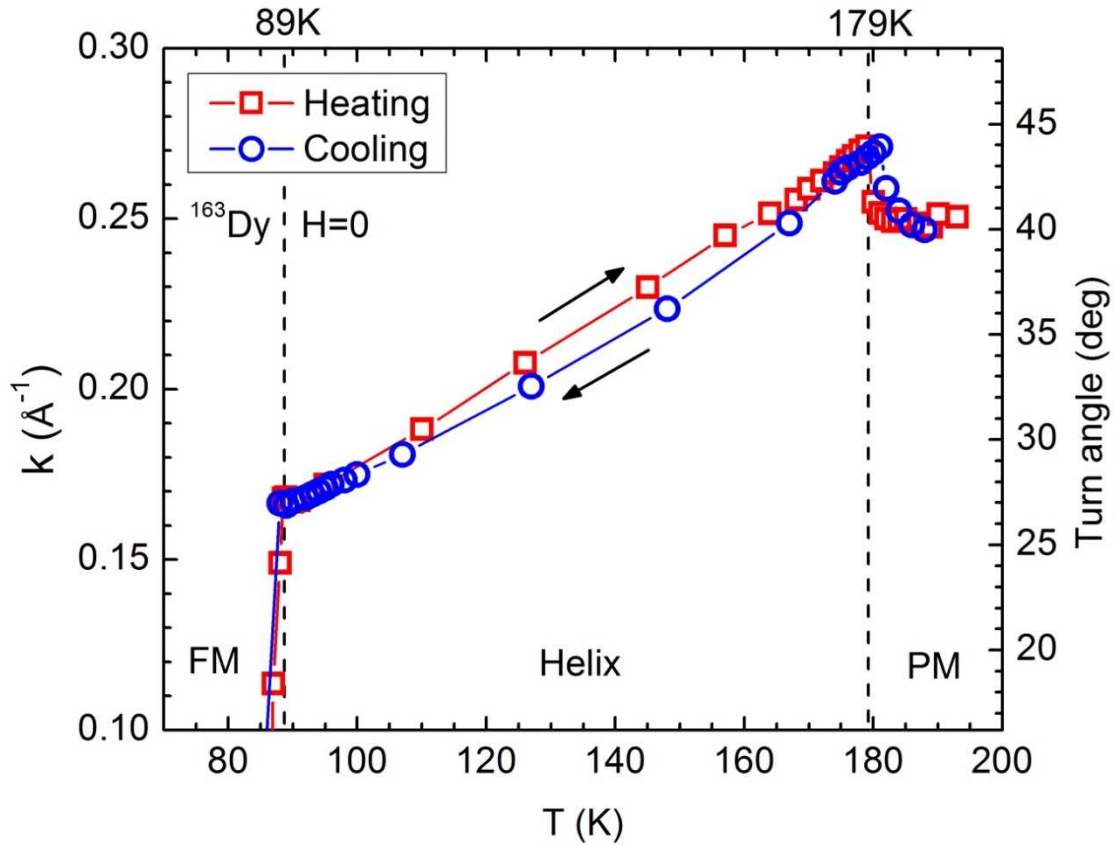


Figure 24. The temperature dependence of the propagation wavevector and the average turn angle of the helix modulation in zero field.

4.4 Magnetic phases and the phase transitions of ^{163}Dy in the field of 1 T

The magnetic field applied in the basal plane of the hexagonal Dy crystal is known to not only change the transition temperature between the helical and the ferromagnetic phases, but also induce intermediate phases [1]. An intermediate fan phase was predicted to emerge naturally between the helical phase and the ferromagnetic phase in theoretical investigations [72, 73] and was later confirmed with experiments [14-16]. However, more intermediate phases are possible based on the magnetic phase boundaries (Fig. 2) constructed by Chernyshov et al. via a careful study of the magnetocaloric effect, magnetization, AC susceptibility and heat capacity on single-

crystal Dy [17]. Here we examine the nature of the field induced magnetic phases and the transitions as a function of temperature by neutron diffraction along the c-axis of the Dy crystal.

With the field of 1 T applied along the a-axis of the Dy crystal, neutron diffraction scans were performed along the c-axis at various temperatures from 119 K to 177 K. According to the phase diagram (Fig. 2) in reference [17], the ferromagnetic phase, a possible new phase, the fan phase, the helical antiferromagnetic phase and a possible vortex phase were covered. Similar to the zero-field case, the temperature dependence of the integrated intensity (top) and the position (bottom) of the magnetic diffraction peaks are plotted in Fig. 25. Below 119 K, only the ferromagnetic phase is present since only a large ferromagnetic diffraction peak was observed. Between 119 K and 145 K, the intensity of the ferromagnetic peak decreases whereas the intensities of the magnetic satellites increase. In other words, the net magnetization of the crystal is reduced as the modulated magnetic ordering accumulates. The presence of both intense ferromagnetic peak and satellite peaks is the character of the fan phase. The magnetic satellites grow slower upon heating from 119 K to 130 K, but faster from 130 K to 145 K (Fig. 25 top). The fan phase below 130 K appears to be only short-range ordered (SRO), while it becomes long-range ordered (LRO) above 130 K. The onset (130 K) of the LRO fan phase is consistent with the structural transition of the c-axis (see Fig. 22). Between 153 K and 177 K, the ferromagnetic peak drops to a very low value while the magnetic satellites remain relatively intense, suggesting a dominating helical antiferromagnetic state. In our scan geometry, the magnetization parallel to the c-axis does not contribute to the magnetic scattering. Therefore, we are not able to distinguish the helix phase from the vortex phase where the magnetic moments tip out of the basal plane.

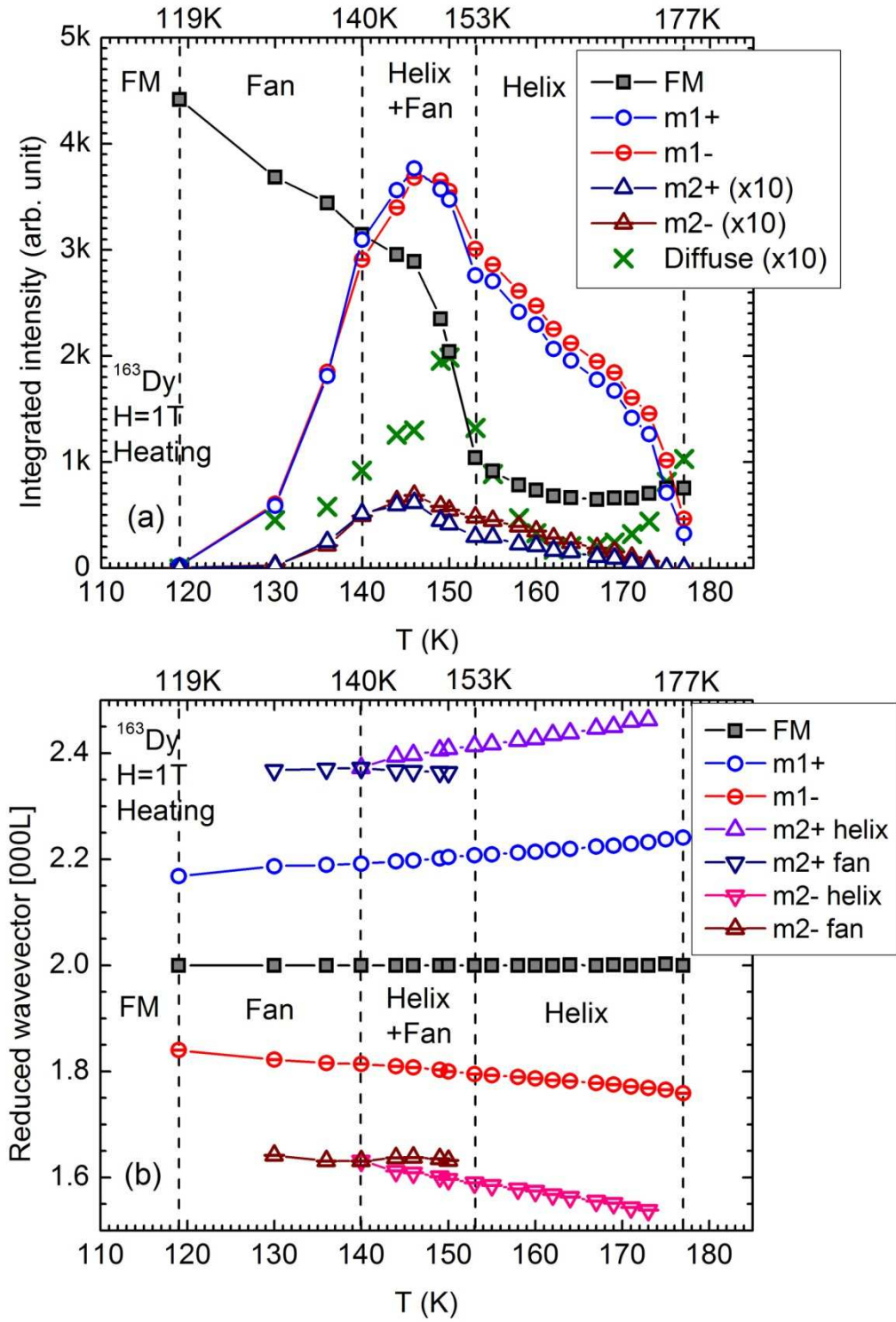


Figure 25. The temperature dependence of the integrated intensity (top) of the magnetic diffraction peaks and the diffuse scattering, and the position (bottom) of the peaks with 1 T field applied along the a -axis of the Dy crystal. The dash lines indicate the phase boundaries between the FM, fan, coexisting helix and fan, helix, and PM phases.

Between 140 K and 153 K, the second-order magnetic satellite peaks split into a double-peak and the first-order magnetic satellites also appear broader (see Fig. 18 and Fig. 25 bottom). The separation between the double peaks of the second order ranges from 0.026 to 0.032 in terms of the reduced wavevector, which is barely above the resolution limit ($\Delta L \approx 0.02 - 0.03$) of the instrument at the scan region. Therefore, the resolution is not sufficient to distinguish the double peaks of the first order, which would be much closer. The split of the magnetic satellites suggests the coexistence of two magnetic modulations of different periods. This behavior was initially discovered by neutron diffraction at 149 K with the applied field between 0.9 T and 1.2 T along the a-axis of the Dy crystal [15]. Reference [15] investigated the origin of the two modulations and concluded that the magnetic satellites closer to the central peak are associated to the fan phase and the others are due to the helix phase. Therefore, we found the helix and the fan phase coexist between 140 K and 153 K in the field of 1 T. A closer look of the double peaks at the second-order magnetic satellite (m2-) is shown in Fig. 26. The peak at the smaller L arises from the helix while the one at the larger L stems from the fan structure. Both peaks can be fitted accurately by a Voigt function with the width consistent with the instrument resolution. The peak positions of the double peaks in Fig. 25 (bottom) are determined by the fitting. The peak intensity showed in Fig. 25 (top) is the total intensity of both peaks. Two tendencies of the double m2- peaks are observed in Fig. 26 as the temperature increases. First, the helix peak grows and the fan peak decays continuously upon heating. This illustrates that the phase transition from the fan phase below 140 K to the helix phase above 153 K is of the first-order, but is broadened by the inhomogeneity in the crystal. Second, while both of the peaks shift closer to the central peak as temperature increases, the helix peak is shifting at a higher rate than the fan peak does. The propagation wavevectors (k) for both of the helix and the fan modulations are

calculated based on their peak positions and plotted in Fig. 27. Instead of the turn angles, the average period (Λ_m) of the magnetic modulation corresponding to the propagation wavevector is shown as the vertical axis on the right side of Fig. 27, because the average turn angle of the fan modulation cannot be determined without knowing its opening angle.

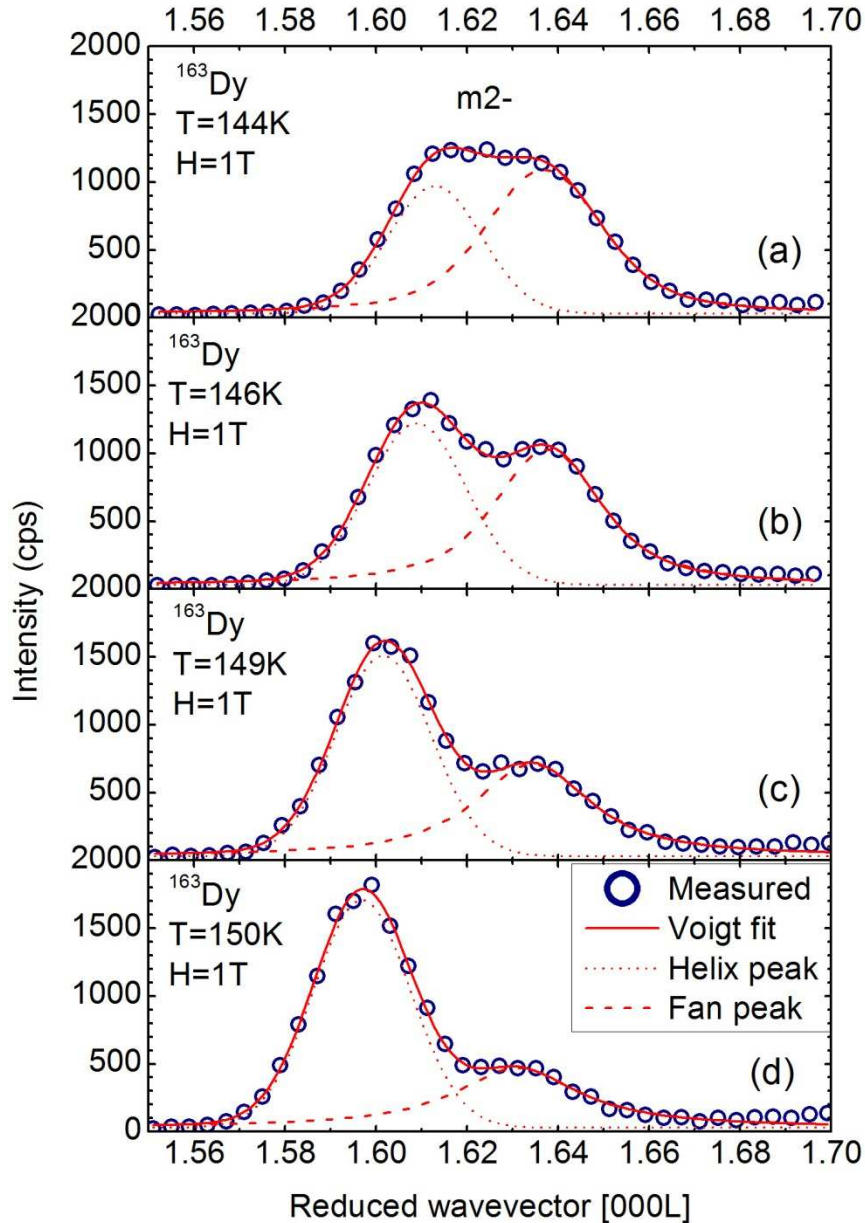


Figure 26. The temperature dependence of the double peaks at the $m2-$ magnetic satellite in a field of 1 T applied along the a-axis of the crystal. The peak at the lower L is due to the helix structure and the one at higher L stems from the fan modulation.

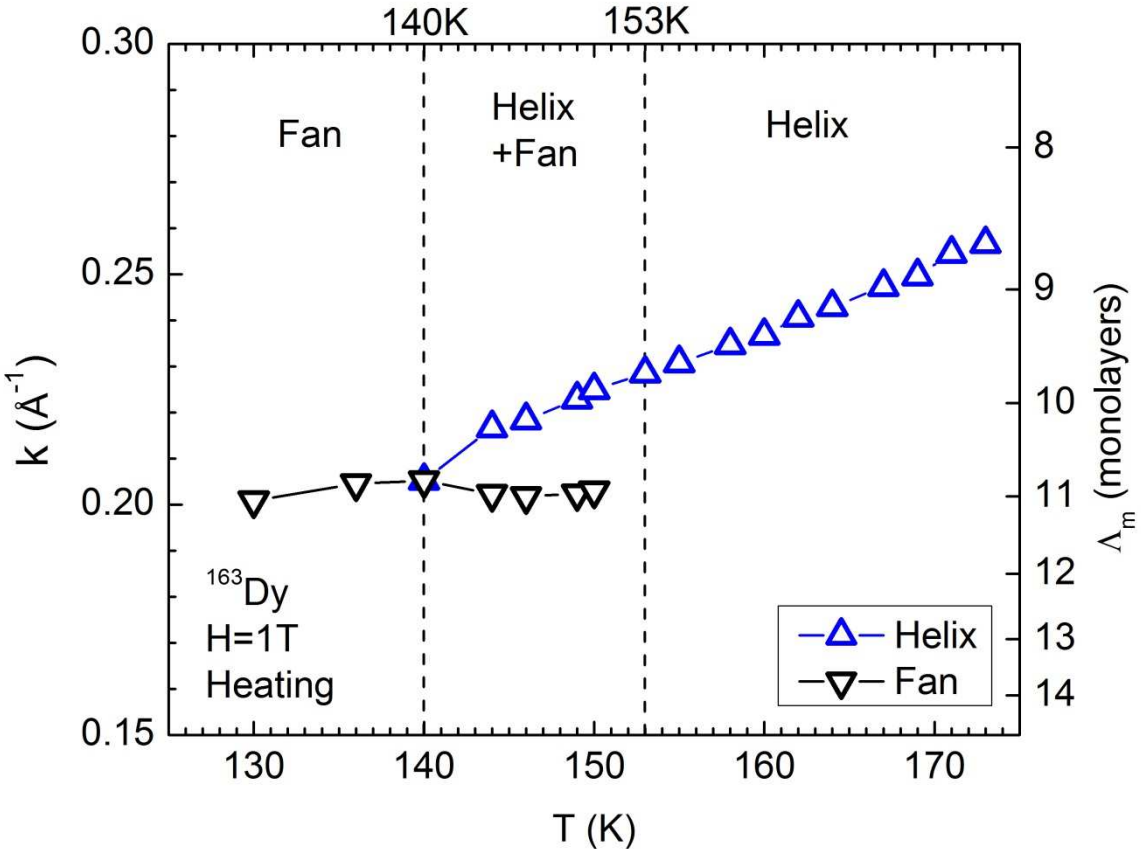


Figure 27. The temperature dependence of the propagation wavevector and the average period of the helix and fan modulations in 1 T field applied along the a-axis of the Dy crystal.

In the field of 1 T, the fan phase exists between 130 K and 153 K, and the average period of the fan modulation stays at around 11 monolayers of the Dy (0002) plane (see Fig. 27). On the other hand, the helix phase appears from about 140 K through 177 K, and its average period decreases from 11 to 9 monolayers as the increase of the temperature. The average turn angles of the helix modulation can be calculated by equation (27). However, the fan modulation cannot be described by the turn angle alone. It is necessary to introduce the opening angle for the fan

structure. The average turn angle (φ) and the opening angle (Φ) are related by:

$$2\Phi = \Lambda_m \varphi. \quad (64)$$

Here Λ_m is the average period of the magnetic fan modulation in terms of the number of monolayers.

The average turn angle and the opening angle of the fan modulation were estimated based on the net magnetization of the structure measured at 1 T from reference [17]. Assuming that the turn angle is uniform throughout the fan modulation, the orientation of the magnetization in each monolayer can be uniquely determined such that the net magnetization perpendicular to the applied field is zero. Fig. 28 interprets the evolution of the fan modulation (a-c) and the helix modulation (d-f) with the estimated values for the turn angle and opening angle. Only one period of the magnetic modulation is shown in Fig. 28. The numbers at the end of the arrows indicate the index of the Dy (0002) atomic layers. Although the period of the fan modulation remains at 11 monolayers from 130 K to 153 K, the average turn angle and the average opening angle increases continuously with temperature. This agrees with the decrease of the ferromagnetic diffraction peak in Fig. 25 (top). On the other hand, the turn angle of the helix modulation increases with temperature, resulting in the decrease of the period of the helix structure. Note that in reality, the turn angles in the helix and fan modulations are unlikely to be uniform under the influence of the external field. The schematics in Fig. 28 only give an averaged picture on the evolution of the magnetic modulations.

Based on Fig. 25 and Fig. 28, the evolution of the magnetic phases during heating in the field of 1 T can be described as the following:

- (1) Between 119 K and 130 K, the magnetizations in different Dy basal planes start to spread about the field direction due to interplay between the RKKY interaction and

the external field, and form a SRO fan-like structure. The transition is of the second-order. The modulation of the fan structure is not well-defined initially due to the inhomogeneity in the crystal.

- (2) At \sim 130 K, the lattice spacing between the (0002) planes is reduced abruptly (see Fig. 22), thus significantly modifies the magnetoelastic energy. The ferromagnetic arrangement is no longer stable.
- (3) As the temperature increase from 130 K to 140 K, the LRO fan develops. The moments in the fan structure continuously spread to a wider opening angle while the period of the fan remains at 11 monolayers.
- (4) At \sim 140 K, a small fraction of the fan structure goes through a first-order transition to the helix structure. The turn angle is not modified during the transition but the chirality of the magnetization is reversed for half of the monolayers.
- (5) Heating from 140 K to 153 K, more fan structure transforms into the helix structure. The turn angles for the helix and the remaining fan modulations grow continuously but at different rates.
- (6) At \sim 153 K, the transition to the helix is complete, when the period of the helix modulation is 10 monolayers.
- (7) From 153 K to 177 K, the period of the helix modulation further reduces to 9 monolayers.
- (8) At \sim 177 K, the helix phase undergoes a second-order transition to the paramagnetic phase.

The intensity peaks of the diffuse scattering again confirm the critical temperatures of fan-helix and helix-paramagnetic transitions (Fig. 25 top). However, there is not enough evidence to verify the new phase at ~ 130 K suggested in Fig. 2.

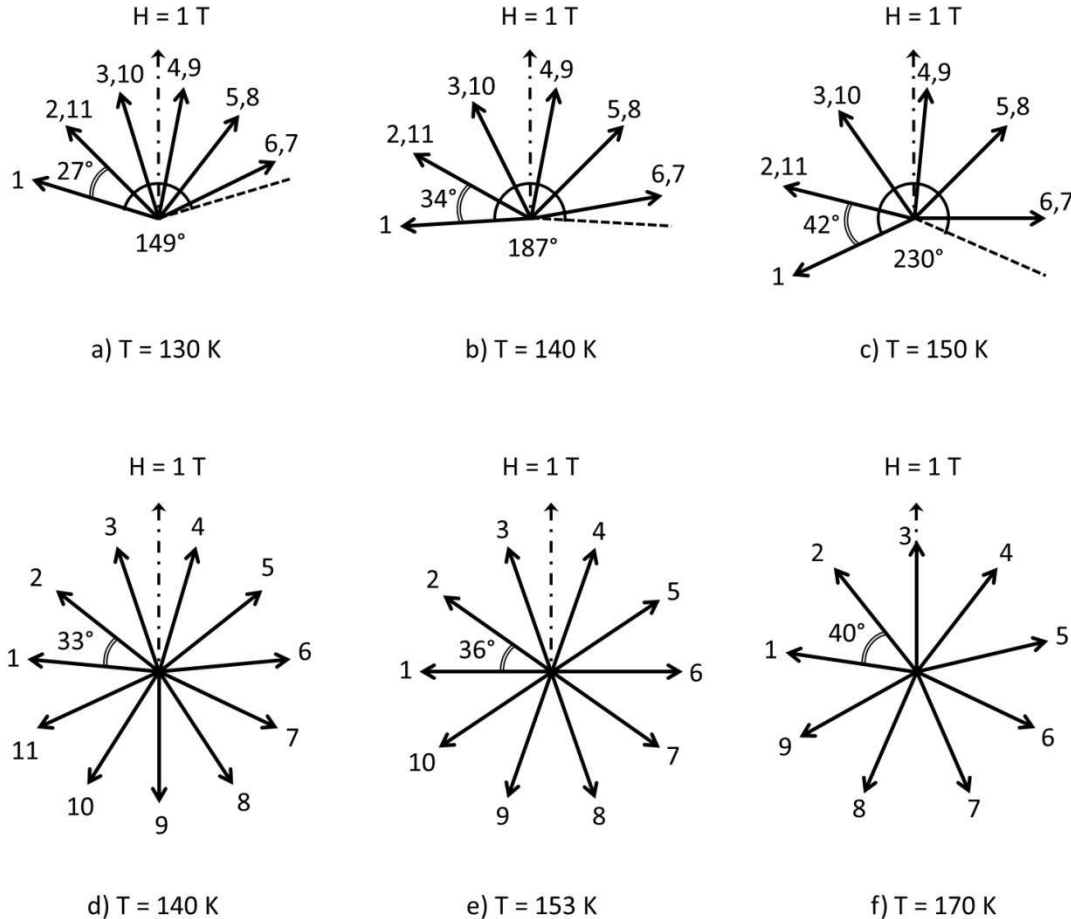


Figure 28. The evolution of the fan modulation (a-c) and the helix modulation (d-f) as temperature increases in the field of 1 T. Only one period of the magnetic modulation is shown. The average turn angle and opening angle are estimated based on the magnetization in reference [17]. The numbers at the end of the arrows indicate the indices of the Dy (0002) atomic layers.

4.5 Magnetic phases and the phase transitions of ^{163}Dy in the field of 1.5 T

With the field of 1.5 T applied along the a-axis of the Dy crystal, the neutron diffraction scans were performed along the c-axis from 114 K to 190 K. The ferromagnetic phase, a possible

new phase, the fan phase, a possible helifan phase and the paramagnetic phase were covered in this measurement according to the phase diagram (Fig. 2) in reference [17]. Again, the integrated intensity (top) and the position (bottom) of the magnetic diffraction peaks are plotted in Fig. 29. At 114 K, the ferromagnetic phase dominates, while the fan phase emerges identified by presence of magnetic satellites (see Fig. 30a). Upon heating, the fan phase grows as evidenced by the increasing magnetic satellites (Fig. 30b). The fan phase is most pronounced at ~155 K (Fig. 30c). Above 177 K, the magnetic modulation turns into the paramagnetic phase, with only small ferromagnetic component induced by the external field (Fig. 30d). However, the magnetic satellites do not immediately vanish at 177 K, suggesting some SRO fan structure still persists up to 190 K. The intensity of the ferromagnetic peak decreases constantly as the temperature increases from 114 K to 177 K. The propagation wavevector of the fan modulation and its corresponding period in terms of the number of monolayers are plotted in Fig. 31. A closer look at the fan region in Fig. 29 and Fig. 31 suggests that the evolution of the fan phase can be divided into three stages:

- a. Between 114 K and 142 K, the magnetic satellites are relatively weak and grow slowly compared to stage b. The period of the magnetic modulation decreases continuously from around 12 to 10 monolayers.
- b. From 142 K to 160 K, the magnetic satellites grow at a higher rate compared to stage a. The period of the magnetic modulation stays at around 10 monolayers.
- c. From 160 K to 177 K, the magnetic satellites descend. The period of the magnetic modulation decreases continuously from around 10 to 8 monolayers.

The temperature ranges of the three stages match closely to the regions of the possible new phase, the fan phase, and the possible helifan phase indicated in Fig. 2.

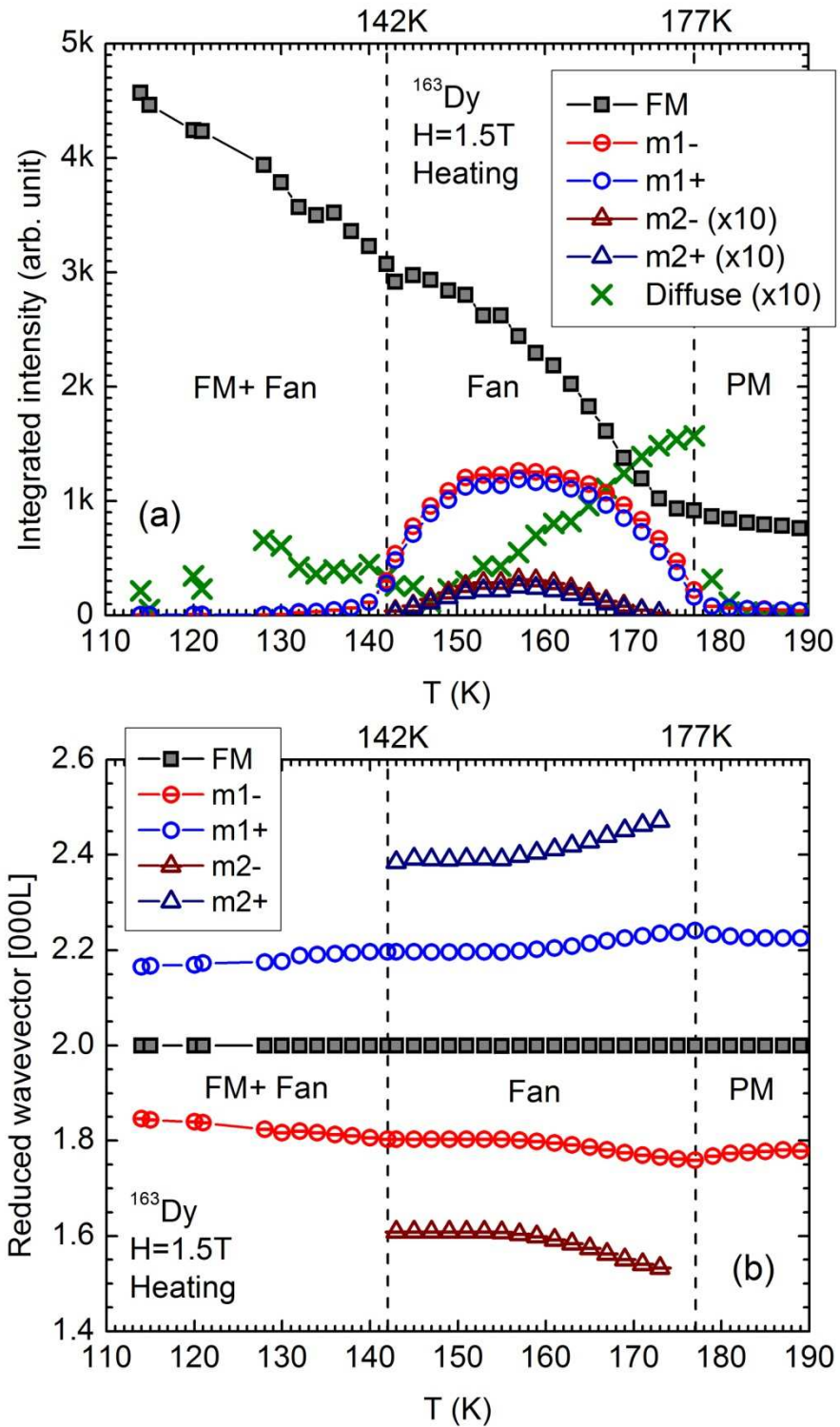


Figure 29. The temperature dependence of the integrated intensity (top) of the magnetic diffraction peaks and the diffuse scattering, and the position (bottom) of the peaks with 1.5T field applied along the a-axis of the Dy crystal. The dash lines indicate the phase boundaries between the FM, fan, and PM phases.

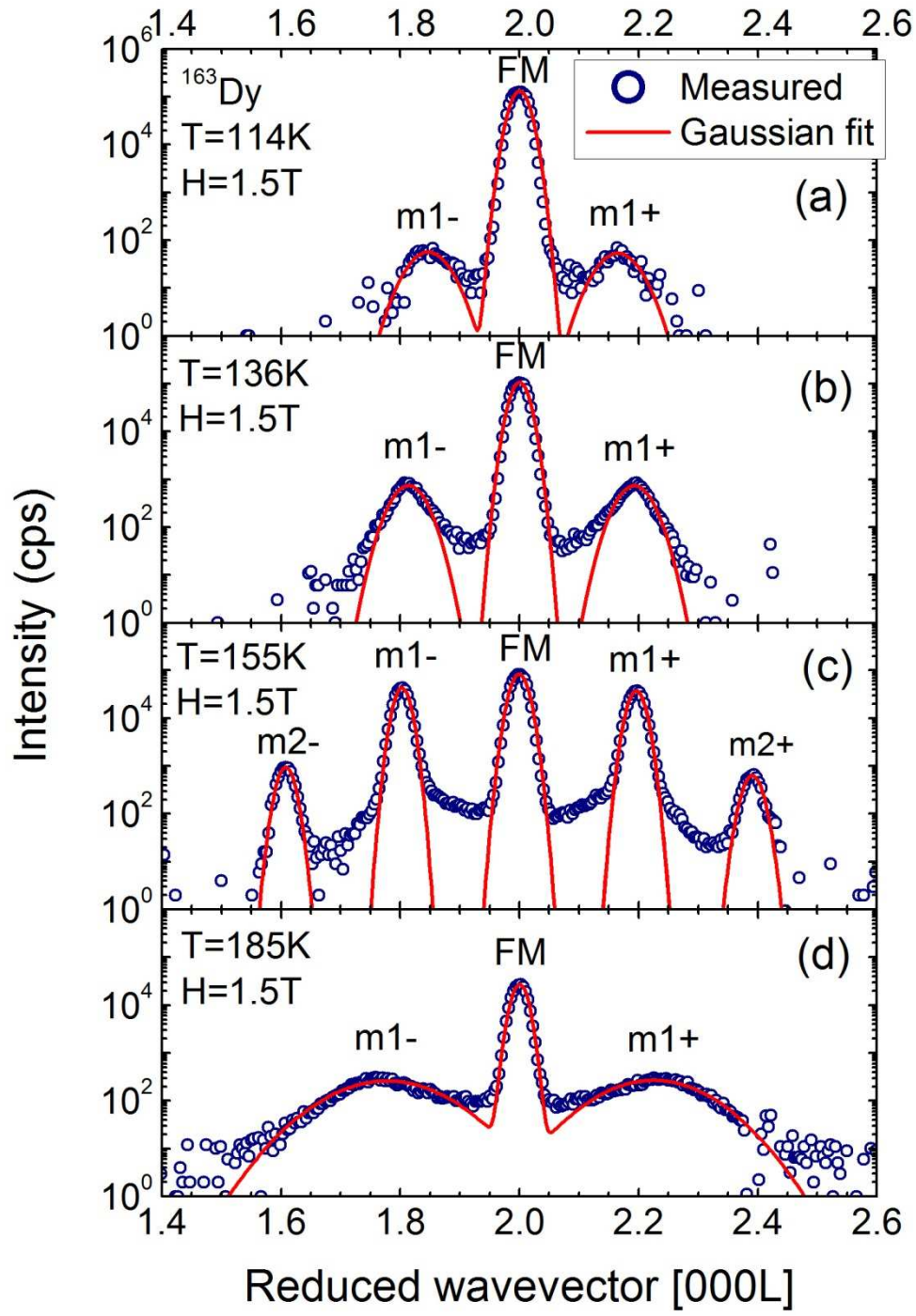


Figure 30. The magnetic diffraction patterns measured at (a) 114 K, (b) 136 K, (c) 155 K, and (d) 185 K when 1.5 T field is applied along the a-axis of the Dy crystal.

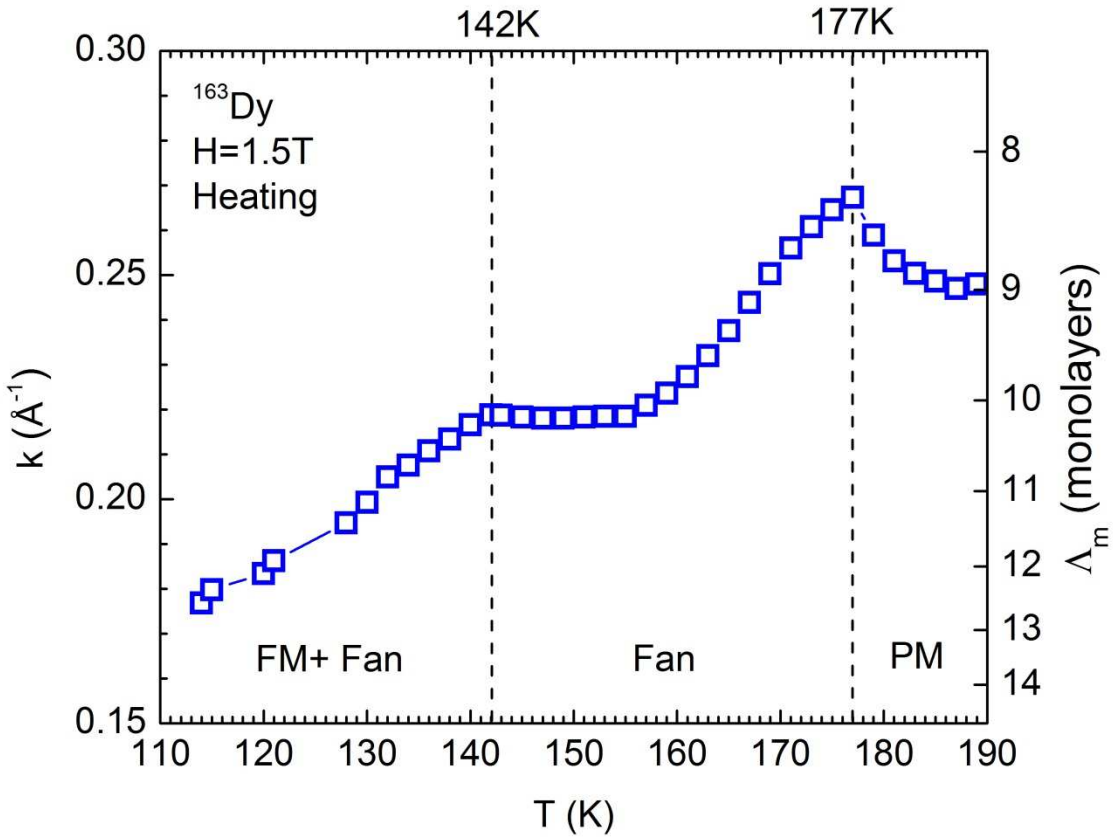


Figure 31. The temperature dependence of the propagation wavevector and the average period of the fan modulations in 1.5 T field applied along the a-axis of the Dy crystal.

Again, the average turn angle and the average opening angle of the fan structures were estimated based on the magnetization measured at 1.4 T reported in reference [17]. The schematics of the fan structure are shown in Fig. 32 for three different temperatures (128 K, 150 K and 170 K), corresponding to the three stages of the fan phase. Based on Fig. 29 and Fig. 32, the following conclusions can be made on the three stages of the fan phase during heating in the field of 1.5 T:

- (1) In stage a (114 K - 142 K), the magnetizations in some of the monolayers start to spread about the applied field and develop a fan-like modulation, while ferromagnetic

arrangement still persists in the other monolayers. Probably due to the effect of the crystal field anisotropy in the basal plane, the fan modulation in this region may involve spin-slip and is only SRO. The average period of the modulation decreases as the fan modulation becomes better-defined upon heating.

- (2) For stage b (142 K - 160 K), a pronounced and LRO fan modulation develops rapidly, coupled with the c-axis structural transition (see Fig. 22). The average turn angle of the fan grows continuously but the period stays at 10 monolayers.
- (3) In stage c (160 K - 177 K), under the influence of thermal energy, the fan modulation becomes disordered gradually. Meanwhile, the average turn angle of the fan further increases, giving an average opening angle greater than 180° at 170 K. Between 170 K and 177 K, the presence of a distorted helical modulation cannot be ruled out based on our scan along the c-axis of the crystal. A scan along the b-axis of the crystal may reveal the differences.

The intensity peaks of the diffuse scattering around 128 K, 142 K and 177 K further confirm the phase boundaries between the aforementioned magnetic phases (Fig. 29 top). Both of the transitions at 142 K and 177 K appear to be the second-order. The absence of any outstanding helifan peak between the ferromagnetic peak and the magnetic satellites rules out the possibility of well-defined helifan phase as seen in Ho [18, 19]. This is consistent with the X-ray study performed on the lattice parameter of Dy in various fields [74] and the mean-field calculations carried out in reference [15], which showed the free energy of the helifan phase is always greater than the free energy of the helix or fan.

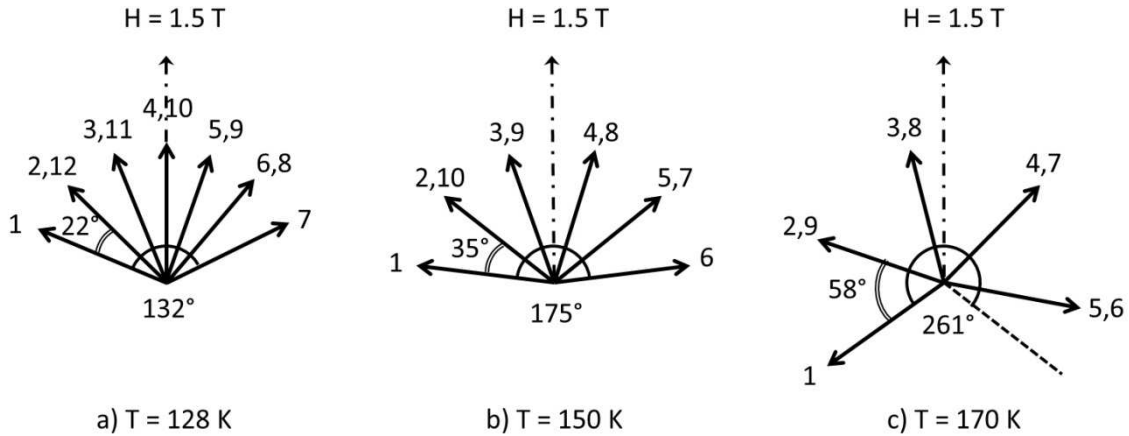


Figure 32. The evolution of the fan modulation as temperature increases in the field of 1.5 T. Only one period of the magnetic modulation is shown. The average turn angle and opening angle are estimated based on the magnetization in reference [17]. The numbers at the end of the arrows indicate the indices of the Dy (0002) atomic layers.

4.6 The refined magnetic phase diagram

Based on the above discussions, we have refined the magnetic phase diagram of Dy around the region shown in Fig. 33. The possible new phase at $\sim 140 \text{ K}$ suggested in Fig. 2 is identified as an intermediate state between the ferromagnetic and the LRO fan phase. It is mostly ferromagnetic but contains SRO fan locally. The temperature region appears wider than that indicated in Fig. 2. Some SRO fan arrangements also persist into the paramagnetic region. The boundary between the SRO and LRO fan is consistent with the onset of the c-axis structural transition in 1 T and 1.5 T. With the help from the data in reference [15], the small section of coexisting fan and helix has been mapped out.

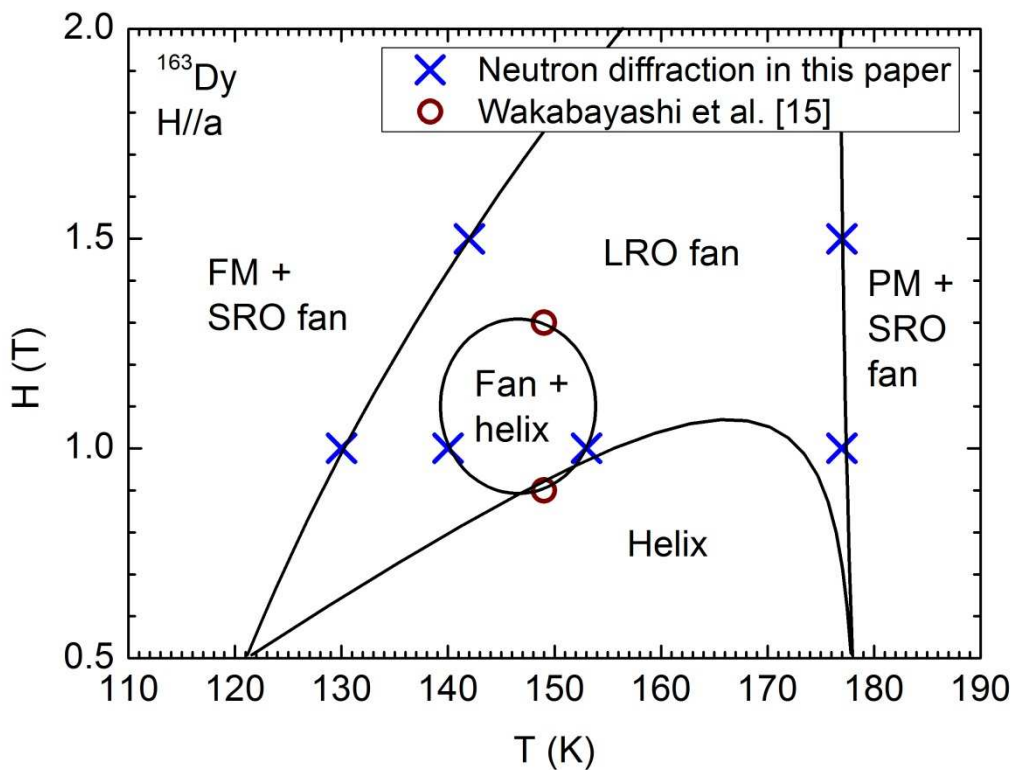


Figure 33. The refined magnetic phase diagram of Dy based on the neutron diffraction results, with the magnetic field applied along the a -axis.

5. CRYSTALLOGRAPHIC, MORPHOLOGICAL AND MACROSCOPIC MAGNETIC PROPERTIES OF Dy/Y SUPERLATTICES

5.1 Epitaxial Dy/Y superlattices grown on a-sapphire

While all of the Dy/Y superlattices in earlier studies by other groups were grown by MBE [25-30], we fabricated Dy/Y superlattices of various layer thicknesses and numbers of repeats by the DC magnetron sputtering. The home-built ADAM system is equipped with two computer-controlled shutters, a temperature controller (up to 1000 °C), a sample rotation system, and the base pressure of 10^{-9} Torr. Both Dy and Y lattices are hexagonal-close-packed (hcp) structure. The close lattice mismatch (1.6 %) between Dy ($c_{\text{Dy}} = 5.655 \text{ \AA}$) and Y ($c_{\text{Y}} = 5.641 \text{ \AA}$) ensures the weak strain within the superlattice. The magnetic easy plane of the Dy moment is the hexagonal (0002) basal plane. The helical magnetic moment rotates within the easy plane while propagating along the c-axis of Dy. The propagation of the Dy moment is coherent even with an intervening non-magnetic Y layer. Aiming to study the propagation of the helical magnetic moment of Dy, we grew the single-crystal Dy/Y superlattices in the (0002) orientation, i.e. the c-axes of Dy and Y are parallel to the surface normal.

A widely used template for the epitaxial growth of the hexagonal rare-earth thin film like Dy is the corundum sapphire (Al_2O_3) substrate and the body-centered cubic (bcc) Nb buffer layer. The epitaxial relationship between the sapphire substrate and Nb is unique and three-dimensional [75]. For example, sapphire (0002) // Nb (111), since the Nb (111) plane and the sapphire (0002) plane share the similar basis, an equilateral triangle with the length of the sides equal to 4.667 Å for the former and 4.758 Å for the latter. On the other hand, while not so

obvious, sapphire (11-20) // Nb (110) was confirmed by experiments [76]. The combination of a-plane sapphire (11-20) substrate and the Nb (110) has been proved to be an effective seeding for the epitaxial growth of Y along its c-axis [26, 77]. Fig. 34 shows a comparison of the atomic spacing in the sapphire (11-20) plane, the Nb (110) plane and the Y (0002) plane. The Nb atoms in the (110) plane form a slightly distorted hexagon (marked in red in Fig. 34), which matches closely to the hexagonal lattice in the Y (0002) plane. The initial growth of the Y (0002) lattice is strained, but the strain relieves as the Y grows thicker. Therefore, a good hexagonal Y (0002) atomic plane can be achieved by depositing a thick Y seed layer before the Dy/Y superlattice.

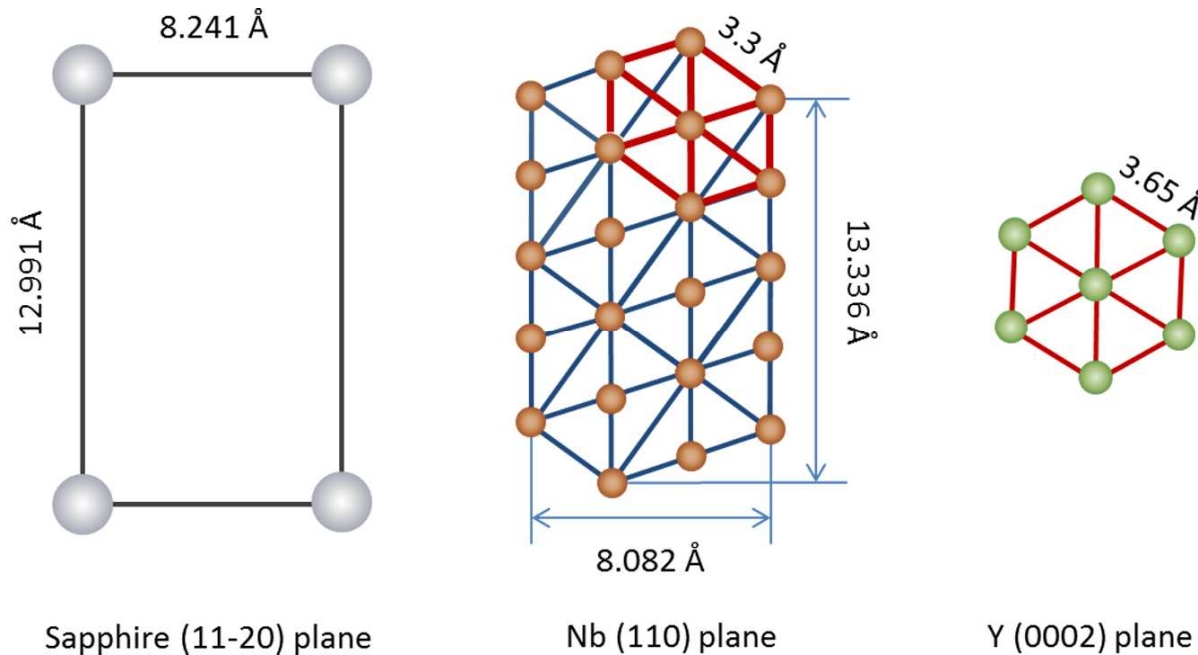


Figure 34. A comparison of the atomic spacing between the sapphire (11-20) plane, the Nb (110) plane and the Y (0002) plane.

Based on the epitaxial relationships discussed above, the layout of the Dy/Y superlattices is designed as Fig. 35 shows. Since both Dy and Y are very reactive and tend to be oxidized easily, an amorphous Nb capping layer is deposited on top in order to protect the superlattice.

The Nb buffer layer between the sapphire and the Y seed layer also serves as a protective layer which avoids the reaction between Y and Al_2O_3 .

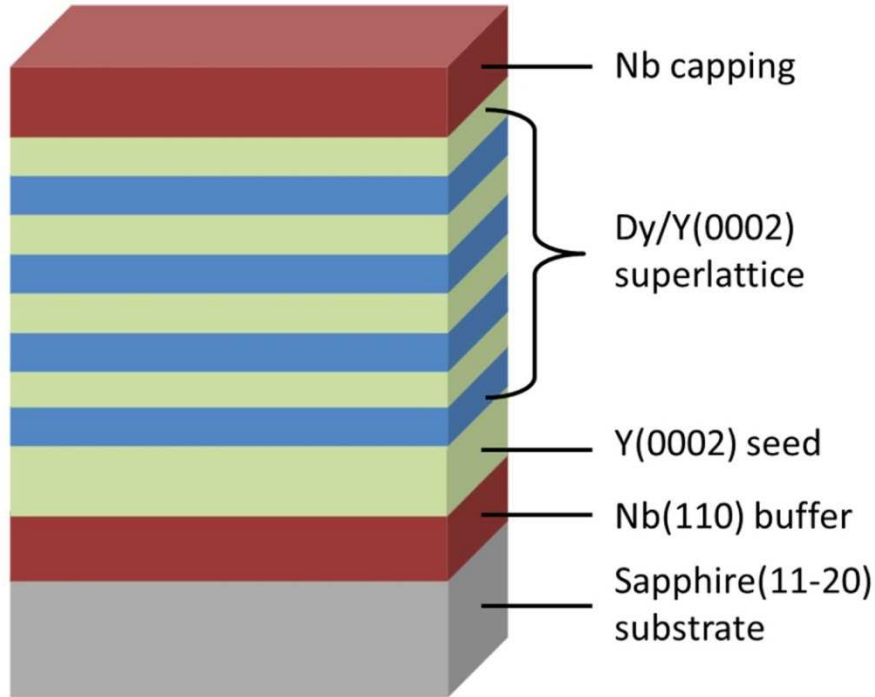


Figure 35. The layout of the Dy/Y superlattice designed in this work.

The Ar pressure during sputtering has a significant impact on the morphology of the deposited superlattice. In general, higher deposition pressure leads to rougher interface. Therefore, the minimum Ar pressure required to maintain stable plasma is used. The deposition rate of each target (Nb, Dy and Y) was calibrated for various Ar pressures. The increase of the Ar pressure gives rise to two effects, a) more target materials are ejected by the Ar bombardment per unit time, and b) more target materials are scattered by the Ar ions before they reach the substrate. The latter is dominant here since the deposition rates for all materials decreased as the increase of the Ar pressure, as shown in Fig. 36. The circles in Fig. 36 indicate the Ar pressures selected for depositing the superlattices. The deposition of alternating Dy and Y layers was

controlled by two pneumatic shutters while both magnetron guns were active for the entire deposition. For this reason, the same Ar pressure (\sim 5.6 mTorr) had to be used for both Dy and Y. As a result, Y was not sputtered at its optimum pressure (\sim 3.8 mTorr), which may adversely affect the interfacial quality in the superlattices.

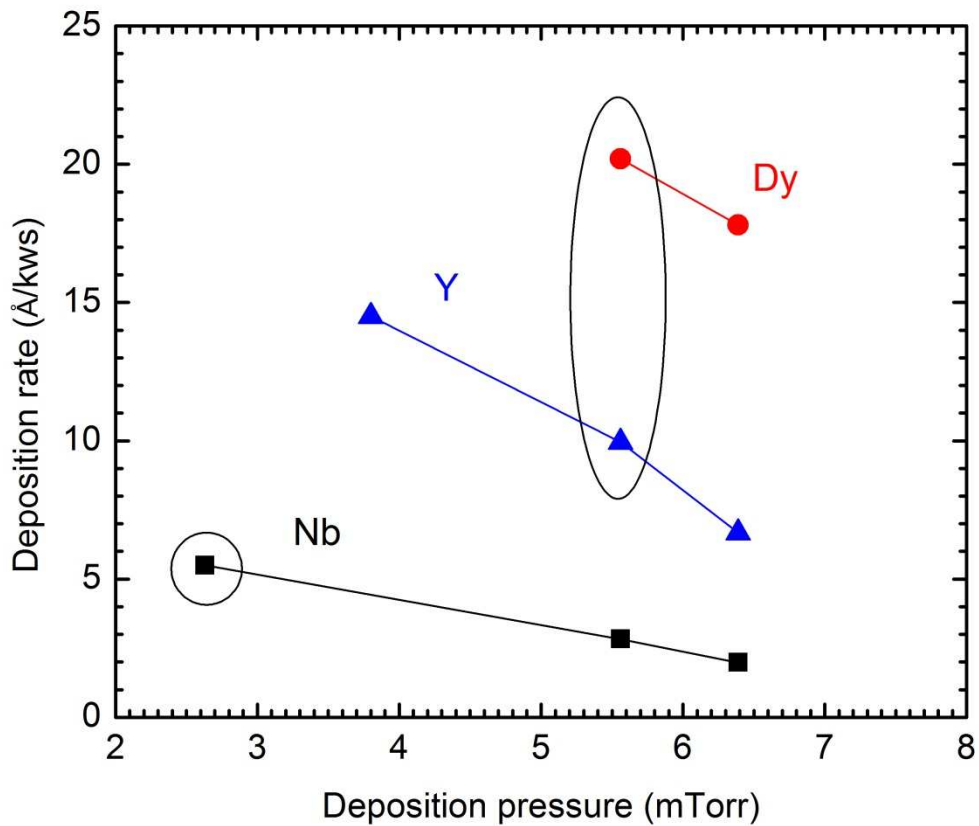


Figure 36. The deposition rate for Nb, Dy and Y as a function of the Ar pressure. The circles indicate the pressure selected for depositing the superlattices.

The deposition temperatures were optimized for the epitaxial Nb (110), Dy (0002) and Y (0002) layers based on the respective diffraction peaks and the superlattice satellite peaks measured by XRD. The intensity of a diffraction peak represents the degree of ordering of a specific orientation, while the intensity of the satellite peak reflects the separation between Dy

and Y. The results are plotted in Fig. 37. The deposition temperature for Nb (110) was optimized by growing a single Nb layer on sapphire substrate at different temperatures. The maximum Nb (110) diffraction peak was given by the sample deposited at around 900 °C. The optimum temperature (~360 °C) for Dy/Y (0002) was found with the maximum intensities of the Dy/Y (0002) diffraction peak and the +1 satellite peak on the 8-repeat Dy/Y superlattices. The optimum conditions are circled in the plots.

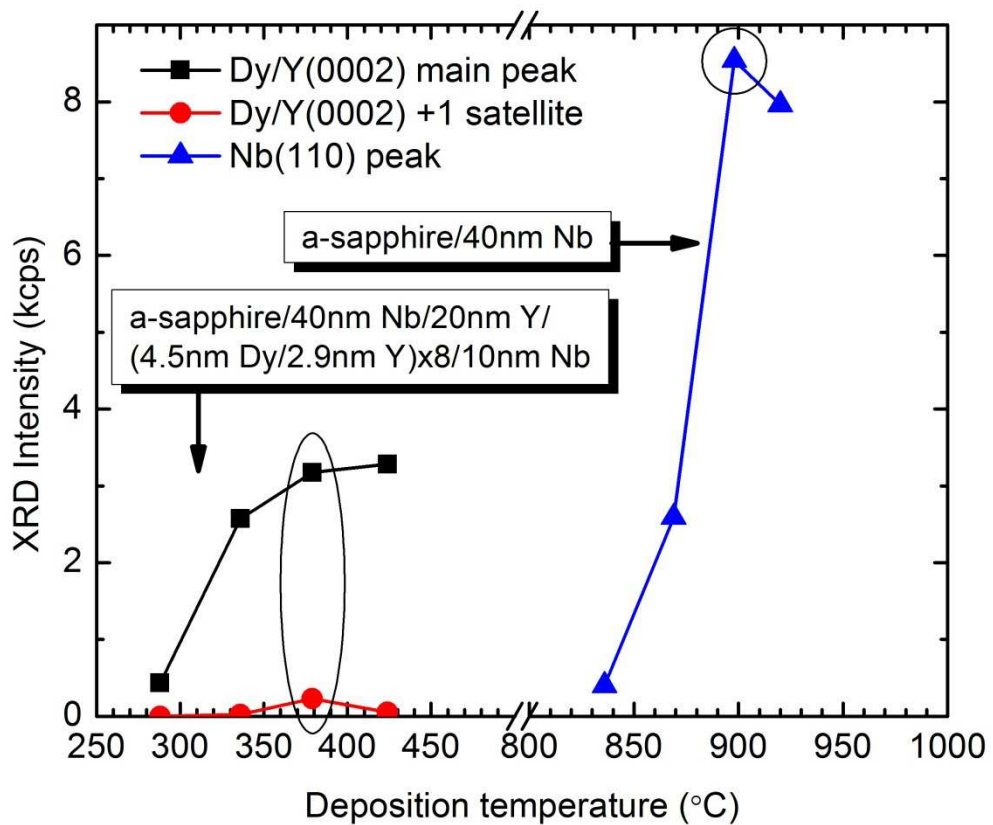


Figure 37. The optimization of the deposition temperature based on the XRD intensity of the Nb (110), Dy/Y (0002) and the Dy/Y (0002) satellite peaks. The circles indicate the temperature selected for depositing the superlattices.

A few other processes were undertaken in order to ensure both the epitaxial and interfacial quality of the Dy/Y superlattices. First, all targets were pre-sputtered before the sample deposition in order to remove the oxidized layer at the surfaces. The time of the pre-sputtering depends on the reactivity of the material. Second, the sapphire substrates were degassed at around 950 °C for at least 1 hour before the deposition of Nb buffer layer. Third, intended to avoid the contaminations on the Nb (110) surface, the growth of the Y seed layer immediately followed the deposition of Nb buffer layer. In practice, after the deposition of Nb buffer layer at 900 °C, the temperature was set to 360 °C, which was the deposition temperature for the Dy/Y superlattice. Meanwhile, the Y seed layer was deposited when the temperature was changing from 900 °C to 360 °C. The growth temperature gradient along the thickness of the Y seed layer is required since stopping the growth while cooling would result in a surface contaminated by background gas adsorption.

5.2 Crystallographic and morphological qualities characterized by X-ray

Due to the stringent requirements for the samples qualities in the neutron scattering experiments, the detailed crystallographic and morphological properties of the Dy/Y superlattices were carefully characterized by X-ray techniques. Table 5 lists the seven samples selected from over 40 Dy/Y superlattices, based on the results of X-ray characterizations, to be investigated by neutron scattering techniques. The table also lists the actual thicknesses and roughnesses of each layer determined by XRR fitting, which are discussed in more detail below. Sample a, b, c, and d were studied by PNR, while sample e, f, and g went through the elastic neutron diffraction measurements. The characterization results are explained here using sample a: [Dy₂₄/Y₇]×8 for example.

Table 5. The chemical profiles extracted by XRR for the seven superlattices selected for neutron scattering experiments.

Sample ID	Nb buffer thk. (Å)	Y seed thk. (Å)	Dy thk. (Å)	Y thk. (Å)	Dy thk. (mono-layers)	Y thk. (mono-layers)	Repeats	Nb cap thk. (Å)
a	163(5)	150(14)	69(18)	19(12)	24(6)	7(4)	8	153(20)
b	159(5)	140(20)	36(17)	39(14)	13(6)	14(5)	8	150(20)
c	341(0)	200(30)	43(25)	24(20)	15(9)	8(7)	40	100(31)
d	340(1)	200(20)	41(19)	25(14)	15(7)	8(5)	40	100(40)
e	400(2)	200(25)	45(20)	29(15)	16(7)	10(5)	54	100(30)
f	400(2)	200(30)	43(25)	28(20)	15(9)	10(7)	80	100(30)
g	400(2)	200(28)	44(25)	29(20)	16(9)	10(7)	80	100(30)

The values in the parentheses indicate roughness.

First, the film orientation was confirmed by the XRD. In Fig. 38, clear Bragg peaks are observed for Sapphire (11-20), Nb (110), and Dy/Y (0002). The corresponding second-order Bragg peaks are also shown. The resolution of the X-ray diffractometer is not sufficient to separate the diffraction peaks of Dy (0002) and Y (0002). Zooming in around the Dy/Y (0002) diffraction peak, a pair of satellite peaks shows up as a result of the modulation of the alternating Dy and Y layers. The presence of the satellite peaks suggests good contrast at the Dy/Y interface. The superlattice period (thickness of one Dy/Y bi-layer) Λ , is calculated by equation (27),

$$\Delta Q = \frac{2\pi}{\Lambda}, \quad (27)$$

where ΔQ represents the separation between the main diffraction peak and the first-order satellite peaks. The calculated superlattice period is consistent with the values obtained by XRR fitting (see Table 5). Note that for easy comparison between the X-ray and neutron data, the horizontal axis here is plotted in terms of the scattering vector ($Q = 4\pi\sin\theta/\lambda$), which is independent of the wavelength.

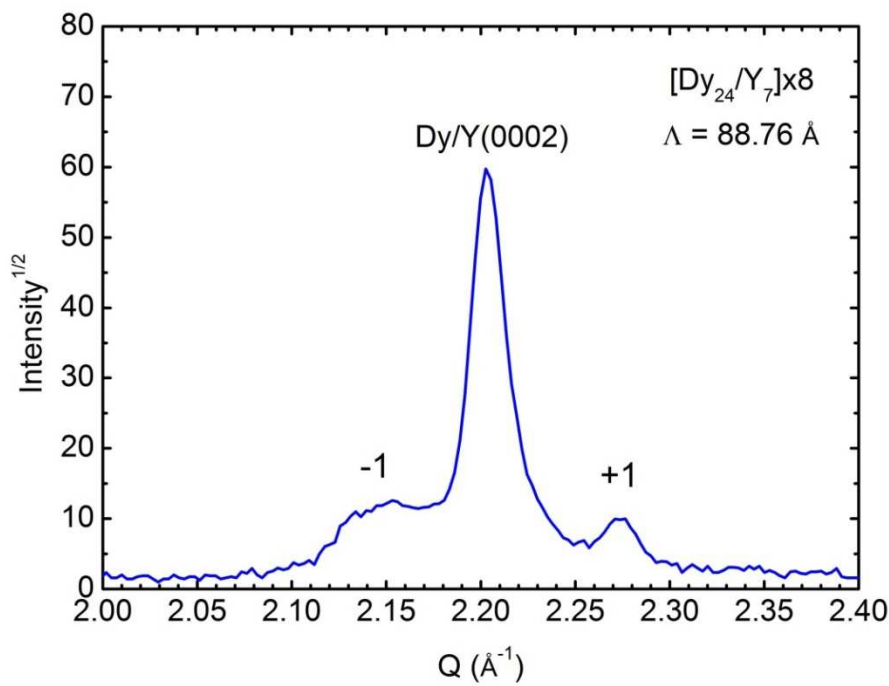
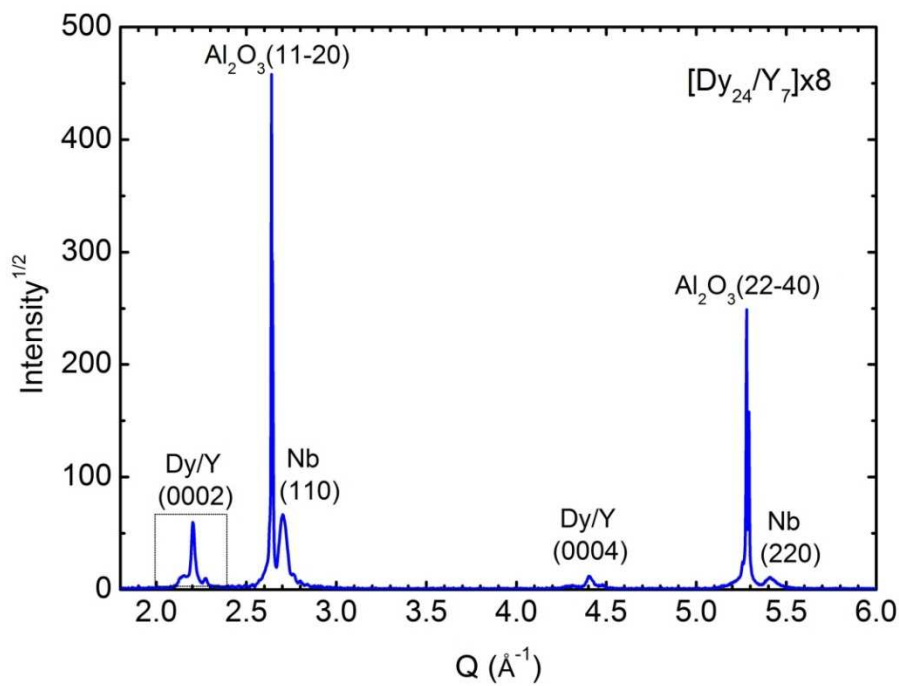


Figure 38. The XRD pattern (top) for sample a and the zoomed in region (bottom) around the $\text{Dy/Y}(0002)$ diffraction peak.

Second, XRR was performed to characterization the chemical depth profile of the multilayer, including the layer thicknesses and interfacial roughness. Fig. 39 shows the measured XRR for sample a with the fitting simulated by Wingixa, as well as the depth profile (inset) model used to generate the simulated curve. The smallest oscillations (Kiessig fringes) originate from the total thickness of the sample and the oscillations at high Q stem from the thickness of the Nb buffer layer. The Bragg peaks ($Q \approx 0.09 \text{ \AA}^{-1}$ and $Q \approx 0.15 \text{ \AA}^{-1}$) are observed for up to the second-order. The superlattice period Λ is estimated by the separation between the M-th order Bragg peak and the critical angle using equation (14),

$$Q_i^2 - Q_c^2 = \left(\frac{2\pi M}{\Lambda} \right)^2, (M = 1, 2, 3, \dots). \quad (14)$$

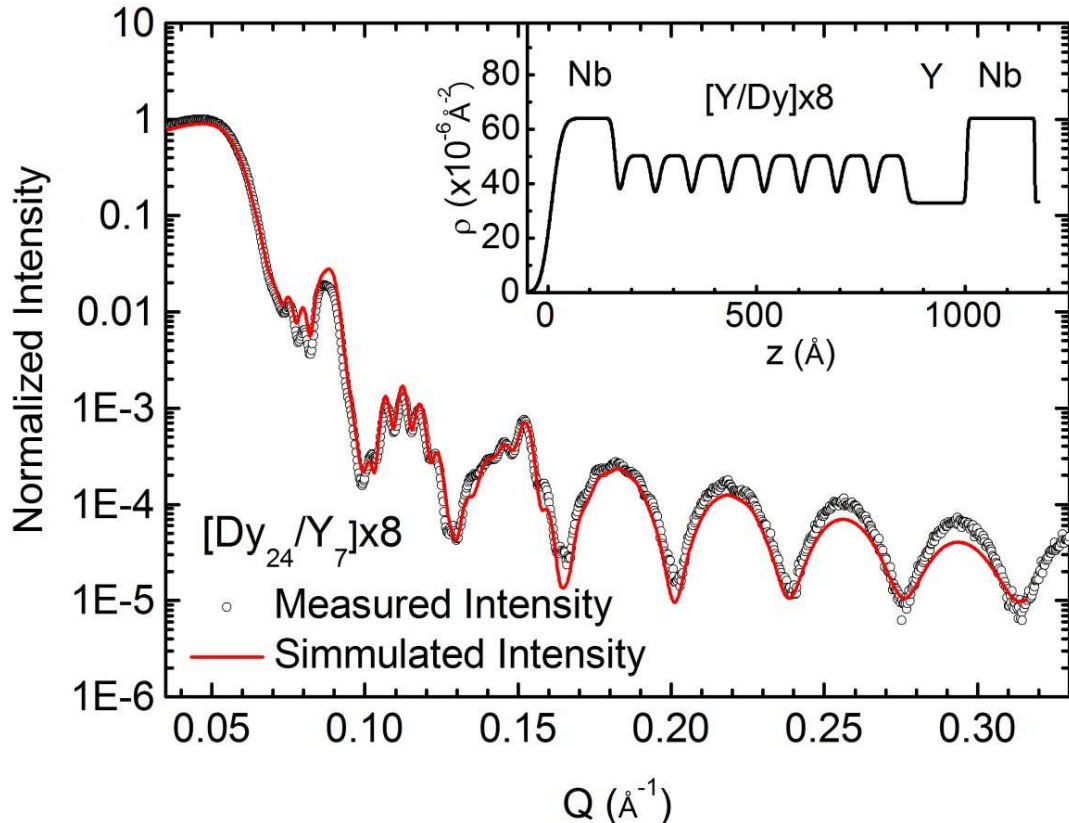


Figure 39. The measured and fitted XRR intensities for sample a. The inset shows the X-ray SLD depth profile for the superlattice extracted from fitting.

During the fitting, the bulk values were used as the densities of the materials, and only the thickness and the roughness were allowed to vary. The thickness and roughness values extracted from the fitting for all samples are shown in Table 5. In general, more roughness accumulated at the superlattice interface as the number of repeats increases. The interfacial roughness ranges from 5 to 9 atomic layers, slightly higher compared to the 4 to 5 atomic layers deposited by MBE [27, 28]. The chemical depth profiles extracted from XRR are later used in calculating the neutron reflectivity and treated as constants.

Intended to maximize the signal in the neutron scattering experiments, some of the Dy/Y superlattices were grown on the sapphire substrates of two-inch diameter. XRR was measured on 21 points over these samples in order to characterize the lateral thickness uniformity. The bi-layer thicknesses are calculated by equation (14) and plotted in Fig. 40 for sample c: $[\text{Dy}_{15}/\text{Y}_8] \times 40$. The variations of the lateral thickness are well within 5% for all samples.

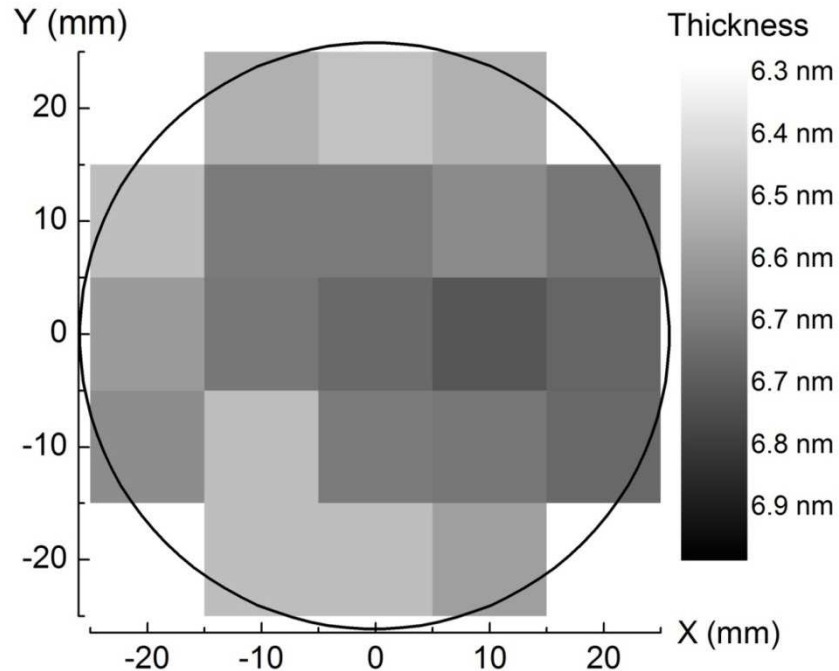


Figure 40. The uniformity of the bi-layer thicknesses over the 2-inch-diameter sample c.

Third, the rocking curve for the Dy/Y (0002) diffraction peak was measured in order to examine the c-axis distribution in the epitaxial Dy/Y superlattices. The rocking curve for sample a is shown in Fig. 41 with the full width at half maximum (FWHM) being 0.79° . The FWHM of all the other Dy/Y superlattices are very close to 1° , i.e. slightly below 1° for the 8-repeat superlattice and slightly above 1° for the 40-repeat one.

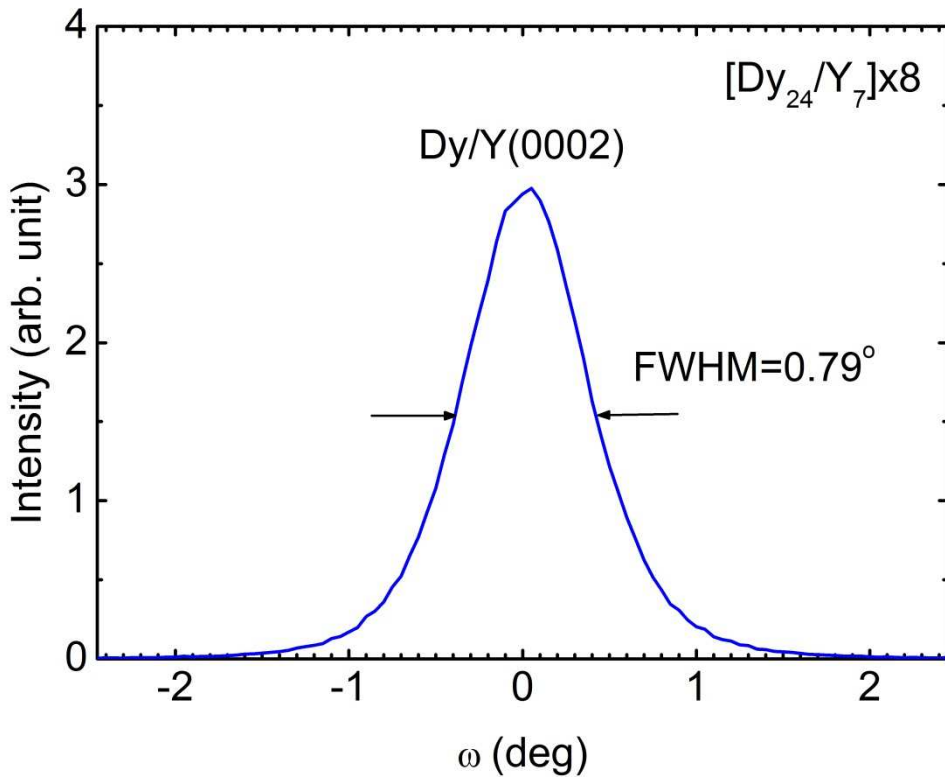


Figure 41. The rocking curve measured on sample a around the Dy/Y (0002) peak.

Last but not least, the pole figure scan was performed to confirm the film was epitaxially ordered in the lateral direction. As shown in Fig. 42, sapphire (11-20) peak and Dy/Y (10-11) peak were probed in the azimuthal scan for sample a. The sample was rotated around its surface normal (c-axis) while the instrument was oriented such that the scattering vector was equal to the

reciprocal vector of the sapphire [11-20] axis or the Dy/Y [10-11] axis. As expected, the sapphire (11-20) diffraction peaks show 2-fold symmetry (180° apart) and Dy/Y (10-11) peaks show 6-fold symmetry (60° apart). The FWHM (1.1°) of the Dy/Y (10-11) peak indicates good epitaxy in three-dimension and small distribution of the crystal axes. Fig. 42 also shows that the a-axis of the Dy/Y crystal lattice aligns at around 5° with respect to the c-axis of the a-plane sapphire substrate.

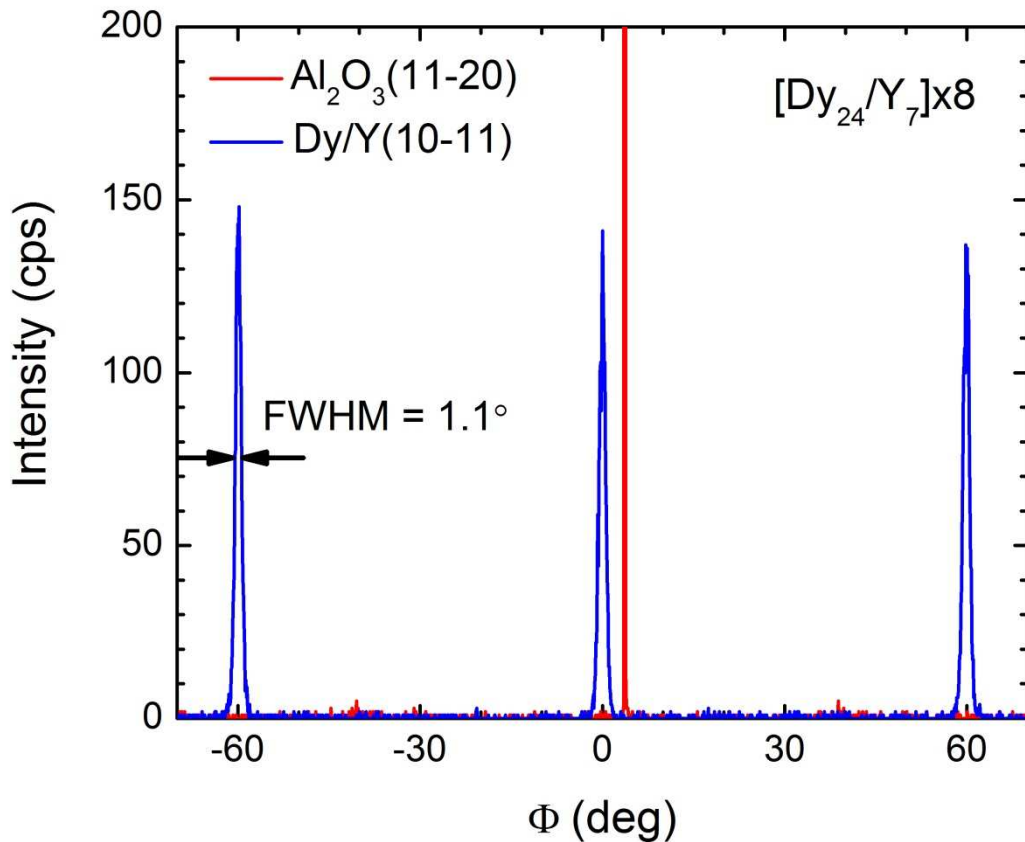


Figure 42. The pole figure measured for the Dy/Y (10-11) peak on sample a shows 6-fold symmetry.

It is worth pointing out that sample c and sample d are nominally identical: $[\text{Dy}_{15}/\text{Y}_8]\times 40$. However, due to the slight differences in the deposition temperatures, the structural

characterization shows dissimilar results. The thickness and roughness values are listed in Table 5, and more properties are specified in Table 6. There are two major differences between sample c and sample d: a) the interfacial roughness for sample c (7 to 9 atomic layers) is higher than that of sample d (5 to 7 atomic layers); b) the single-crystal Dy/Y lattices in sample c are ordered at a higher degree with less defects than the counterpart of sample d, since the integrated intensities of the Dy/Y (0002) and Dy/Y (10-11) diffraction peaks are higher in sample c than those in sample d. Another noticeable difference between sample c and d is that the average lattice spacing along c-axis differs by ~0.01 Å, characterized by the Dy/Y (0002) XRD peak positions.

Table 6. The comparison of the X-ray characterization results for sample c and d.

Sample ID	Superlattice	Dy/Y(0002) diffraction peak integrated intensity	Dy/Y(10-11) diffraction peak integrated intensity	Dy/Y(0002) rocking curve FWHM	Thickness uniformity
c	[Dy ₁₅ /Y ₈]×40	4667	901	1.15°	2.90%
d	[Dy ₁₅ /Y ₈]×40	3004	745	1.08°	3.60%

5.3 Magnetization of Dy/Y superlattice at low temperatures.

The macroscopic magnetic properties of the Dy/Y superlattices were characterized by low-temperature magnetometers, i.e. SQUID and VSM. Fig. 43 shows the temperature dependence of the magnetization for sample a, c and d during cooling in different magnetic fields applied in the sample plane, which is the easy plane for this material. The temperature dependence during heating is not shown here since no significant hysteresis was observed between the heating and cooling case. The samples are paramagnetic from room temperature down to 200 K. For cooling in a field of 1 T, the magnetization of all samples increases rapidly once the temperature drops below the Neel temperature (179 K). The first-order transition from

the helical magnetic to the ferromagnetic phase, which occurs at \sim 86 K for bulk Dy, is suppressed in the superlattice due to the lattice strain when Dy is grown on Y [25]. Instead, the helical magnetic moment is aligned ferromagnetically and goes through a second-order phase transition under the impact of the large applied field (1 T). The magnetization shows saturation below 30 K. The calculated saturation magnetization for Dy is \sim 3100 emu/cc when assuming all Dy moments are aligned ferromagnetically. However, the magnetizations at 5 K and 1 T are only a fraction of the theoretical value. There are two possible sources of the missing magnetization in the superlattices: a) the defects in the Dy crystal lattice are magnetically dead, hence reduce the overall magnetization; b) the field of 1 T is not sufficient to saturate all the Dy moments and the missing moment is still present in the helical or fan state, which could not be sensed by the magnetometer since it only measures the average magnetization. Based on the magnetic hysteresis loops measured at 5 K (Fig. 44), the magnetization is close to saturation at 1 T. Therefore, the unsaturated Dy moments may only yield a small portion of the missing magnetization in the superlattices. The magnetically dead defects are the main contribution. The fact that sample c has higher magnetization than that of sample d during field cooling in 1 T agrees well with the findings by X-ray diffraction that there are less structural defects in sample c than in sample d. On the other hand, the defects accumulate as the number of repeats is increased, since the magnetizations for the 40-repeat sample c and d are significantly lower than the magnetization for the 8-repeat sample a.

Under zero field or low field (5 to 10 mT) cooling, the Dy/Y superlattices are expected to stay in the helical state below the Neel temperature. Very small net magnetization is induced and increases slowly as temperature goes down (Fig. 43 bottom). The cusps, seen around 150 K, correspond to the second-order phase transition from the paramagnetic state to the helical state.

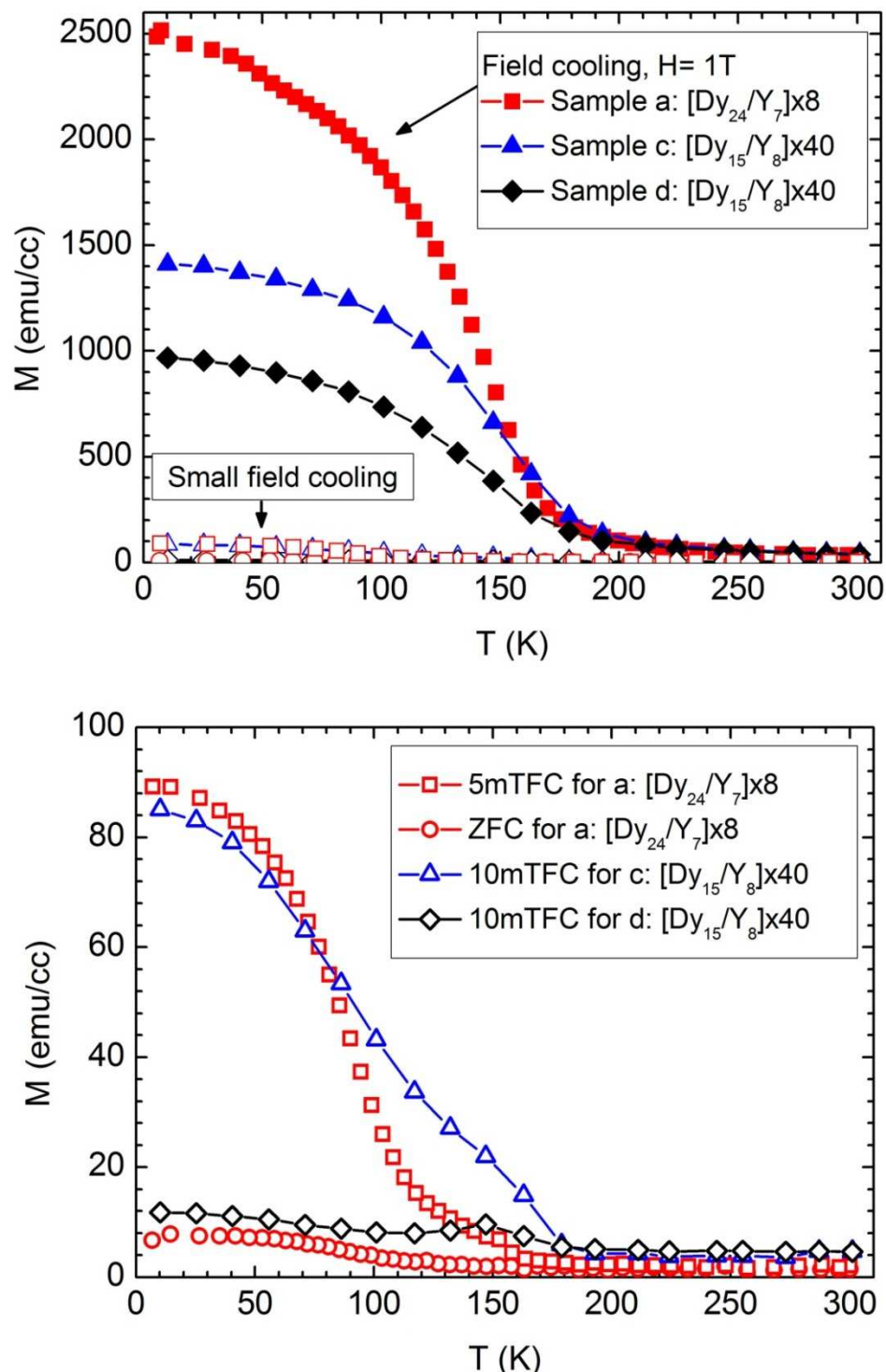


Figure 43. The temperature dependence of the magnetization for sample a, c and d during cooling in different magnetic fields applied in the sample plane.

Compared to sample d, sample a and sample c can be easily magnetized ferromagnetically by a small field as seen in the increase of the net magnetization during cooling. Even cooling in a field of 10 mT, sample d stays at the helical state with insignificant net magnetization. The coupling between the helical magnetic moments in sample d is strong enough to overcome the Zeeman energy induced by the applied field. The structural defects in sample d may play an important role in the above behaviors. Sample c has higher magnetization than sample d at both cooling fields, indicating more ferromagnetic and less helical component in sample c. Since the helical alignment of the Dy moment is a result of the RKKY interaction, which depends on the distance between the adjacent Dy layers, more interdiffusion at the Dy/Y interface would weaken the interaction and cause the Dy moments in sample c easier to be aligned by an external field. When cooling in no field, sample a stays at the helical state as the net magnetization is close to zero.

Fig. 44 shows the in-plane hysteresis loops measured at low temperatures for sample a (bottom) and c (top). The hysteresis loops for sample c were taken at the helical magnetic state (100 K) and the ferromagnetic state (10 K) respectively. The helical state is magnetically softer than the ferromagnetic state. The field of 200 mT is not sufficient to saturate the 40-repeat Dy/Y superlattice. The 8-repeat sample a is saturated by a field of 1 T at 5 K. Fig. 44 (bottom) also shows large coercivity (\sim 500 mT) and high remanence magnetization (\sim 0.9M_s) for sample a at 5 K.

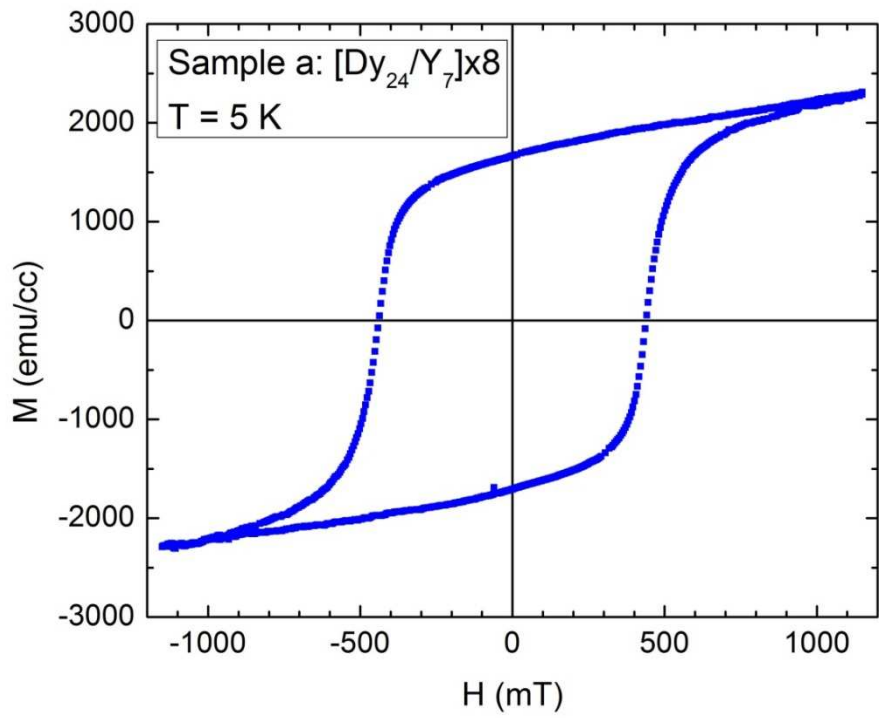
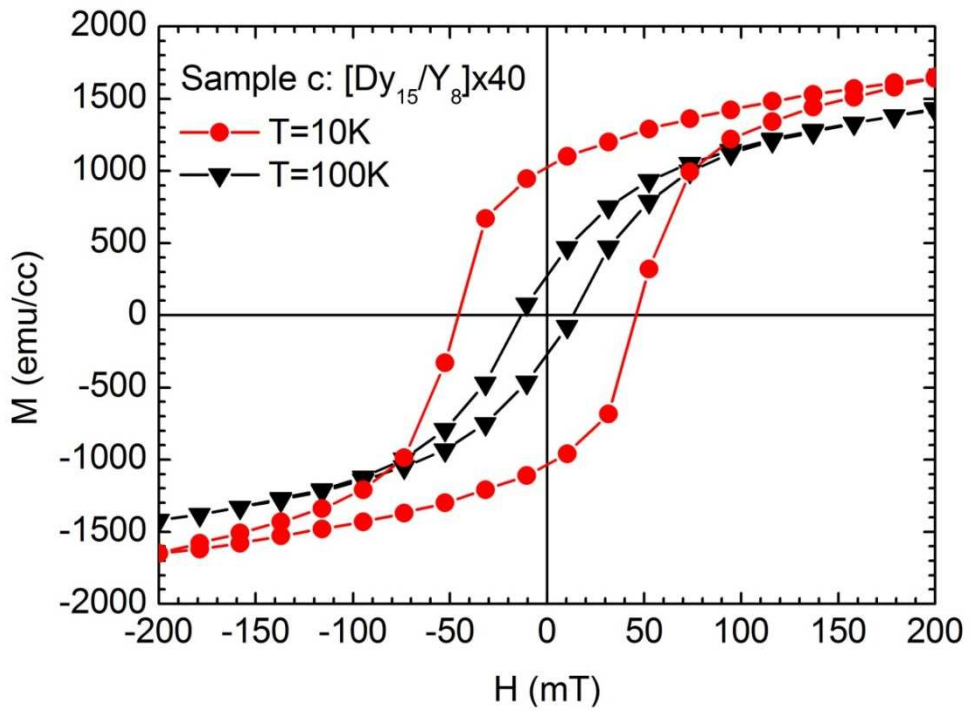


Figure 44. The in-plane hysteresis loops measured at 5 K for sample a (bottom) and 10 K, 100 K for sample c (top).

6. MICROSCOPIC MAGNETIC STRUCTURES IN Dy/Y SUPERLATTICES

6.1 Helical magnetic structures observed by neutron diffraction

Neutron diffraction was performed on a $[Dy_{16}/Y_{10}] \times 214$ superlattice (by stacking samples e, f and g, see Table 5) with no field applied at the Fixed-Incident-Energy Triple-Axis Spectrometer (FIE-TAX) located at beam line HB-1A of the HFIR, ORNL. The raw diffraction patterns are plotted in Fig. 45 as a function of temperature and the scattering vector. The plot is also shown in logarithm scale (bottom) for clarity. In the scan region, no significant background signal needs to be subtracted. The central diffraction peak ($Q_n \approx 2.21 \text{ \AA}^{-1}$) is temperature independent in intensity. Therefore, there is negligible ferromagnetic component throughout the temperatures. The central peak originates solely from the interaction between the neutron and the Dy nuclei in the (0002) planes. The magnetic satellites ($m\pm$) are corresponding to the periodicity of the magnetic modulation, i.e. the helix structure. The nuclear harmonic peaks (n_{SL}) and magnetic harmonic peaks (m_{SL}), which result from the bi-layer structure, are marked in Fig. 45. The positions of the Dy (0002) nuclear peaks remain nearly constant as the temperature is changed. The slight shift of the nuclear peaks with temperature is owing to the temperature dependence of the interplanar spacing of Dy along the c-axis [25]. The Dy nuclear peak and the nuclear harmonic peak here can be analogous to the Dy (0002) peak and the +1 satellite peak measured by x-ray diffraction (see Fig. 38). The position of the central nuclear peak reveals the average spacing between the (0002) planes to be around $2\pi/Q = 2.84 \text{ \AA}$ in the Dy/Y superlattice.

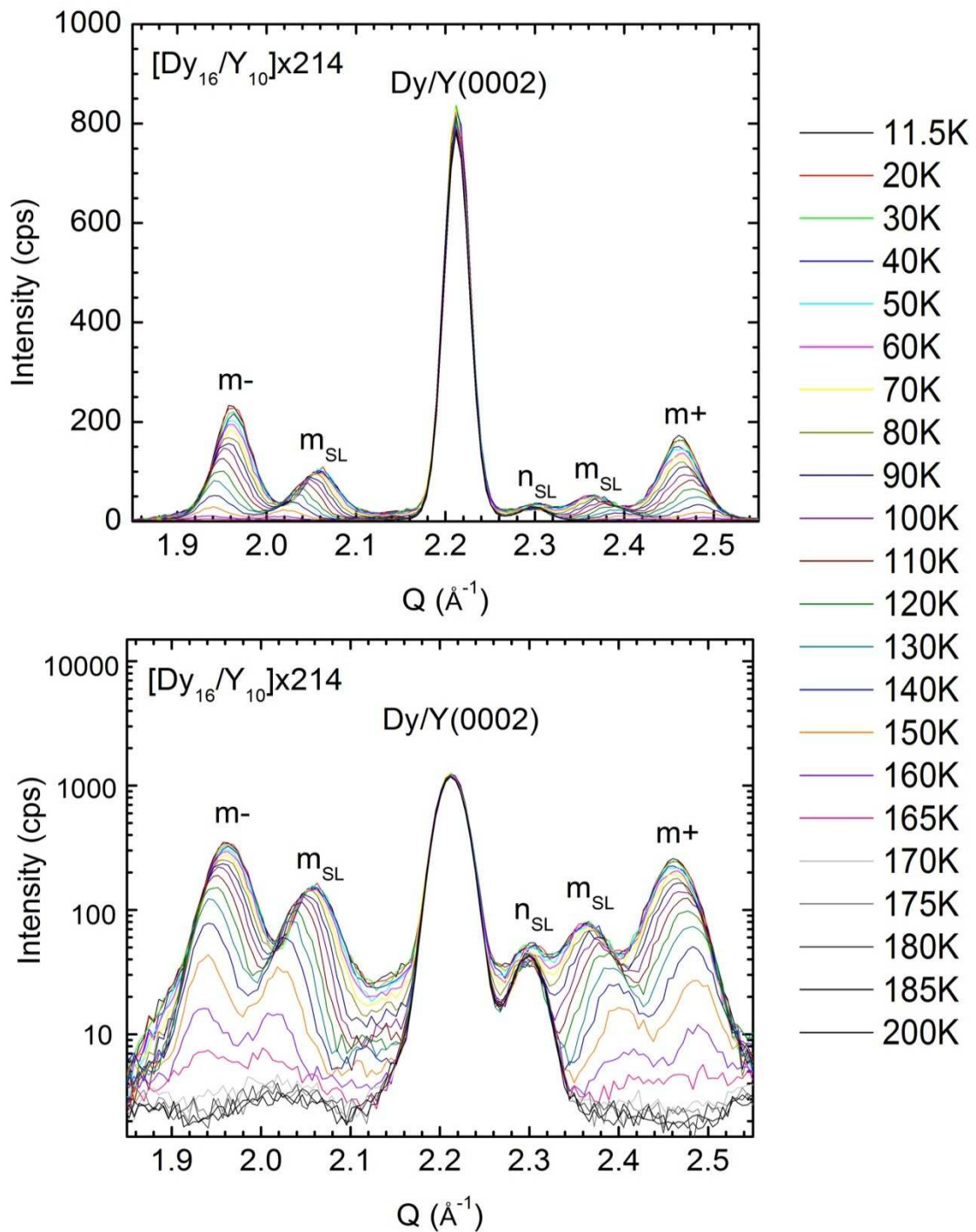


Figure 45. The neutron diffraction patterns measured along the c-axis of the $[Dy_{16}/Y_{10}] \times 214$ superlattice as a function of temperature with no field applied. The intensities are shown in both the linear (top) and the logarithm (bottom) scales.

The nuclear harmonic peak is pronounced at around $Q_{nSL} = 2.3 \text{ \AA}^{-1}$, and hence confirms that the chemical period of the superlattice is reasonably at $\Lambda = 2\pi/\Delta Q_n = 69.81 \text{ \AA}$. The asymmetry of the nuclear harmonic peaks was also observed in the x-ray diffraction data, and it is probably due to the lattice mismatch along the c-axis between the Dy and Y layers [25]. The intensities of the magnetic satellites increase as the temperature decreases. Meanwhile, the satellite peaks move toward the Dy (0002) nuclear peak (Fig. 45). The separation between the magnetic satellites and the central nuclear peak provides information about the period of the helical magnetic structure in the superlattice, corresponding to a 360° turn of the Dy magnetic moment along the c-axis, by equation (27)

$$\Delta Q_m = Q_n - Q_m = \frac{2\pi}{\Lambda_m}. \quad (27)$$

The magnetic period Λ_m is the weighted average over the Dy and Y layers, where the magnetic moments turn by different angles. For a $[\text{Dy}_a/\text{Y}_b] \times n$ superlattice, the relationship between the magnetic period and the turn angles is given by

$$\frac{a\varphi_{Dy} + b\varphi_Y}{360^\circ} = \frac{ad_{Dy} + bd_Y}{\Lambda_m}. \quad (65)$$

Here $d_{Dy} = 2.824 \text{ \AA}$ and $d_Y = 2.867 \text{ \AA}$ are the interplanar spacing along the c-axis of the Dy and Y lattices, respectively. φ_{Dy} is the turn angle of the magnetic moment between the successive atomic planes within the Dy layer, and is temperature dependent. φ_Y is the effective turn angle of Dy moment through every Y atomic plane, and the value ($\varphi_Y \approx 51^\circ$) has been reported as temperature independent by both experiments and calculations [25]. For samples e, f and g, with $a = 16$ and $b = 10$, the turn angles in Dy (φ_{Dy}) are calculated based on equation (27) and (65). The result is plotted in Fig. 46 as a function of the temperature. The turn angle in Dy decreases from 45° to 33.5° upon cooling from 170 K to 10 K. The turn angle locks at around 34° when the

temperature is below 50 K. The similar behavior was reported in previous studies [27, 28], but different lock-in angles have been observed, ranging from around 30° to 38°, depending on thicknesses of the Dy and Y layers. Our value is in reasonably good agreement.

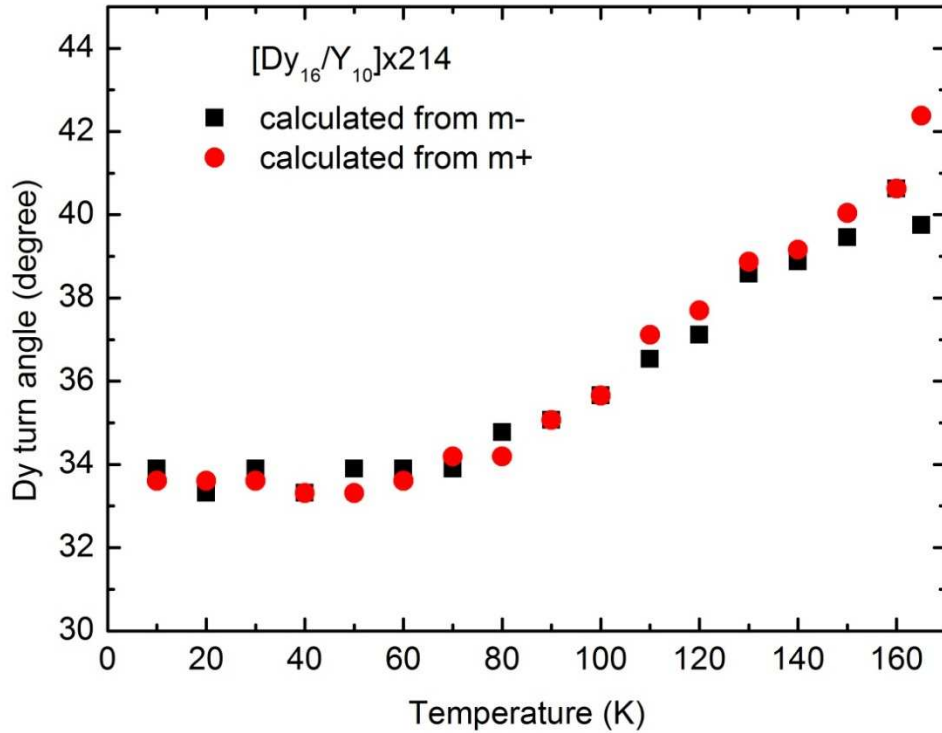


Figure 46. The temperature dependence of the average turn angle of the magnetic moment in the Dy layers, calculated by the positions of the magnetic satellite peaks in Fig. 45.

Fig. 47 shows the temperature dependence of the intensity of the left magnetic satellite (m-). The intensity of the m- peak reflects the magnetic moment in the helical structure. The temperature hysteresis is typical for this system, where upon cooling the competition between the handedness of the structures suppresses the transition around the Neel temperature. Upon heating, the disordering of all right (or left) handed helical structures requires a higher temperature to complete [78].

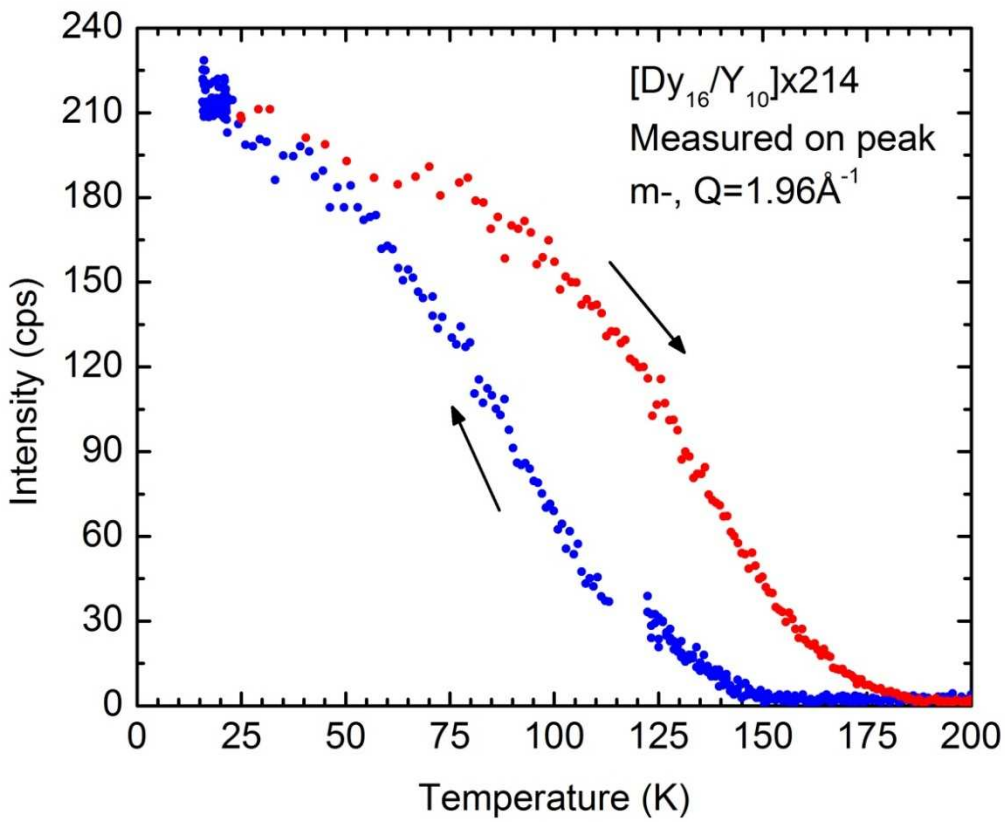


Figure 47. The thermal hysteresis of the intensities of the m - magnetic satellite.

6.2 Helical spin configuration measured by specular PNR

PNR experiments were performed on sample a, b, c and d (see Table 5) at the MR, a polychromatic magnetic reflectometer that uses neutron wavelengths of 1.8 \AA to 14.0 \AA with 98.5% polarization at the Spallation Neutron Source (SNS) in ORNL. The sample was placed with the field applied in the film plane (Fig. 48). The neutrons were polarized parallel or antiparallel to the applied field. The incident neutrons of various wavevectors hit the sample at the same angle, but were reflected along different angles by the chemical and magnetic structures in the sample. The signal was recorded by a time-resolved two dimensional position sensitive

detector (PSD) and then converted to a 3-D intensity map which included both specular ($Q_x = 0$) and off-specular ($Q_x \neq 0$) reflections (Fig. 48). The Dy/Y superlattices were measured at various temperatures, fields with different cooling histories, covering the paramagnetic, helical antiferromagnetic and ferromagnetic states (Table 7).

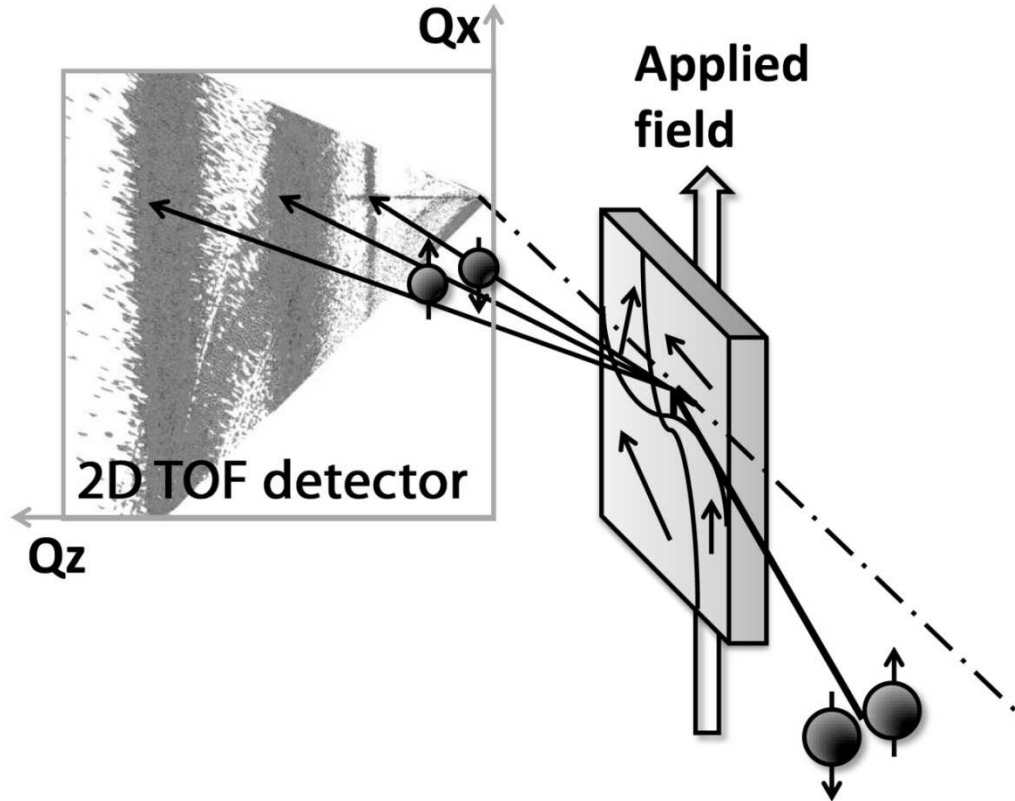


Figure 48. The schematic of the PNR experiment. The applied field and neutron polarization are both parallel with the film plane.

The specular reflectivity measurement probes the profile of the optical index along the film normal (Q_z) usually in terms of four cross-sections: two non-spin-flip cross-sections, R^{++} (R^-), and two spin-flip cross-sections, R^+ (R^{-+}) [55]. In our experiment, only two independent cross-sections ($R^+ = R^{++} + R^{+-}$ and $R^- = R^{--} + R^{-+}$) were used due to the absence of the analyzer. However, the contribution of the spin-flip cross-sections can be negligible based on our

assumption that there is no net magnetization perpendicular to the applied field. The magnetic off-specular scattering would prove the presence of the lateral helical domains and also provides information about the magnetic correlation length. Note that in this experiment geometry, the neutron is not sensitive to the chirality of the helical spin, which requires a measurement with the incident neutrons polarized perpendicular to the helical magnetization [29, 30]. Using the chemical depth profile extracted from XRR, the magnetic depth profile of the superlattices are determined by comparing the measured PNR to the simulations, which is generated by the transform matrix associated with the sample depth profile [79].

Table 7. The summary of the cooling fields, measurement temperatures and fields and the resultant magnetic states for sample a, b, c and d which went through the PNR measurements.

Measurement temperature	5K						150K	200K
	Zero		10mT	1.15T				
Cooling field	3mT	1.15T	10mT	5mT	440mT	1.15T	5mT	3mT
Measurement field								
a: $[\text{Dy}_{24}/\text{Y}_7] \times 8$	HM	FM		FM		FM		PM
b: $[\text{Dy}_{13}/\text{Y}_{14}] \times 8$	HM	FM		FM		FM		
c: $[\text{Dy}_{15}/\text{Y}_8] \times 40$			HM+FM		FM	FM		
d: $[\text{Dy}_{15}/\text{Y}_8] \times 40$			HM	FM+HM		FM	HM	

Subscripts of Dy and Y denote the number of atomic layers.

PM: paramagnetic state

HM: helical magnetic state

FM: ferromagnetic state

The measurement conditions (temperature, field and cooling history) of the PNR are summarized in Table 7 for Dy/Y superlattices (a - d). There is no fundamental difference between the results found for samples a and b, or c and d. Here we focus on sample a and d to interpret the microscopic magnetic properties of Dy/Y superlattices measured by PNR. First of all, at 200 K, 20 K above the Neel temperature of Dy, the PNR shows the reflectivity of

paramagnetic origin (no divergence between R^+ and R^- channels) (Fig. 49a). The simulated reflectivity is generated by the chemical depth profile extracted from XRR (Fig. 39), and agrees well with the measured data. When cooled under a high field (1.15 T) and measured at the same field, the reflectivity at 5 K exhibits strong ferromagnetic ordering (Fig. 49b), which is consistent with the magnetometer results (Fig. 43). After reducing the field to 5 mT, the remanent magnetization is still highly ferromagnetic (Fig. 49c). The simulation is performed with the fixed chemical depth profile and a ferromagnetic model, so the magnetic SLD is the only variable. The magnetic SLD is around $7 \times 10^{-6} \text{ \AA}^{-1}$ for the ferromagnetic state and $6 \times 10^{-6} \text{ \AA}^{-1}$ for the remanent state, in contrast to $9 \times 10^{-6} \text{ \AA}^{-1}$ if all the Dy moments are magnetized. When measured in 10 mT after zero-field cooling to 5 K, the sample is expected to be helical magnetic. The reflectivity appears very similar to be a paramagnetic state, except for a broad peak at $Q \approx 0.115 \text{ \AA}^{-1}$ (Fig. 49d). The simulation with a helical magnetic model confirms that it is a magnetic peak, which originates from the periodicity of the helical modulation. The parameters in the helical model involve not only magnetic SLD but also the angle between the applied field and the Dy moment. The position of the magnetic peak is sensitive to the turn angle of the Dy moment. The magnetic peak is not very pronounced since there are only 8 repeats, and any inhomogeneity in the helical turn angle may broaden the peak. A much sharper magnetic peak could be obtained in the simulation if the repeats were set to 40. The magnetic SLD of the helical magnetic state is found to be around $1 \times 10^{-6} \text{ \AA}^{-1}$, and the turn angle is around 35° , which is close to the turn angles measured by neutron diffraction previously (Fig. 46). Again, the turn angles have been reported locking at different values ranging from 30° to 38° in previous studies of similar superlattice structures [28, 80]. The insets of Fig. 49 show the depth profile of the total SLD, which is the sum of nuclear and magnetic SLD, for neutrons of the two polarization states.

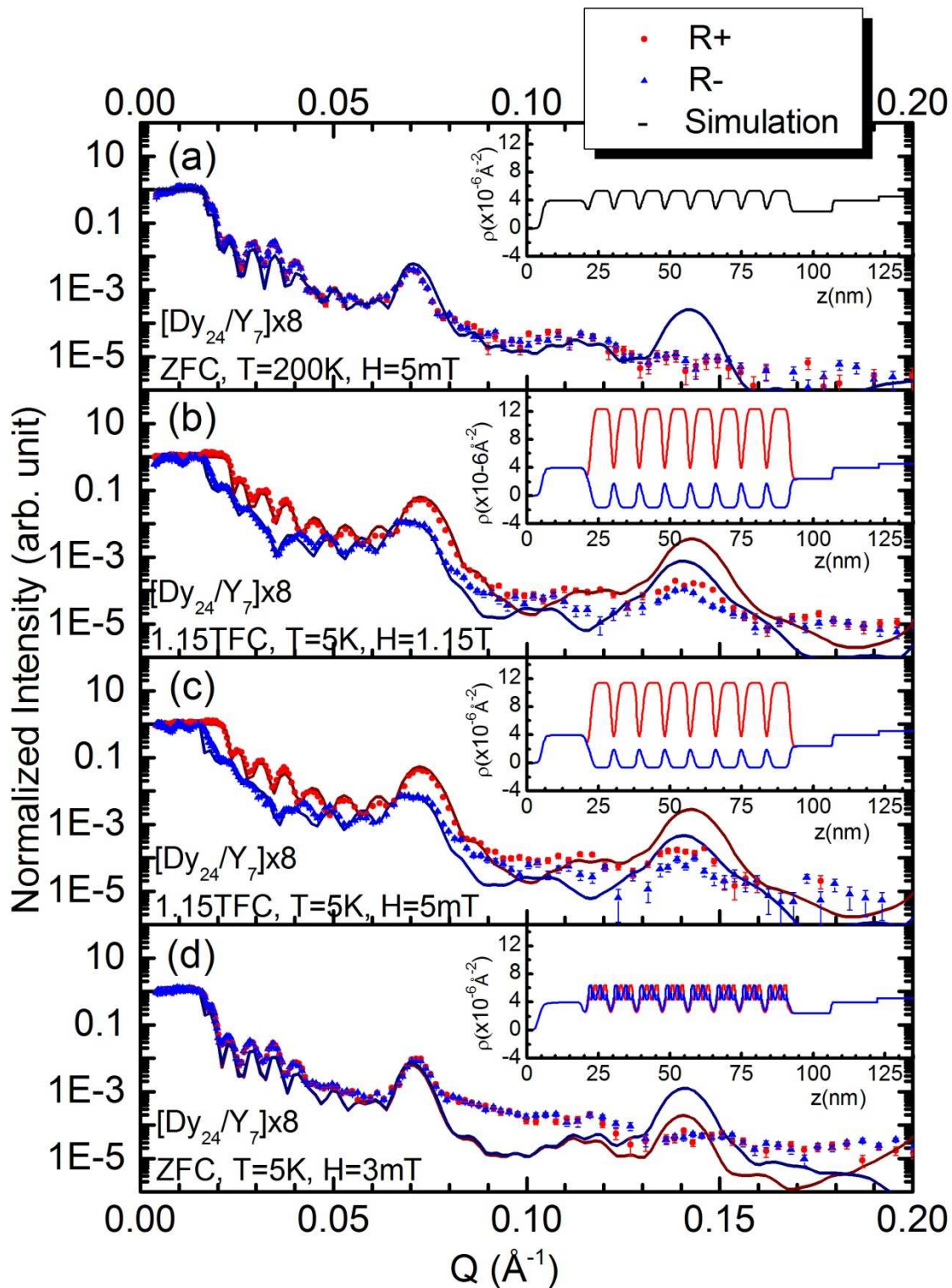


Figure 49. The measured PNR intensities and simulations for sample a ($[Dy_{24}/Y_7] \times 8$) under different cooling histories, measurement temperatures and fields, covering a) PM state, b) FM state, c) remanent FM state, and d) helix state. The total neutron SLD profiles are shown in the insets.

Fig. 50 shows the PNR results for the 40-repeat samples (c and d). Sample c and d were measured under the same condition (at 5 K with 10 mT field), which is expected to induce the helical ordering. The first Bragg peak at approximately $Q \approx 0.1 \text{ \AA}^{-1}$ comes from the chemical modulation of the superlattice structure, and shows consistency with the first Bragg peak measured by XRR. The two magnetic peaks at around $Q \approx 0.15 \text{ \AA}^{-1}$ and $Q \approx 0.25 \text{ \AA}^{-1}$ originate from the modulation imposed by the nuclear multilayer periodicity on the helical magnetic periodicity. Thus the separation between the magnetic peak (M1) and the magnetic harmonic peak (M2) is equal to the first Bragg peak position in Q space [30]. The divergence of the R^+ and R^- curves at the first Bragg peak for sample c (Fig. 50 top) indicates a ferromagnetic component of the sample, agreeing with the previous assumption that it is easier to magnetize sample c ferromagnetically by a small field. On the other hand, sample d shows negligible ferromagnetic character at the chemical Bragg peak (Fig. 50 bottom). Both nuclear and magnetic peaks agree well with the simulations generated by a helical magnetic model with a turn angle of $\sim 37^\circ$. Fig. 51 shows two more cases of the helical structures observed by PNR. At the remanent state of sample d, the helical structure is found to be coexistent with ferromagnetic ordering at 5 K (Fig. 51 top). Warming up to 150 K from the remanent state, the helical magnetic peaks become sharper and the ferromagnetic feature vanishes (Fig. 51 bottom). At the same time, the magnetic peaks shift to a larger Q, and the turn angle given by simulation is $\sim 43^\circ$.

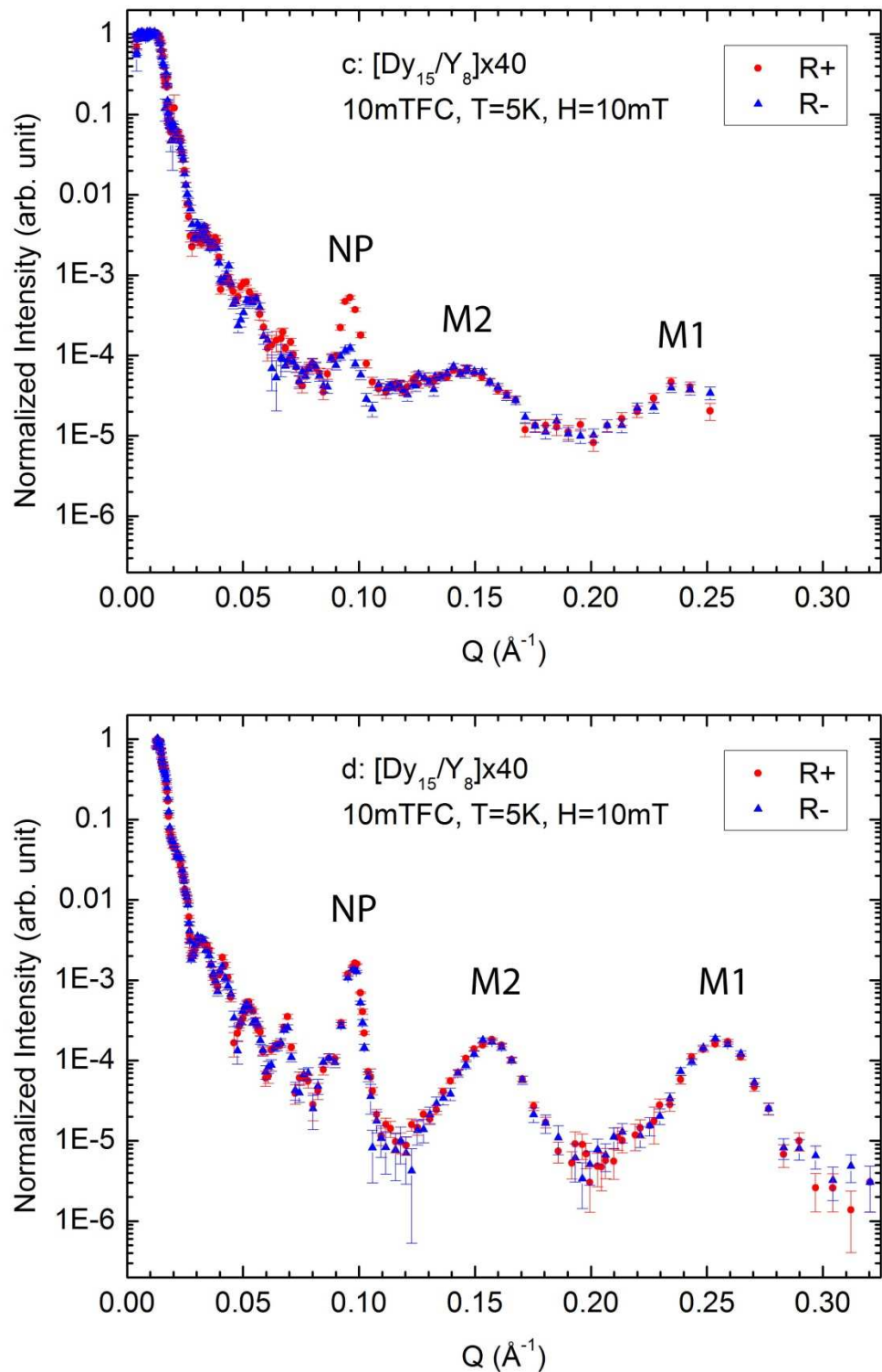


Figure 50. At 5 K and 10 mT applied field, the PNR measurements show the helical magnetic peaks and ferromagnetic components for sample c (top) and the helix modulation with no net magnetization for sample d (bottom).

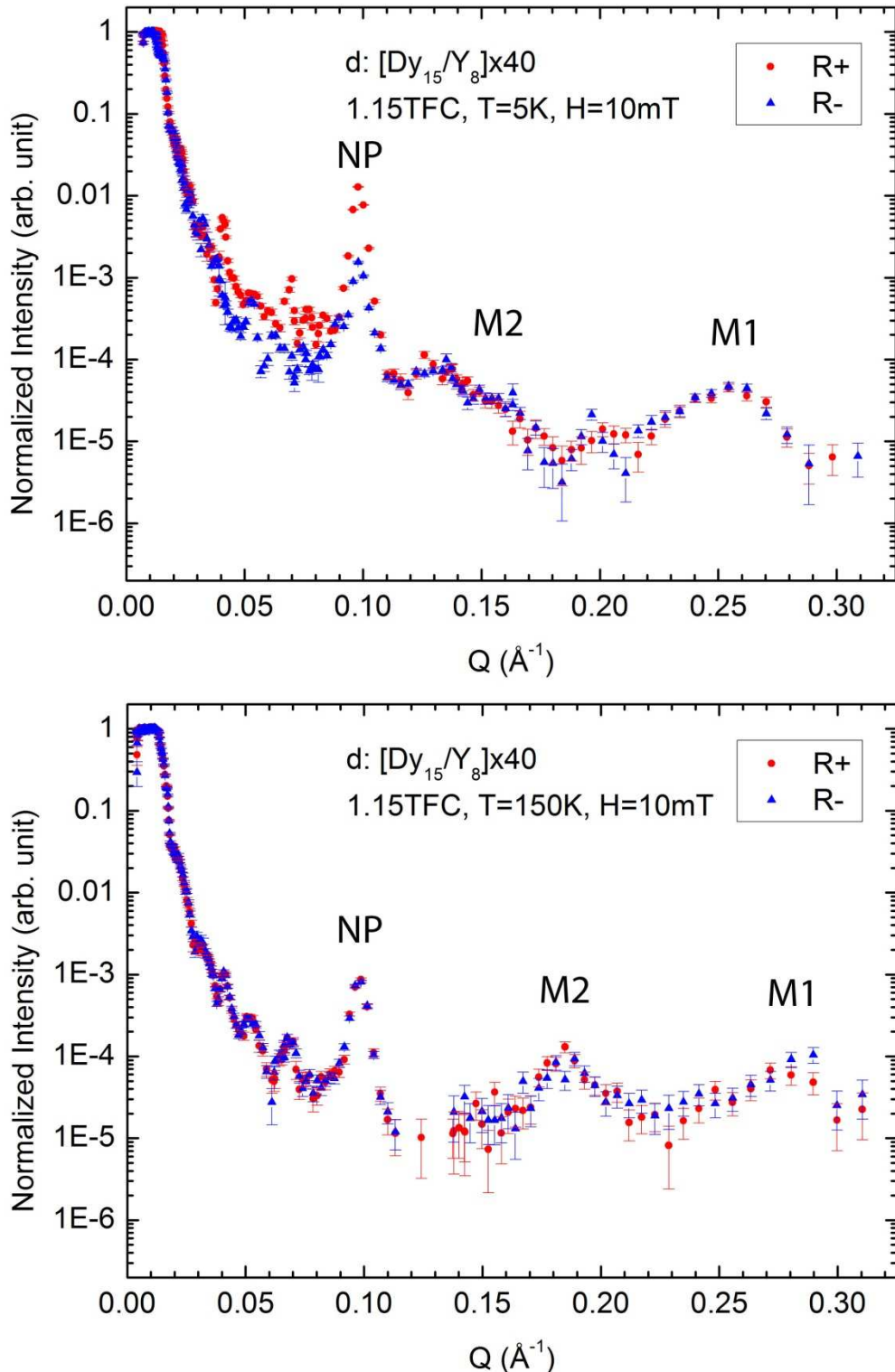


Figure 51. For sample d, the PNR measurements show the helical magnetic peaks and ferromagnetic components at the remanent state at 5 K (top) and the helix modulation with negligible net magnetization after warming up to 150 K (bottom).

6.3 Evidence of helical antiferromagnetic domains shown in off-specular PNR

Off-specular Bragg sheets were observed around both chemical Bragg peaks and magnetic peaks. The off-specular reflection around the structural peak is a sign of lateral structural roughness, and the Bragg sheets around the helical magnetic peaks are the evidences of the lateral magnetic inhomogeneity, which are essentially the lateral magnetic domains (Fig. 52). We assume that the helical magnetic domains are present in terms of left-handed or right-handed chirality and distributed symmetrically about the external field such that there is no net magnetization perpendicular to the applied field thus the Zeeman energy is minimum. The magnetic Bragg sheets are most pronounced at the conditions where the largest magnetic peaks are observed, i.e. at 5 K with 10 mT field after cooling in 10 mT for sample c and d. The 3-D reflectivity contours are plotted as a function of in-plane momentum transfer (Q_x) and out-of-plane momentum transfer (Q_z) in Fig. 52. The intensity ridge located along $Q_x = 0$ is the specular reflectivity showed in Fig. 50. The off-specular rocking curves are extracted by taking the intensity versus Q_x data at the specular peaks of Q_z . After fitting the rocking curves around the magnetic peaks by a Lorentzian function, the lateral correlation length (L), which is a measure of the typical domain size, is estimated by the FWHM of the diffuse scattering peaks [35, 62-64],

$$L \approx \frac{2\pi}{\text{FWHM}} \approx 100 \text{ nm.} \quad (66)$$

The similar lateral correlation length was observed in the Dy thin film grown on W (110) [81] and the Y/Dy/Y tri-layer [82]. In contrast, the lateral correlation length of the film roughness calculated from the X-ray rocking curves is two orders of magnitude lower.

[Dy₁₅/Y₈]x40 superlattices: 10mT FC, T=5K, H=10mT

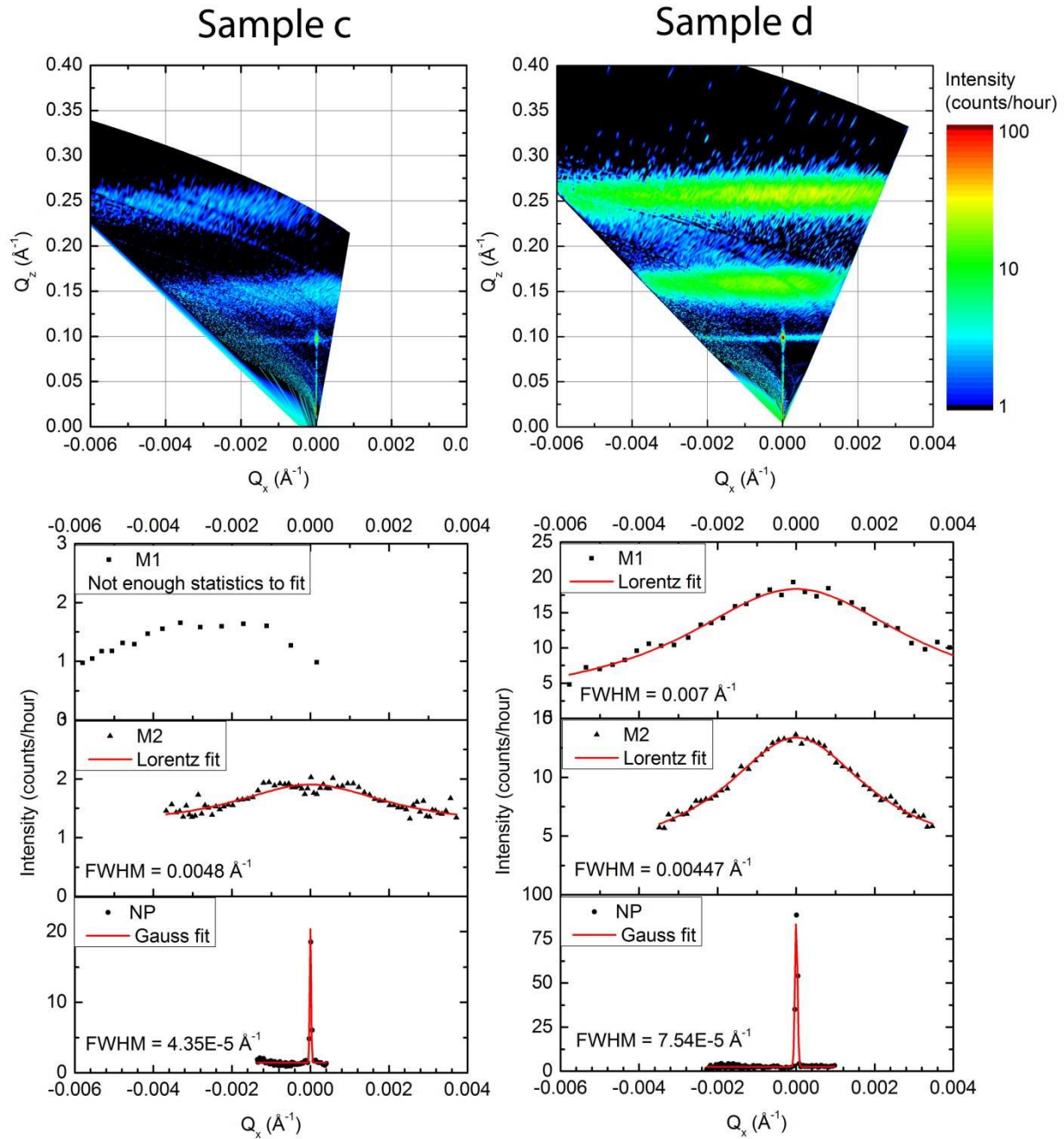


Figure 52. The 3-D reflectivity contour (top) measured by PNR for sample c and d at the helical magnetic state and the off-specular rocking curves (bottom) when Q_z is fixed at the nuclear peak and two magnetic peaks respectively.

The Bragg sheets were also observed at the remanent state of sample d at 5 K and 150 K. The accurate correlation length could not be determined because the intensities are much lower compared to those shown in Fig. 52, but it appears that the correlation length of the helical domains does not change from 5 K to 150 K. The detailed configuration of the helical magnetic domains can be revealed by domain imaging techniques, such as the scanning electron microscopy with polarization analysis (SEMPA) [83]. A complete understanding of the physics of the helical domains requires further study on the temperature and field dependence of the magnetic diffuse scattering.

7. CONCLUSIONS

In this dissertation, we have explored the magnetic phases and phase transitions in both bulk Dy crystal and Dy/Y superlattices by elastic neutron diffraction and polarized neutron reflectivity (PNR) experiments.

In the bulk ^{163}Dy crystal, neutron diffraction experiment was carried out by scanning along the c-axis of the crystal as a function of temperature with different fields (0, 1 T and 1.5 T) applied in the a-axis, covering the well-known ferromagnetic, helical antiferromagnetic, and fan phases as well as several possible new phases suggested by the previous study. It is the first time that the temperature dependence of the field induced magnetic phases been explored by neutron diffraction. The c-axis structural transition shifts to a higher temperature when a non-zero magnetic field is applied in the a-axis. In 1 T field, a second-order ferromagnetism-fan transition, a first-order fan-helix transition, and a second-order helix-paramagnetism transition occur in a sequence upon heating. The fan phase is induced by the magnetic field, thus it is suppressed in zero field as the first-order ferromagnetism-helix transition takes place at the Curie temperature. In 1.5 T field, the helix phase is suppressed, leading to a second-order fan-paramagnetism transition. The possible new phase between ferromagnetism and fan is identified as a mix of ferromagnetic and SRO fan arrangements. No trace of well-defined helifan phase was observed throughout the temperatures. The phase boundaries are determined by the temperature dependence of the magnetic diffraction peaks as well as the diffuse scattering. Taking into account of the newly determined magnetic origin of the field induced phases, the magnetic phase

diagram of Dy has been refined to include the SRO/LRO fan phase, as well as the coexisting helix/fan region. The modulation period of both fan and helix decreases continuously upon heating. Estimated from the period of the magnetic modulation and the average magnetization, a quantitative picture is given on the evolution of the spin arrangement in the fan and helix phases. These behaviors can be understood by considering the competition between the RKKY exchange interaction, the crystal field anisotropy, the magnetostrictive interactions and the Zeeman interaction.

The epitaxial Dy/Y superlattices of various layer thicknesses and repeats were fabricated by DC magnetron sputtering. X-ray characterizations confirmed that the crystallographic and interfacial qualities of the superlattices are comparable to those grown by MBE in previous studies. The macroscopic magnetic properties were characterized by low-temperature magnetometers. The microscopic magnetic structures were investigated by both neutron diffraction and PNR. In summary, at low temperature (5 K), ferromagnetic ordering dominates the sample in high fields (1 to 1.15 T) despite the cooling history, whereas the helical magnetic state appears at low fields (3 to 10 mT). The ordering of helical modulation is sensitive to the interfacial roughness of the sample as well as the cooling history. The helical modulation can be enhanced from a less pronounced helical ordering at low temperature by warming up to 150 K. Once above the Neel temperature (179 K), the paramagnetic state overrules. The turn angle of the helix in Dy characterized by neutron scattering showed reasonably good agreement with previous studies. Off-specular PNR was applied the first time to characterize the helical domain structures in Dy/Y multilayers. The lateral correlation length in the helical magnetic structure was in the order of 100 nm. Meanwhile, a new method of stacking several equivalent samples for neutron diffraction measurements of multilayered samples has been demonstrated.

REFERENCES

- [1] J. Jensen and A. R. Mackintosh, *Rare earth magnetism* (Clarendon Oxford, 1991).
- [2] M. Wilkinson, W. Koehler, E. Wollan, and J. Cable, *J. Appl. Phys.* **32**, S48 (1961).
- [3] D. Gibbs, J. Bohr, J. Axe, D. Moncton, and K. d'Amico, *Phys. Rev. B* **34**, 8182 (1986).
- [4] H. Miwa and K. Yosida, *Progr. Theor. Phys.* **26**, 693 (1961).
- [5] K. Yosida and H. Miwa, *J. Appl. Phys.* **32**, S8 (1961).
- [6] R. M. Nicklow, *J. Appl. Phys.* **42**, 1672 (1971).
- [7] R. J. Elliott, *Phys. Rev.* **124**, 346 (1961).
- [8] W. Evenson and S. Liu, *Phys. Rev.* **178**, 783 (1969).
- [9] W. Koehler, *Acta Crystallogr.* **14**, 535 (1961).
- [10] W. C. Koehler, *J. Appl. Phys.* **36**, 1078 (1965).
- [11] J. W. Cable, E. O. Wollan, W. C. Koehler, and M. K. Wilkinson, *J. Appl. Phys.* **32**, S49 (1961).
- [12] T. Chatterji, *Neutron scattering from magnetic materials* (Gulf Professional Publishing, 2005).
- [13] J. J. Rhyne and A. E. Clark, *J. Appl. Phys.* **38**, 1379 (1967).
- [14] R. Herz and H. Kronmüller, *J. Magn. Magn. Mater.* **9**, 273 (1978).
- [15] N. Wakabayashi, J. Cable, and J. Robertson, *Physica* **241**, 517 (1997).
- [16] M. Akhavan, H. A. Blackstead, and P. L. Donoho, *Phys. Rev. B* **8**, 4258 (1973).
- [17] A. S. Chernyshov, A. O. Tsokol, A. M. Tishin, K. A. Gschneidner, and V. K. Pecharsky, *Phys. Rev. B* **71**, 184410 (2005).
- [18] J. Jensen and A. Mackintosh, *Phys. Rev. Lett.* **64**, 2699 (1990).
- [19] T. Kosugi, S. Kawano, N. Achiwa, A. Onodera, Y. Nakai, and N. Yamamoto, *Physica* **334**, 365 (2003).

- [20] D. Gibbs, D. Moncton, K. d'Amico, J. Bohr, and B. Grier, Phys. Rev. Lett. **55**, 234 (1985).
- [21] R. Cowley and S. Bates, J. Phys.: Condens. Matter **21**, 4113 (1988).
- [22] F. Galeener and J. Blackman, *Disorder in condensed matter physics* (Oxford Science Publications, 1991).
- [23] F. Darnell, Phys. Rev. **130**, 1825 (1963).
- [24] P. Bruno, Phys. Rev. Lett. **67**, 1602 (1991).
- [25] R. W. Erwin, J. J. Rhyne, M. B. Salamon, J. Borchers, S. Sinha, R. Du, J. E. Cunningham, and C. P. Flynn, Phys. Rev. B **35**, 6808 (1987).
- [26] M. B. Salamon, S. Sinha, J. J. Rhyne, J. E. Cunningham, R. W. Erwin, J. Borchers, and C. P. Flynn, Phys. Rev. Lett. **56**, 259 (1986).
- [27] J. Rhyne, R. Erwin, J. Borchers, S. Sinha, M. Salamon, R. Du, and C. Flynn, J. Appl. Phys. **61**, 4043 (1987).
- [28] C. Majkrzak, J. Kwo, M. Hong, Y. Yafet, D. Gibbs, C. Chien, and J. Bohr, Adv. Phys. **40**, 99 (1991).
- [29] S. V. Grigoriev, Y. O. Chetverikov, D. Lott, and A. Schreyer, Phys. Rev. Lett. **100**, 197203 (2008).
- [30] S. V. Grigoriev, D. Lott, Y. O. Chetverikov, A. T. D. Grünwald, R. C. C. Ward, and A. Schreyer, Phys. Rev. B **82**, 195432 (2010).
- [31] J. Haraldsen and R. Fishman, J. Phys.: Condens. Matter **22**, 186002 (2010).
- [32] R. S. Beach, J. A. Borchers, A. Matheny, R. W. Erwin, M. B. Salamon, B. Everitt, K. Pettit, J. J. Rhyne, and C. P. Flynn, Phys. Rev. Lett. **70**, 3502 (1993).
- [33] V. Lauter-Pasyuk, H. J. Lauter, B. P. Toperverg, L. Romashev, and V. Ustinov, Phys. Rev. Lett. **89**, 167203 (2002).
- [34] V. Lauter-Pasyuk, H. Lauter, B. Toperverg, O. Nikonov, E. Kravtsov, M. Milyaev, L. Romashev, and V. Ustinov, Physica **283**, 194 (2000).
- [35] G. Felcher and S. Te Velthuis, Appl. Surf. Sci. **182**, 209 (2001).
- [36] J. Baruchel, S. Palmer, and M. Schlenker, J. Phys. **42**, 1279 (1981).
- [37] J. Lang, D. Lee, D. Haskel, and G. Srager, J. Appl. Phys. **95**, 6537 (2004).
- [38] J. F. O'Hanlon, *A user's guide to vacuum technology* (John Wiley & Sons, 2005).

- [39] M. Ohring, *Materials science of thin films* (Academic press, 2001).
- [40] K. Marton, *Vacuum Physics and Technology* (Academic Press, 1980).
- [41] H. Jiang, T. J. Klemmer, J. A. Barnard, and E. A. Payzant, *J. Vac. Sci. Technol. A* **16**, 3376 (1998).
- [42] H. Jiang, T. J. Klemmer, J. A. Barnard, W. D. Doyle, and E. A. Payzant, *Thin Solid Films* **315**, 13 (1998).
- [43] F. Himpsel, J. Ortega, G. Mankey, and R. Willis, *Adv. Phys.* **47**, 511 (1998).
- [44] T. Schwarz-Selinger, Y. L. Foo, D. G. Cahill, and J. E. Greene, *Phys. Rev. B* **65**, 125317 (2002).
- [45] T. Suzuki, Z. Zhang, A. K. Singh, J. Yin, A. Perumal, and H. Osawa, *IEEE Trans. Magn.* **41**, 555 (2005).
- [46] L. Parratt, *Phys. Rev.* **95**, 359 (1954).
- [47] W. L. Bragg, in *Proceedings of the Cambridge Philosophical Society* (1913), p. 4.
- [48] C. Kittel and P. McEuen, *Introduction to solid state physics* (Wiley New York, 1986).
- [49] E. E. Fullerton, I. K. Schuller, H. Vanderstraeten, and Y. Bruynseraede, *Phys. Rev. B* **45**, 9292 (1992).
- [50] *Physical Property Measurement System, DynaCool User's Manual* (Quantum Design Inc., 2011).
- [51] *Magnetic Property Measurement System Manual* (Quantum Design Inc., 1987).
- [52] A. Barone, *Principles and applications of superconducting quantum interference devices* (World Scientific, 1992).
- [53] G. P. Felcher, *Phys. Rev. B* **24**, 1595 (1981).
- [54] J. Ankner and G. Felcher, *J. Magn. Magn. Mater.* **200**, 741 (1999).
- [55] F. Ott, *C. R. Phys.* **8**, 763 (2007).
- [56] E. Fermi, *Ricerca sci.* **7**, 13 (1936).
- [57] V. F. Sears, *Neutron optics: an introduction to the theory of neutron optical phenomena and their applications* (Oxford University Press, 1989).
- [58] E. Karhu, S. Kahwaji, M. Robertson, H. Fritzsche, B. Kirby, C. Majkrzak, and T. Monchesky, *Phys. Rev. B* **84**, 060404 (2011).

- [59] M. R. Fitzsimmons, P. Yashar, C. Leighton, I. K. Schuller, J. Nogués, C. F. Majkrzak, and J. A. Dura, Phys. Rev. Lett. **84**, 3986 (2000).
- [60] C. Leighton, M. R. Fitzsimmons, A. Hoffmann, J. Dura, C. F. Majkrzak, M. S. Lund, and I. K. Schuller, Phys. Rev. B **65**, 064403 (2002).
- [61] S. Roy, M. R. Fitzsimmons, S. Park, M. Dorn, O. Petracic, I. V. Roshchin, Z.-P. Li, X. Batlle, R. Morales, A. Misra, X. Zhang, K. Chesnel, J. B. Kortright, S. K. Sinha, and I. K. Schuller, Phys. Rev. Lett. **95**, 047201 (2005).
- [62] E. Kentzinger, U. Rücker, and B. Toperverg, Physica **335**, 82 (2003).
- [63] S. Langridge, J. Schmalian, C. H. Marrows, D. T. Dekadjevi, and B. J. Hickey, Phys. Rev. Lett. **85**, 4964 (2000).
- [64] H. Zabel and K. Theis-Bröhl, J. Phys.: Condens. Matter **15**, S505 (2003).
- [65] <http://neutrons.ornl.gov/mr/> (Neutron Science, Oak Ridge National Laboratory, 2014).
- [66] B. Yu, J. A. Harder, J. A. Mead, V. Radeka, N. A. Schaknowski, and G. C. Smith, Nucl. Instr. Meth. Phys. Res. **513**, 362 (2003).
- [67] A. Schreyer, T. Schmitte, R. Siebrecht, P. Bödeker, H. Zabel, S. Lee, R. Erwin, C. Majkrzak, J. Kwo, and M. Hong, J. Appl. Phys. **87**, 5443 (2000).
- [68] A. T. D. Grünwald, A. R. Wildes, W. Schmidt, E. V. Tartakovskaya, J. Kwo, C. Majkrzak, R. C. C. Ward, and A. Schreyer, Phys. Rev. B **82**, 014426 (2010).
- [69] <http://neutrons.ornl.gov/fietax/> (Neutron Science, Oak Ridge National Laboratory, 2014).
- [70] O. Schult, M. Bunker, D. Hafemeister, E. Shera, E. Journey, J. Starner, A. Bäcklin, B. Fogelberg, U. Gruber, and B. Maier, Phys. Rev. **154**, 1146 (1967).
- [71] T. Kaplan, Phys. Rev. **124**, 329 (1961).
- [72] U. Enz, J. Appl. Phys. **32**, S22 (2009).
- [73] T. Nagamiya, J. Appl. Phys. **33**, 1029 (2004).
- [74] Y. Kida, K. Tajima, Y. Shinoda, K. Hayashi, and H. Ohsumi, J. Phys. Soc. Jpn. **68**, 650 (1999).
- [75] J. Mayer, C. Flynn, and M. Rühle, Ultramicroscopy **33**, 51 (1990).
- [76] A. R. Wildes, J. Mayer, and K. Theis-Bröhl, Thin Solid Films **401**, 7 (2001).
- [77] J. Kwo, M. Hong, and S. Nakahara, Appl. Phys. Lett. **49**, 319 (1986).
- [78] A. L. Dantas, R. Camley, and A. Carriço, Phys. Rev. B **75**, 094436 (2007).

- [79] P. A. Kienzle, K. V. O'Donovan, J. F. Ankner, N. F. Berk, and C. F. Majkrzak, (<http://www.ncnr.nist.gov/reflpak>, 2000-2006).
- [80] K. Theis-Bröhl, K. A. Ritley, C. P. Flynn, K. Hamacher, H. Kaiser, and J. J. Rhyne, *J. Appl. Phys.* **79**, 4779 (1996).
- [81] H. Ott, C. Schüßler-Langeheine, E. Schierle, E. Weschke, and G. Kaindl, *Phys. Rev. B* **82**, 214408 (2010).
- [82] S. W. Chen, H. Guo, K. A. Seu, K. Dumesnil, S. Roy, and S. K. Sinha, *Phys. Rev. Lett.* **110**, 217201 (2013).
- [83] J. A. Borchers, J. A. Dura, J. Unguris, D. Tulchinsky, M. H. Kelley, C. F. Majkrzak, S. Y. Hsu, R. Loloe, W. P. Pratt, and J. Bass, *Phys. Rev. Lett.* **82**, 2796 (1999).